

High Speed Optical Links Using CAP Modulation and Novel Equalisation Techniques



Xiaohe Dong

Hughes Hall

University of Cambridge

This thesis is submitted for the degree of Doctor of
Philosophy

November 2019

Declaration

This thesis is the result of my own work and includes nothing which is the outcome of work done in collaboration except as declared in the Preface and specified in the text. It is not substantially the same as any that I have submitted, or, is being concurrently submitted for a degree or diploma or other qualification at the University of Cambridge or any other University or similar institution except as declared in the Preface and specified in the text. I further state that no substantial part of my thesis has already been submitted, or, is being concurrently submitted for any such degree, diploma or other qualification at the University of Cambridge or any other University or similar institution except as declared in the Preface and specified in the text. It does not exceed the prescribed word limit for the relevant Degree Committee

Abstract

High speed optical links suffer from inter-symbol-interference (ISI) due to their limited bandwidth. Equalisation is typically used to mitigate ISI and therefore improve the link capacity. This dissertation explores novel equalisation techniques for carrierless amplitude and phase (CAP) modulation based optical communication systems including OM4 based and plastic optical fibre (POF) based links.

An 850 nm VCSEL based OM4 link using CAP-16 scheme is studied. For the first time, the CAP equaliser, is proposed to mitigate both crosstalk channel interference (CCI) and ISI in the link at the receiver side. Performance comparisons are studied between the CAP-16 scheme using CAP equaliser and a conventional equaliser, pulse amplitude modulation (PAM-4) scheme, and discrete multitone (DMT) scheme. CAP based data transmission of 112 Gb/s is achieved over 150 m OM4 fibre with this novel equaliser, while the conventional equaliser can only support over 1 m OM4 fibre and fails to recover the signals at the same data rate. In addition, this novel equaliser provides a 1.2 dB and 1.7 dB improvement in receiver sensitivity over PAM-4 and DMT schemes, respectively, at 112 Gb/s over 100 m OM4 fibre. A novel pre-CAP-equaliser solving CCI at the transmitter side is also proposed. Data transmission of 56 Gb/s over 100 m OM4 fibre is reported experimentally with an improvement of 0.7 dB in receiver sensitivity compared to using the CAP equaliser at the receiver side. A simulation study shows a 2 dB improvement in receiver sensitivity at 112 Gb/s over 100 m OM4 fibre. Furthermore, an artificial neural network (ANN) equaliser in conjunction with the CAP equaliser structure is explored in a VCSEL based OM4 fibre link in order to further mitigate the nonlinear impairments. For 112 Gb/s data transmission over 100 m OM4 fibre, a 2.4 dB improvement of receiver sensitivity is achieved compared to the CAP equaliser.

In addition to the electrical equalisers, a monolithically integrated silicon optical equaliser consisting of three taps is used for 50 Gb/s data transmission. After 10 km standard single mode fibre (SSMF), error free eye diagrams at the receiver are demonstrated.

A μ LED based POF link based on an APD receiver is also investigated with the CAP equaliser at the receiver side. Data transmission rates of 4 Gb/s over 25 m and 5 Gb/s over 10 m POF links are demonstrated with this equaliser while the conventional equaliser can only support 4 Gb/s over 10 m and fails to recover the signals for 5 Gb/s data transmission.

Acknowledgement

First and foremost, I would like to thank my supervisor Professor Richard Penty for providing me with invaluable guidance and exceptional research environment throughout the period of my PhD study. I would never have been able to finish my dissertation without their consistent help, support and patience.

I also thank my academic adviser Professor Ian White for sharing his wealth of knowledge on optical communication and enlightening me with forward-looking ideas. His devotion to details has benefited me with patience and precision in research.

My special thanks go to Dr. Nikos and Dr. David Cunningham who have been helping me through almost all my experimental work. They have selflessly shared his valuable experiences and insightful ideas on the research. Without their guidance and help, I would not have finished this dissertation.

I must also acknowledge the EPSRC Terabit Bidirectional Multi-user Optical Wireless System and Ultra-parallel visible light communications projects for supporting this work. I would like to thank our colleagues involved in the project for sharing information and ideas.

I thank all members of Centre of Photonic Systems for their kindness, support and hard work to keep this group with an energetic and active environment.

Finally and faithfully, I would like to give my deepest gratitude to my parents for their endless love and unconditional support, without which my doctoral study would not be possible.

To my parents

List of Publications

- [1] **X. Dong**, N. Bamiedakis, D. Cunningham, R. Penty, and I. White, "A Novel Equaliser for 112 Gb/s CAP-Based Data Transmission over 150 m MMF links," *Journal of Lightwave Technology*, 2019.
- [2] **X. Dong**, N. Bamiedakis, D. Cunningham, R. Penty, and I. White, "A Novel CAP Equaliser for 112 Gb/s CAP-Based Data Transmission Over 150 m MMF Links," in *European Conference on Optical Communication (ECOC)*, pp. 1-3, 2019.
- [3] **X. Dong**, N. Bamiedakis, D. Cunningham, R. Penty, and I. White, "112 Gb/s CAP-based Data Transmission over 100 m MMF Links using an Artificial Neural Network Equaliser," in *CLEO: Science and Innovations*, SM1G. 3, 2019.
- [4] **X. Dong**, N. Bamiedakis, D. Cunningham, R. Penty, and I. White, "A Novel Equaliser for 100 Gb/s CAP-Based Data Transmission Over 100 m MMF Links," in *European Conference on Optical Communication (ECOC)*, pp. 1-3, 2018.
- [5] N. Bamiedakis, **X. Dong**, R. Penty, and I. White, "High-Speed Visible-Light Optical Links over Standard Plastic Optical Fibre," in *28th international Conference on Plastic Optical Fibres*, 2019.
- [6] **X. Dong**, N. Bamiedakis, D. Cunningham, R. Penty, and I. White, "LED-based 4 Gb/s Data Transmission over 25 m POF using CAP modulation and A Novel Equaliser", in *Optical Fibre Communication Conference and Exhibition (OFC)*, Submitted, 2019.

Publication in Preparation:

- [1] **X. Dong**, N. Bamiedakis, D. Cunningham, R. Penty, and I. White, "A Novel Feed-Forward Pre-Equaliser for CAP based High-Speed Short-Reach Optical Links," prepared for submission to *Journal of Lightwave Technology*.

Table Contents

CHAPTER 1 INTRODUCTION.....	1
1.1. The development of optical communications	2
1.1.1. Multimode glass fibre links	5
1.1.2. Plastic fibre links	7
1.2. Advanced modulation schemes	9
1.2.1. Non-Return-to-Zero (NRZ)	9
1.2.2. Pulse Amplitude Modulation (PAM)	10
1.2.3. Carrierless Amplitude and Phase (CAP) Modulation.....	11
1.2.3.1. Principle of the CAP modulation format	11
1.2.3.2. CAP prospect for optical communication system	17
1.2.4. Discrete Multitone (DMT) Modulation.....	20
1.3. Mode division multiplexing (MDM) technique.....	21
1.4. Offset launch	21
1.5. Organizations and contributions of the dissertation.....	22
1.5.1. Chapters Organization	22
1.5.2. Contributions of the Dissertation	23
CHAPTER 2 PRINCIPLES OF MULTIMODE FIBRE LINKS	25
2.1. Introduction of multimode waveguides	26
2.1.1. Multimode glass fibre	28
2.2. LED transmitters for POF links.....	40
2.2.1. Resonant Cavity LEDs	42
2.2.2. μ LEDs.....	43
2.3. VCSEL transmitters for MMF fibre links.....	45
2.3.1. Emission spectrum, L-I curve and bandwidth performance	48
2.4. Receivers	49
2.5. Conclusion.....	54
CHAPTER 3 VCSEL BASED OM4 LINK USING CAP MODULATION AND A NOVEL	
EQUALISER.....	56
3.1. Introduction	57
3.2. Simulation model.....	59
3.2.1. VCSEL.....	59
3.2.2. MMF (OM4) fibre	61
3.2.3. PIN receiver.....	62
3.2.4. Noise Model	63
3.2.5. Equalisation	64
3.2.6. Error vector magnitude (EVM).....	67
3.3. Simulation Results	68
3.3.1. CAP-16 based link performance.....	69
3.3.2. Link performance	75
3.4. Conclusion.....	88
CHAPTER 4 LED-POF LINK USING CAP MODULATION SCHEME AND A NOVEL	
EQUALISER.....	89

4.1. Introduction	90
4.2. Simulation model.....	91
4.2.1. LED	91
4.2.2. SI-POF	92
4.2.3. Simulation model of APD receiver	93
4.2.4. Overall frequency response and phase response	94
4.3. Simulation results	96
4.4. Experimental results	101
4.5. Conclusion.....	105
CHAPTER 5 A FEED-FORWARD PRE-EQUALISER FOR CAP BASED HIGH SPEED	
SHORT REACH OPTICAL LINKS.....	107
5.1. Introduction	108
5.2. Feed-forward pre-equaliser structure.....	109
5.3. Simulation Results	113
5.4. Experimental Results	118
5.5. Conclusion.....	120
CHAPTER 6 ARTIFICIAL NEURAL NETWORK BASED EQUALISERS.....	122
6.1. Artificial Neural Network.....	123
6.1.1. Introduction	123
6.1.2. Structure of CAP ANN equaliser	123
6.1.3. Noise.....	125
6.1.4. Simulation results	126
6.1.5. Experimental results	127
6.1.6. Conclusion.....	129
CHAPTER 7 OPTICAL EQUALISERS	130
7.1. Silicon optical equaliser.....	131
7.1.1. Introduction	131
7.1.2. Design and experimental setup	132
7.1.3 Experimental Results	134
7.1.4. Conclusion.....	136
CHAPTER 8 FUTURE WORK	138
8.1. Future work	139
8.1.1. Parallel transmission.....	139
8.1.2. Artificial neural network based pre-equalisation scheme	140
8.1.3. CAP modulation based other optical communication links	141
CHAPTER 9 CONCLUSIONS	142
9.1. Conclusion.....	143
Appendix	146
BER estimation method.....	146
References	135

List of Figures

Figure 1.1: Global IP traffic forecast (2017-2022) of various devices predicted by Cisco [9]	4
Figure 1.2: Proposals of Fast Ethernet over plastic optical fibres	7
Figure 1.3: NRZ modulation scheme.....	10
Figure 1.4: PAM-4 modulation scheme.....	11
Figure 1.5: Nyquist pulse shapes	12
Figure 1.6: ISI free of Nyquist pulse functions	12
Figure 1.7: Waveform (a) and spectrum (b) of a series of raised cosine pulse shaping filters with different roll off factors	13
Figure 1.8: CAP signal generation.....	13
Figure 1.9: Impulse response of I/Q- channel filter.....	14
Figure 1.10: Magnitude and phase spectrum difference ($\angle I(\omega) - \angle Q(\omega)$) between I- and Q- filter	15
Figure 1.11: CAP signal demodulation.....	15
Figure 1.12: Convolution results of the I- filter or Q- filter at the transmitter side with the I- matched filter at the receiver side	16
Figure 1.13: Block diagram of DMT modulation and demodulation (S/P: serial to parallel conversion, P/S: parallel to serial conversion, CP: cyclic prefix).....	21
Figure 2.1: Refractive index profiles of (a) step-index and (b) graded-index multimode glass fibres	27
Figure 2.2: Schematic of light propagation in a grade-index multimode glass fibre	29
Figure 2.3: Attenuation of different standard-NA SI-POF (measurement by POF-AC) [23]	34
Figure 2.4: illustration of total internal reflection and light confinement within the fibre	35
Figure 2.5: structure and refractive index profile of SI-POF	36
Figure 2.6: Efficiency of various LED material systems [23]	41
Figure 2.7: Switching times of various LED material systems [23]	41
Figure 2.8: Spectrum of a blue LED (SHR470) [23]	42
Figure 2.9: Structure of a RC-LED.....	43
Figure 2.10: Schematic of (a) microscope image of a violet μ LED array (b) the cross-sectional of the μ LED array design and (c) the circular segmented μ LED arrays [111].....	44
Figure 2.11: Maximum modulation bandwidths of μ LEDs of different diameters of the violet, blue and green μ LEDs [111].....	44
Figure 2.12: schematic of a VCSEL structure	46
Figure 2.13: Emission spectrum of a 5 mm x 5 mm VCSEL array at 100 W output power (120A) [114]	46
Figure 2.14: (a) Emitted spectrum at 12 mA bias and (b) optical power coupled in the 50 μ m MMF	48
Figure 2.15: Measured small signal modulation response at increasing bias currents for the 850 nm VCSEL [115]	48
Figure 2.16: Schematic of the basic PIN detector structure with electric field distribution under reverse bias [79]	49
Figure 2.17: An APD together with the electric field distribution inside various layers under reverse bias [79].....	52

Figure 2.18: Measured receiver bandwidths for PIN detectors of various sizes and reverse bias voltage levels [23]	53
Figure 3.1: (a) Measured and modelled frequency response at 5 mA and 7.5 mA under different temperature conditions [130] (b) measured eye diagram of Broadcom's 25G PAM4 VCSEL and (c) modelled eye diagram overlapped with the measured eye diagram [130]	61
Figure 3.2: Frequency Response of the Gaussian OM4 fibre model.	62
Figure 3.3: Frequency response of the PIN receiver model with 30 GHz bandwidth	63
Figure 3.4: Experimental setup for receiver noise measurement.....	63
Figure 3.5: Measured RMS value of the total noise at various received optical power (ROP: receive optical power).....	64
Figure 3.6: Pre-cursor ISI and post-cursor ISI of a symbol after dispersive channel	65
Figure 3.7: Pre-cursor ISI and post-cursor ISI of a symbol after dispersive channel	66
Figure 3.8: Schematic of a Decision feedback equaliser	66
Figure 3.9: detailed structure of the conventional FFE and DFE	67
Figure 3.10: Typical CAP-based transmission.....	69
Figure 3.11: Block diagram of link model used for CAP	70
Figure 3.12: Ideal (a) I- channel eye diagram and (b) constellation diagram	71
Figure 3.13: Demodulation results over 100 m OM4 fibre at various symbol rate: (a) 5 Gbaud(20 Gb/s), (b) 15 Gbaud (45 Gb/s) and (c) 25 Gbaud (100 Gb/s)	71
Figure 3.14: Structure of (a) a conventional FFE and DFE equaliser and (b) the proposed CAP equaliser for I- channel recovery. Similar structure can be applied for Q- channel.....	74
Figure 4.1: Schematic of simulation model	91
Figure 4.2: Frequency response of the LED model with 150 MHz bandwidth	92
Figure 4.3: Frequency response of the Gaussian POF model for various length.....	93
Figure 4.4: Frequency response of raised cosine model of the APD receiver with 650 MHz bandwidth	94
Figure 4.5: Simulated frequency response (a) frequency response and (b) phase response	94
Figure 4.6: Experimental setup for receiver noise measurement.....	95
Figure 4.7: Measured APD current versus (a) noise RMS voltage and (b) received optical power.....	95
Figure 4.8: ideal and received waveforms over 25 m POF at 4Gb/s.	97
Figure 4.9: Constellation diagram (before equalisation) over 25 m POF length at various data rate: (a) 400 Mb/s (100 MBaud), (b) 800 Mb/s (200 MBaud), (c) 2 Gb/s (500 MBaud) and (d) 4 Gb/s (1 GBaud)	97
Figure 4.10: Demodulated I- channel symbols for the two modes of operation before equalisation at two different symbol rates (a) 100 MBaud (400 Mb/s) and (b) 1 Gbaud (4 Gb/s)	98
Figure 6.1: Structure of ANN	124
Figure 6.2: Schematic of the method for calculating the noise after the ANN equaliser (EQ: equaliser)	125
Figure 6.3: Link model used.....	126
Figure 6.4: Recovered constellation diagrams at 112 Gb/s over a 100 m OM4 fibre: (a) conventional equaliser, (b) CAP equaliser and (c) ANN equaliser	127
Figure 6.5: BER performance of CAP-16 based on ANN and CAP equalisers and DMT at 112 Gb/s over a 100 m OM4 fibre	127
Figure 6.6: Experimental Setup (AWG: arbitrary waveform generator, OSC: oscilloscope, Demod:	

demodulation, EQ: equaliser)	128
Figure 6.7: Constellation diagrams at 112 Gb/s over 100 m OM4 fibre: (a) conventional equaliser, (b) CAP equaliser and (c) ANN equaliser.....	128
Figure 6.8: BER performance of two equalisers based on CAP-16 scheme and DMT scheme at 112 Gb/s over a 100 m OM4 fibre.....	129
Figure 7.1: Principle of the optical equaliser	132
Figure 7.2: Image of this on-chip optical equaliser.....	133
Figure 7.3: Experimental setup to characterize the optical equaliser.....	134
Figure 7.4: VOAs (three taps) against their applied voltages	135
Figure 7.5: Delays of impulse responses (three taps)	135
Figure 7.6: Eye diagrams at B2B and after 10 km without and with the optical equaliser.	136
Figure 8.1: 400 Gb/s optical transmission: (a) OM4 bundle and (b) 2×2 VCSELs array	139
Figure 8.2: 400 Gb/s over a single OM4 fibre achieved by SWDM technique	139
Figure 8.3:(a) Hexagonal SI-POF bundle for parallel transmission, (b) WDM-POF link.....	140
Figure 8. 4: Schematic of the link with pre-distortion based on ANN algorithm.	141

List of Tables

Table 2-1 Comparisons of SI-POF, GI-POF, MMF, SSMF, and RG-6[104]	38
Table 3-1: parameters used in the basic rate equations.....	59
Table 3-2: Rate equation parameters for various types of VCSELs	60
Table 3-3: Link simulation parameters	69
Table 4-1: Summary of simulation parameters.....	96
Table 5-1: equaliser parameters.....	115

CHAPTER

1

INTRODUCTION

This chapter gives an overview of the historical development of optical communications and worldwide data traffic demands nowadays over the optical networks today. The multimode glass fibre link and POF link have been introduced. Advanced modulation formats with high spectral efficiency have also been illustrated.

1.1. The development of optical communications

The use of light for communication can be dated back to thousands of years ago when people used signal fibres and smoke to convey information or draw attention. This further evolved to more complicated signaling systems using flags and lamps throughout more modern history. In 1880, Alexander Graham Bell demonstrated his photophone which was believed to be the first time human speech successfully transmitted through an optical signal [1]. This was demonstrated between two buildings 213 m apart. The transmission medium was the atmosphere. However, in the 19th century, the electrical wire was a much more robust transmission medium and the telephone was more practical at that time. The idea was only further developed for military use [2]. The main limitation in Bell's idea was the beam divergence. The solution involved is to achieve the optical transmission by confining the light beam to a certain medium like the electrical signal carried by copper wires. Therefore, the signal power can be largely maintained, and the optical path is more flexible. In 1841, this concept was first demonstrated by Swiss physicist Daniel Colladon [3]. He focused sunlight on a water tank to illuminate the water so that the back of the lecture hall could have a better view. However, Colladon did not see the importance of this work which was not further explored. A few years later, an Irish-born physicist, John Tyndall, popularized the light guiding effect known as total internal reflection where the light can be completely reflected at a material boundary. In 1957, the Indian scientist Narinder Singh invented the fibre scope which initiated the development of all glass optical fibres. At nearly the same time, the invention of the semiconductor LED and laser in the 1960s made a significant step forward for guided optical transmissions. However, early on, glass fibres had attenuation rates of ~ 1000 dB/km, which is too high for practical use. In 1964, Charles Kao and George Hockham proposed that the attenuation of the fibre loss can be reduced to 20 dB/km if the iron-impurity can be reduced, which made fibres a practical communication medium [4]. In 1970, the first optical fibre with loss less than 20 dB/km at 633 nm was developed by Corning. The fibre attenuation dropped dramatically with the advanced glass purification technologies and the exploration of lasers with longer wavelengths. In 1970, the invention of a semiconductor laser emitting continuous waves at room temperature by separate teams at the Lofe Physical Institute and Bell Labs [5] started a new phase of transmitting light through fibre optic cables over long distances. In 1977, the general electronics and telephone deployed the first live telephone traffic by fibre optics at 6 Mbps, in Long Beach, California [6]. Since then, optical fibre communication has

become more and more important in modern communication systems. Long distance communication becomes possible owing to the high capacity enabled by the optical carrier and the low attenuation achieved by the advanced optical fibre.

For short-reach multimode optical links, Corning produced a multi-mode fibre with a loss of only 4 dB/km in the spectral window around 850 nm by replacing titanium with germanium as a dopant inside the fibre's silica core in 1970 [7]. The region of lowest loss was matching the operating wavelength of GaAs semiconductor lasers leading to the first generation of optical fibre communication systems, which operated around 850 nm over multimode fibre (MMF) [7]. After that, many industrial laboratories race to further reduce the fibre losses during the 1970's. In 1979, a Japanese group reported losses near 0.2 dB/km around 1.55 μm [7]. In the 1980's, MMF links was used in Enterprise networks, supporting applications such as private telephone switches (PBX's), data multiplexers, and LANs. In the 1990's, it become the main media for backbone deployments which require reach beyond the capability of copper twisted pair cabling. This motivated a conversion of MMF core diameter from 62.5 μm (OM1) to 50 μm (OM2) and then the first laser-optimized multimode fibre offers a bandwidth distance product at least 2000 MHz·km at 850 nm in the late 1990's. In the 2000's, OM4 arrives, offering at least 4700 MHz·km. Nowadays, OM3 and OM4 are the primary fibre media for Ethernet and fibre channel applications and OM5 has been a recognized media in emerging Ethernet. The majority of short-reach optical links consists of multimode fibre (MMF) links based on 850 nm vertical cavity surface-emitting lasers (VCSELs). 40 Gb/s open eye diagrams have been demonstrated over a 62.5 mm-core multimode fibre (0.8 m) for VCSELs based short-reach optical communications using a nonreturn-to-zero (NRZ) data pattern. The results demonstrated that directly current-modulated VCSELs can be applied in the near future for reliable ultra-high speed data transmission in short distance optical data networks and interconnects [8].

The new technology motivated the development of more convenient communication approaches. Exchanging and sharing information efficiently is crucial to improving the quality of people's daily lives. Internet and computing technology improve the efficiency of communication, whilst requiring a massive amount of bandwidth resources. More and more information is sent digitally owing to well-established optical communication systems. Video streaming, cloud computing and file sharing require an increasing capacity of the communication industry. Cisco predicted that the overall IP traffic is expected to grow to 396 EB per month by 2022. This is mainly driven by an increase in the growing share of mobile traffic

as percentage of the total IP traffic. The video effect of mobiles or PCs on the traffic becomes more pronounced due to the introduction of Ultra-High-Definition (UHD) and video streaming (Figure 1.1). By 2022, it can be estimated that nearly two thirds of the installed flat-panel TV sets will become UHD, from only one-fifth in 2017.

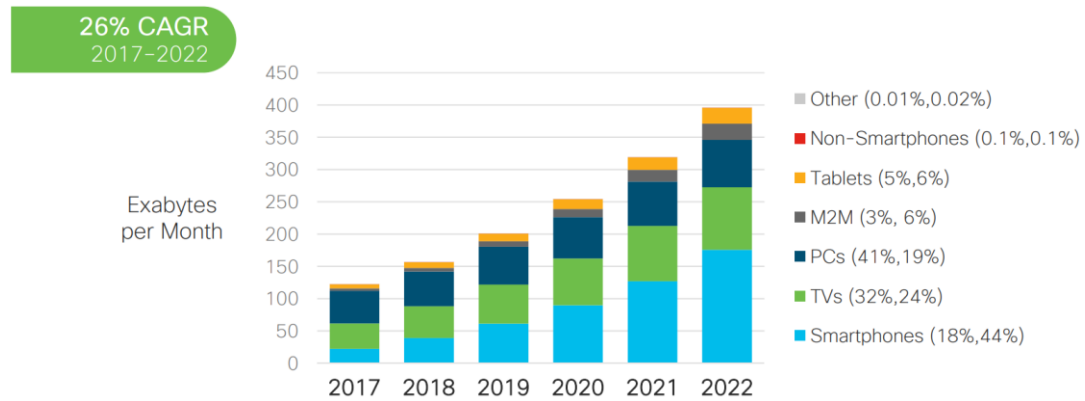


Figure 1.1: Global IP traffic forecast (2017-2022) of various devices predicted by Cisco [9]

In order to achieve these new services, line rates of a few Mbit/s are insufficient, and can only support web and email browsing and some basic VoIP applications. With the increasing demand for data transmission such as multi-core servers, virtualization, network storage, and data center aggregation, 40 GBE and 100 GBE was defined by the IEEE 802.3 in 2010 and developed by the 802.3bj-2014, 802.3bm-2015, and 802.3cd-2018 standards. For short distance, optical fibres are the perfect solution owing to the high capacities in comparison with other medias, such as copper cables. Although SSMF has higher bandwidth distant product than multimode fibres, it is not cost-effective to implement SSMF due to its high cost of the connectivity which is not suitable for the access-point-intensive environment [10, 11]. The multimode fibre has been applied in these environment for decades. Although the multimode fibre's bandwidth does not meet the requirement of today's bandwidth, replacing the high-cost SSMF will not cause significant cost concerns and market difficulties, which makes the multimode fibre a very popular solution for short-distance communication.

The progress for the optical fibre communication can be categorized into several generations including low-loss single fibre[12], the EDFA[13], wavelength division multiplexing[14, 15], advanced high-spectral efficiency coding via digital signal processing enabled coherent transmission and also the recent

space division multiplexing technique. The transmission capacity increases around tenfold every four years. Ultra-high speed data transmission can now be achieved by fibre-optic communication. Furthermore, the development of fibre-optic communication is thought to be able to continually support the future demand for higher data capacity.

1.1.1. Multimode glass fibre links

The Multimode glass fibre has been mainly used for short-distance applications, especially for in-building networks. The multimode glass fibre was introduced to the fibre distributed data interface (FDDI) as an alternative solution for the conventional copper -based high speed local area network [16]. LEDs and 62.5 μm multimode glass fibres (OM1) were employed in this technology with a data rate of up to 100 Mbit/s. FDDI had been very popular for years before the proposal of a more effective solution called Fast Ethernet in late 1995 [17]. The early generation of multimode glass fibres (OM1 and OM2) have the bandwidth-distance products of up to $\sim 500 \text{ MHz}\cdot\text{km}$. This low bandwidth is due to the large number of supported modes in the multimode glass fibre which has different propagation velocities. Therefore, multimode fibre links are only used over short distances with a link length typically less than 500 m. However, the large core size of the multimode fibre allows for low-cost LEDs to be used as the transmitter. The divergence of the large beam from the LED and limited bandwidth of the LED reduce the overall capacity of the multimode glass fibre link in a high-capacity system. The invention of the semiconductor laser, however, solved this problem owing to the much higher bandwidth of lasers than that of traditional LEDs [18]. Moreover, the narrower optical spectrum reduced the chromatic dispersion for different wavelengths[19, 20], and the smaller emitted spot size on the multimode fibre excited fewer modes [21].

With the increasing demand for data rates and component bandwidth, new multimode glass fibres have also been developed. The first generation of OM1 multimode glass fibres have been implemented for more than 20 years and new types of multimode glass fibres (OM2, OM3 and OM4) are also developed later.

OM1 fibre have a core size of 62.5 μm and typically comes with an orange jacket. It can support 10 Gigabit Ethernet at lengths of up to 33 meters. It commonly used a LED source and is mostly applied for 100 Megabit Ethernet applications. OM2 fibre is also with orange jacket and uses a LED source as OM1

does. However, it has a smaller size of 50 μm and supports up to 10 Gigabit Ethernet at lengths up to 82 m. It is more commonly used for 1 Gigabit Ethernet applications. OM3 fibre is with an aqua color jacket and has the same core size as OM2 fibre has. It is optimized for laser-based equipment and able to support 10 Gigabit Ethernet up to 300 m. OM3 fibre can support 40 Gigabit and 100 Gigabit Ethernet up to 100 m but is commonly used for 10 Gigabit Ethernet. OM4 fibre is backwards compatible with OM3 fibre and has the same distinctive aqua jacket. OM4 was specifically developed for VCSEL based transmission and enables 10 Gig/s link distances of up to 550 m compared to 300 m with OM3 and is able to support 40/100Gigabit Ethernet up to 150 m. The VCSEL sources have narrower spectral widths than LEDs, therefore the chromatic dispersion was greatly minimized compared to OM1 and OM2 fibres. The modal dispersion then becomes the main factor resulting to the inter-symbol-interference.

OM1 fibres are popular owing to their bandwidth being sufficient for most in-building applications in the Gigabit Ethernet age, as well as their low cost. However, OM1 fibres tend to struggle for 10 Gbit/s links due to their inadequate bandwidth for the required length of in-building networks. According to the IEEE 10GBASE-LRM standard, electrical dispersion compensation (EDC) technology have to be employed. However, for higher speed links such as 40 Gbits/s or even 100 Gbits/s, the low bandwidth of the OM1 fibre cannot reach the required link length for the in-building networks. Since the 40 G/100 G Ethernet standard has been published, the most challenging issue is the cost-effective solution for updating the existing fibre bases. OM1 and OM2 fibres were not considered in this standard due to their limited bandwidth.

In response to this emerging need, the OM4 fibre has been developed to enhance the system cost benefits enabled by 850 nm VCSELs. OM4 fibre can support services such as Ethernet and Fibre Channel, enabling an extended reach of up to 550 m for ultra-long building backbones and medium length campus backbones [21]. OM4 fibre is also well suited for shorter reach data centres and high-performance computing applications. The high bandwidth of OM4 fibre provide more tolerance to the extra channel insertion loss when it is employed at a shorter distance than its rated distance. A number of standards were developed which defined the use of OM4 fibre for high-speed transmission. For example, within the TIA, OM4 fibre performance specifications have been defined in TIA-492AAAD. Besides these, OM4 fibre can also support video, data and voice services in data centres and premises cabling in data networks including backbone, riser and horizontal. OM4 fibre can provide a minimum reach of 125 m

over multi-mode fibre under the 40 GBE and 100 GBE standards. Therefore, in this thesis, OM4 is chosen for investigation of multimode glass fibres for the single lane 100 Gbits/s laser system.

1.1.2. Plastic fibre links

In an optical communication system, the optical transmitter is used to transfer the electrical signal into its optical form. For the POF based system, the common optical sources used are light-emitting diodes with their thermal stability, low-cost and intrinsic eye safety. A group of researchers in Germany proposed a standard by using Fast Ethernet over POF [22]. Three different versions are described in the proposal, as shown in Figure 1.2. The 50 m link is achieved using both 650 nm and 510 nm LEDs (with connectors) whilst the 100 m link is only achieved using a 510 nm LED. For the 50 m links, the standard step index POF is used which is able to provide sufficient bandwidth. However, this type of fibre does not support the 100 m link due to its low bandwidth and the double step index POF has to be used. Although semiconductor lasers have also been employed for high speed demonstrations [23], large bandwidth μ LEDs with diameters $\leq 100 \mu\text{m}$ have recently attracted much research interest [24, 25].

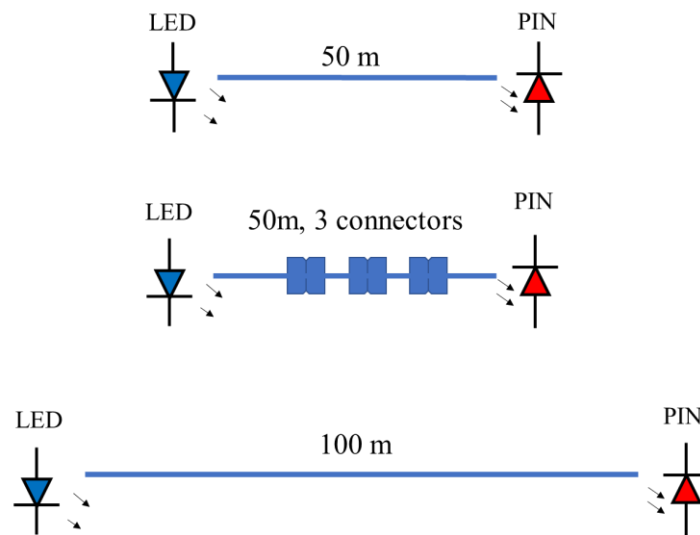


Figure 1.2: Proposals of Fast Ethernet over plastic optical fibres

The function of the optical receiver is to convert the optical signal back into its electrical form which carries the original information. PIN photodiodes are widely used in the POF links while the APD has

been demonstrated to have improved sensitivity compared to the conventional PIN in multi-gigabit applications [26]. NRZ (non-return-to-zero) is conventionally used in optical communication systems and has also been investigated for LED based POF links as it is easy to be implemented and straightforward clock recovery circuits can be used. However, owing to the low bandwidth of the POF links, it is unrealistic to achieve multi-gigabit applications such as 3DTV, HDTV and multi-sensor automotive data networks employing the NRZ modulation scheme. Advanced modulation schemes such as multilevel and multi-carrier schemes are required to achieve high spectral efficiency and enable high speed POF links. Besides these, the equalisation technique is also used to solve the inter-symbol-interference (ISI) introduced by the low bandwidth of the link and recover the distorted signals at the receiver.

The first POF link was presented in the literature in 1988 with a 20 Mb/s over 80 m PMMA-based step index POF [27]. In 1992, Hewlett Packard invented the first commercial POF transceiver [28] at 50 Mb/s over proposed POF of 15 m [29]. By this, Hewlett Packard became one of the most important pioneers in the field of POF communications.

The standard PMMA-based POF normally has a core size of 500 μm to 1000 μm [30]. This makes the fibre strongly multimode, which introduces large modal dispersion [31] and also very small bandwidth-distance product of less than 2 MHz·km. In addition, POF also exhibits high fibre loss of ~ 0.2 dB/m at 650 nm wavelength. However, POF has presented some important advantages over their glass counterpart. The large core size of POF allows low precision plastic connectors to be used, which provides low cost connectivity and installation and reduces the total costs of the system. For example, POF is much easier to handle and more tolerant against challenging environments. The attenuation remains constant when POF is dipped into such liquids including water, NaOH, sulfuric acid (34.6%) or engine oil at 50 °C for 1000h [32]. These factors make POF a very popular transmission medium for short-range optical communications such as in-car networks and home networks where the multimode glass fibre is too fragile or the copper cable cannot withstand the challenging environments.

Currently, as more and more devices become interconnected, the traffic demand for home networks is rapidly increasing such as high-definition television, 3DTV, uncompressed video calls, online gaming and cloud computing. High speed access is available now owing to the development of high speed passive

networks [33] but the challenge is the home network solution ability to connect all devices. POF has been considered as an inexpensive home networking solution which has attracted great attention. POF has been proposed as the backbone of the home network as WIFI access points distributed throughout the home. POF backbone can exploit the available electrical and optical bandwidth and support a high quality of service to multiple users [34].

Besides in-home applications, POF can also be used for automotive networks. It was first introduced into automotive networking in 1998 and the Media Oriented Systems (MOST) promoted since then. The MOST provides a robust and reliable network protocol for interconnecting entertainment multimedia and POF is specified as the physical data transmission medium by the MOST standard. Nowadays, MOST technology has been used in almost every car brand worldwide. The development of automotive industry aims to make cars more intelligent with more sensors and applications and its market is estimated to be USD 6.78 billion in 2018 and predicted to reach USD 19.99 billion by 2025 [35]. The HD audio/video, 3D video, next generation wireless networking and drive assist applications are raising new challenges for future automotive systems. The latest MOST 150 networks can support mobile connectivity and entertainment up to 150 Mb/s [36]. It is believed that the next generation in-car network will require a data rate of $\sim 3\text{Gbit/s}$.

1.2. Advanced modulation schemes

For short range optical communications, research has been concentrated on improving the capacity of the link. However, the data rate is limited by the low bandwidth of the link. The optical communication has been evolved from the NRZ scheme to advanced modulation schemes with high spectral efficiency. These modulation schemes have been proposed and implemented to achieve high speed optical links such as Pulse Amplitude Modulation (PAM), Carrierless Amplitude and Phase modulation (CAP), and Discrete Multitone (DMT).

1.2.1. Non-Return-to-Zero (NRZ)

As a simple modulation scheme, NRZ has only two levels: 0 and 1 (Figure 1.3). The spectral efficiency is 1 bps/Hz without any pulse shaping filter. It has been both employed in POF based and OM4 based

links. Data rates up to 1 Gb/s have been demonstrated in a POF based link using a single μ LED with a PIN receiver based on the NRZ scheme[25]. A 71Gb/s data transmission has also been achieved using the NRZ scheme on an 850 nm VSCSEL based optical link [37]. However, due to the low bandwidth of the link and low spectral efficiency of the NRZ modulation, higher data rates are difficult to be implemented and therefore advanced modulation formats are required.

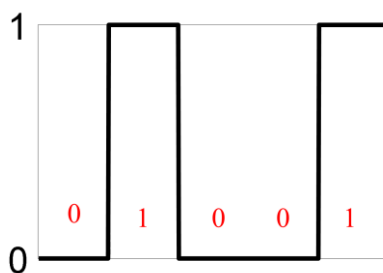


Figure 1.3: NRZ modulation scheme

1.2.2. Pulse Amplitude Modulation (PAM)

PAM employs pulse amplitude to encode the data, which can use 2^N levels to represent N bits of data in one symbol. For example, PAM-4 signal has 4 symbols that vary from 0 to 3, and each encoded symbol has 2 bits (Figure 1.4). Therefore, when the system has symbol rate R Gbaud/s, the resultant aggregate data rate is up to $2R$ Gb/s.

Spectral efficiency is an important parameter which measures how efficiently the spectrum is used. With regards to the PAM-4 and PAM-8 schemes, their spectral efficiencies are twice and three times of that for the NRZ modulation scheme, respectively. Therefore, much lower bandwidth is required compared to that required by the NRZ modulation scheme at the same data rates. Generally, without pulse shaping, PAM- 2^N can achieve a spectral efficiency of N bps/Hz while NRZ can only achieve 1 bps/Hz.

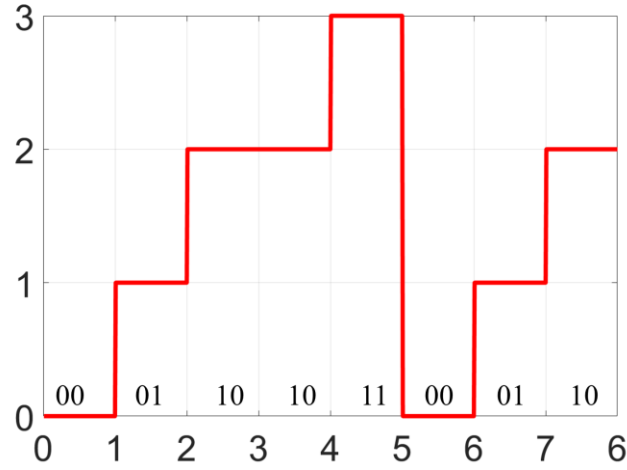


Figure 1.4: PAM-4 modulation scheme

Several PAM-modulation based data transmissions on short range optical links have been reported. In [26], PAM-32 was employed to achieve 5 Gb/s data over 25 m POF. For the VCSEL based link, PAM-4 was demonstrated at a 150 Gb/s data rate over a 100 m OM4 fibre.

1.2.3. Carrierless Amplitude and Phase (CAP) Modulation

1.2.3.1. Principle of the CAP modulation format

CAP uses two passband orthogonal filters to encode the baseband Nyquist pulses. The principle of the Nyquist pulse is first investigated in this section. In digital communication systems, the received pulse should not interfere with adjacent pulses. Nyquist criterion, to achieve zero inter-symbol-interference (ISI), guarantees that samples only have one non-zero value at each sampling point. It is based on a specific shape (Figure 1.5) with zero ISI between each other. In the time domain, the Nyquist pulse with minimum bandwidth is expressed as

$$q(t) = \text{sinc}\left(\frac{t}{T}\right) \quad 1-1$$

where sinc function is defined as: $\text{sinc}(x) = \sin(\pi x) / (\pi x)$. It can be clearly seen that the pulse crosses zero at $t=nT$.

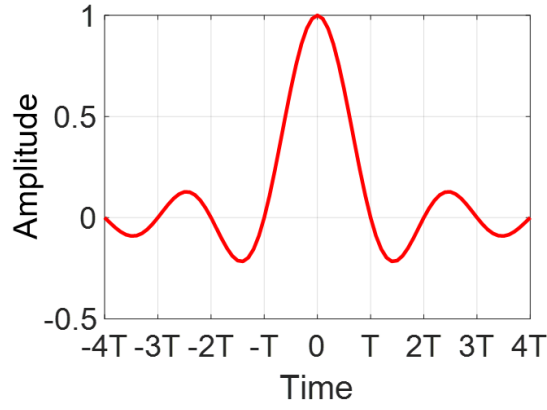


Figure 1.5: Nyquist pulse shapes

Therefore, the sample only contains the information from one symbol if sampling at $t=nT$. Figure 1.6 shows that no interference is generated from adjacent symbols.

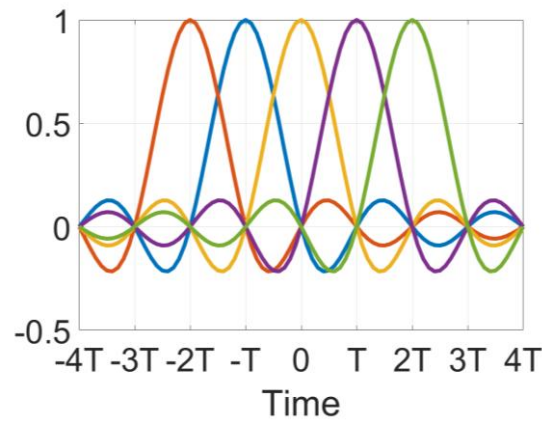


Figure 1.6: ISI free of Nyquist pulse functions

However, a sinc pulse is not available as it requires an ideal rectangular spectrum in the frequency domain, which is difficult to be generated with any form of electronics. With a reasonable roll off factor value, the raised-cosine pulse can be practically generated using a finite impulse response filter by truncating the pulse to a certain length of integer multiples of T . Therefore, a practical Nyquist pulse usually has a wider bandwidth than $1/2T$ with a roll-off factor in the spectrum. This can be written as

$$p(t) = \frac{\sin(\pi t/T)}{\pi t/T} \left[\frac{\cos(\alpha \pi t/T)}{1 - (2\alpha t/T)^2} \right] \quad 1-2$$

where α is the roll-off factor. Raised-cosine pulses with different roll-off factors and their spectrums are

plotted in Figure 1.7.

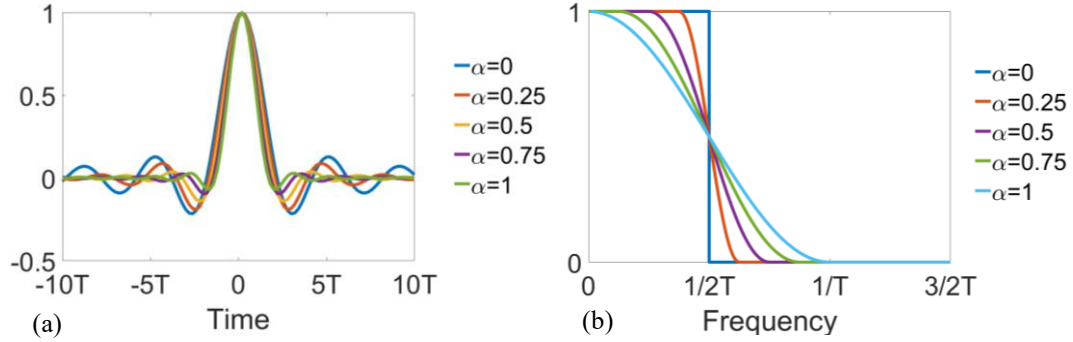


Figure 1.7: Waveform (a) and spectrum (b) of a series of raised cosine pulse shaping filters with different roll off factors

The roll-off factor is also known as the excess bandwidth which indicates how much bandwidth is above $1/2T$. If the roll-off factor is 1, the excess bandwidth is 100% and the bandwidth of the signal becomes $1/T$.

For CAP modulation, the amplitude of the pulses for either channel can be also made to be multilevel as well. Figure 1.8 illustrates the schematic block diagram for the CAP signal generation.

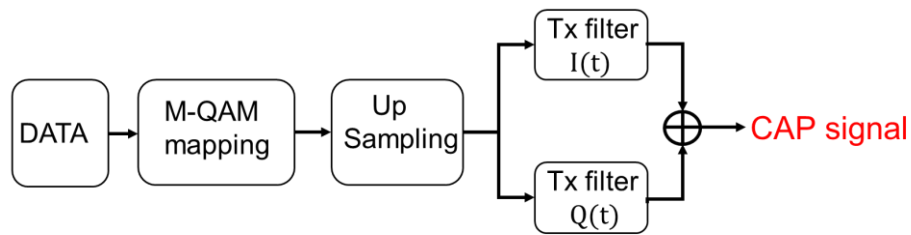


Figure 1.8: CAP signal generation

The input data is divided into two parallel data streams (QAM-mapping) firstly, encoded into symbols, and then up-sampled. After that, it is encoded by the I- and Q- transmitter filters and combined together as the transmitted signal. The transmitted CAP signal is expressed in 1-3

$$s_T(t) = D_I(t) \otimes I(t) + D_Q(t) \otimes Q(t) \quad 1-3$$

Where $D_I(t)$ and $D_Q(t)$ is the encoded up-sampling I- and Q- channel symbols, $I(t)$ and $Q(t)$ are the I- and Q- filters at the transmitter side. The I- and Q- channel filters can be expressed as

$$I(t) = \cos\left(\frac{\pi(1+\alpha)t}{T}\right)g(t) \quad 1-4$$

$$Q(t) = \sin\left(\frac{\pi(1+\alpha)t}{T}\right)g(t) \quad 1-5$$

where T is the symbol duration and α is the roll-off factor, and $g(t)$ is known as square root Nyquist raised-cosine filters.

$$g(t) = \frac{\sin(\pi(1-\alpha)t') + 4\alpha t' \cos(\pi(1+\alpha)t')}{\pi t' [1 - 4\alpha^2 t'^2]} \quad t' = t/T \quad 1-6$$

As the transmitter and receiver sides are both encoded by square root pulses, the resultant overall response of the shaping filter has a Nyquist raised-cosine response. Figure 1.9 shows the shapes of I- and Q- channel pulses.

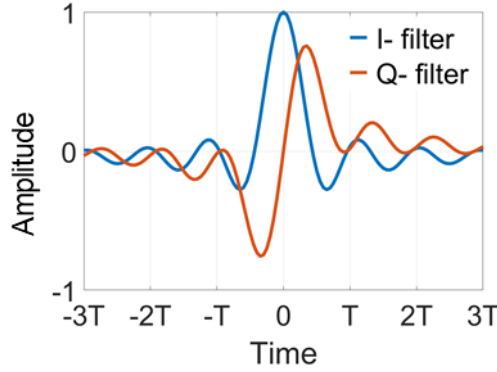


Figure 1.9: Impulse response of I/Q- channel filter

The I- and Q- pulses filters have the same magnitude in the frequency domain however with different phase spectrums. Figure 1.10 shows the spectrum magnitude and phase difference of the I- and Q- transmitted filter which gives a $\pi/2$ constant phase difference over the spectrum, indicating the orthogonality between I- and Q- channel (α is the roll off factor and T is the symbol duration).

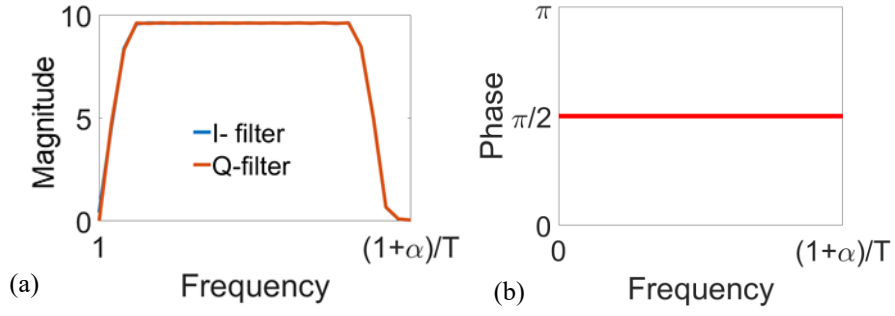


Figure 1.10: Magnitude and phase spectrum difference ($\angle I(\omega) - \angle Q(\omega)$) between I- and Q- filter

At the receiver side, the incoming signal includes information from both I- and Q- channel. Two matched filters are used to separate signals, shown in **1-7** and **1-8**.

$$r_I(t) = s_R(t) \otimes I_M(t) \quad \mathbf{1-7}$$

$$r_Q(t) = s_R(t) \otimes Q_M(t) \quad \mathbf{1-8}$$

where $s_R(t)$ is the received signals, $I_M(t)$ and $Q_M(t)$ are the I- and Q- channel matched filters. The demodulated signal $r_I(t)$ and $r_Q(t)$ is then down-sampling and de-mapped. Figure 1.11 describes the schematic of CAP signal demodulation.

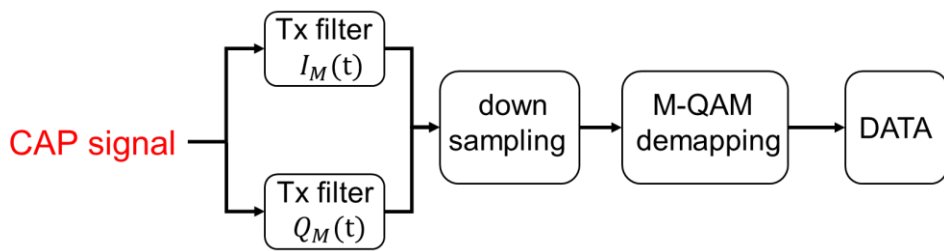


Figure 1.11: CAP signal demodulation

The I- and Q- channel matched filter can be expressed as:

$$I_M(t) = I(t) \quad \mathbf{1-9}$$

$$Q_M(t) = -Q(t) \quad 1-10$$

The matched filters are the time reverse version of the corresponding filter. In order to investigate the separation of the I- channel and Q-channel information, Figure 1.12 shows the convolution results of I- matched filter at Rx with Tx I- filter and Q- filter, respectively. For the I- filter, we have the pulse:

$$F_I(t) = I(t) \otimes I_M(t) = \begin{cases} 1, & t = 0 \\ 0, & t = nT (n \neq 0) \end{cases} \quad 1-11$$

‘0’ means there is no ISI from the adjacent symbols. For the Q- filter, we have the pulse

$$F_Q(t) = Q(t) \otimes I_M(t) = 0, t = nT \quad 1-12$$

Therefore, at each sampling point, the Q- channel information is all zero including the current symbol point $t=0$. Therefore, the I channel matched filter eliminates the information from the Q channel. The similar result can be obtained for the Q- channel.

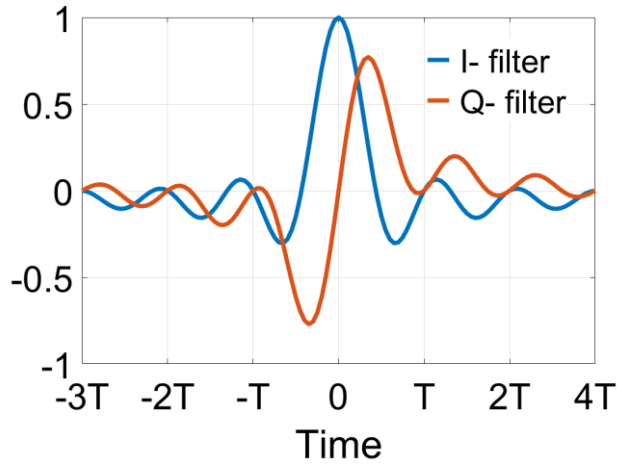


Figure 1.12: Convolution results of the I- filter or Q- filter at the transmitter side with the I- matched filter at the receiver side

The orthogonality is the key point to separate the I- and Q- channel perfectly. This can be further expressed in Equation 1-13 and Equation 1-14, which will be detailed discussed in Chapter 3.

$$\angle I_M(\omega) \equiv \angle Q(\omega) + \frac{\pi}{2} \quad 1-13$$

$$\angle Q_M(\omega) \equiv \angle I(\omega) + \frac{\pi}{2} \quad 1-14$$

1.2.3.2. CAP prospect for optical communication system

The carrierless amplitude phase (CAP) modulation format was proposed in 1975 by the Bell Labs as a viable modulation technique for high-speed communication links over copper wires [60]. CAP has not drawn much attention until the dawn of the digital subscriber loop (DSL) techniques that were aimed for private consumer asymmetric digital subscriber line (ADSL) [38, 39].

In [40], the quality shown by CAP has attracted interest for implementation in asynchronous transfer mode (ATM) local area networks standard application. Owing to its high bandwidth efficiency and low implementation costs, CAP has been adopted primarily and widely used for ADSL and ATM LANs. For high speed transmissions, CAP modulation has been demonstrated to be simpler and has better performance than discrete multitone (DMT) [41]. The interesting feature of CAP is the possibility to extend its signal basis to higher dimension for DSL application [42, 43]. The optimization algorithm has been used to extend the conventional 2D-CAP scheme to higher dimensionality and to assure perfect filter reconstruction. Furthermore, multiband-CAP has also been exploited to extend the system capacity to 102.4 Gb/s over 15 km of SSMF [44].

- **SSMF and MMF links**

In recent years, there is increasing interest to implement CAP modulation format in various optical communication system applications. Numerous studies between CAP and other modulation schemes also have been reported to show how CAP modulation format manage to outperform others. High speed of 40 Gb/s CAP-16 modulation over 10 km SSMF has been demonstrated for the first time, providing significant dispersion advantages compared to non-return-to-zero (NRZ) modulation [45]. It proves the feasibility of generating and decoding 40 Gb/s CAP channels using current low-cost transversal filters. A comparison of CAP and Discrete multitone (DMT) modulation (DC-biased optical OFDM) using VCSELS has also been demonstrated over MMF [46]. CAP achieved an improved of 0.7-1.1 dB

sensitivity and spectral efficiency than DMT. The spectral efficiency for DMT is reduced because of the addition of the cyclic prefix. It is believed that CAP can be viewed as an attractive alternative modulation format for optical in-home networks. Intensive theoretical investigations have been analyzed to compare the link power budget and power dissipation of NRZ, PAM-4, CAP-16 and 16-QAM-OFDM systems for data communication application [47, 48]. The results show that the CAP-16 scheme offers good performance and half the power consumption of optical orthogonal frequency division multiplexing (OOFDM) schemes over lengths up to 30 km at a 28 Gb/s data rate. For higher speed such 100 Gb/s, the comparison of link power budget and power dissipation have also been studied between CAP-16/64 and 16/61-QAM-OFDM systems over 2 km FEC enhanced SSMF links using direct modulation lasers [49]. Both CAP-16 (in conjunction with feed forward and decision feedback equalisation) and 16-QAM-OFDM can support transmissions over 5 km of SSMF, with power dissipation of ~ 2 times that of a 4×25 Gb/s NRZ system [49]. However, CAP modulation utilizes two orthogonal passband filters (in-phase and quadrature) to encode the baseband signal rather than employing sine and cosine carriers and is easier to implement than quadrature amplitude modulation (QAM) schemes.

- **POF links**

SI-POFs are also an attractive transmission medium for high speed in-home optical networks due to their easy installation and low cost properties [50]. LED is used as an optical source for POF links to sustain the system cost-effectiveness, ease of system installation and maintenance. The main challenge arising in the link is to achieve high system capacity due to limited bandwidth of LED and SI-POF itself. A straightforward way to increase system capacity is to improve the system spectral efficiency by enabling the same bit rate to be transmitted using a reduced bandwidth. The implementation of the CAP modulation format in a SI-POF link can be an appealing approach to increase the bandwidth efficiency while maintaining its relatively low complexity and low energy cost system. A record high error free transmission without forward error correction (FEC) over 50 m SI-POF at 1.5 Gb/s has been experimentally demonstrated with the CAP-16 modulation scheme using a low-cost commercially resonant cavity light emitting diode (RC-LED) [51]. In [52] and [53], comparisons between gigabit NRZ, CAP and Optical OFDM systems over FEC enhanced 50 m POF links at 2.1 Gb/s with LEDs have been studied. The results show that CAP-64 outperforms both NRZ and optical OFDM scheme for all POF lengths and supports a record high data rate of 3.5 Gb/s bidirectional and 2.1 Gb/s unidirectional

transmission over 50 m POF. The unidirectional 2.1 Gb/s transmission over 50 m POF achieved by CAP-64 increases capacity by 70% compared to the published best performance of 1.25 Gb/s NRZ signal over 50 m POF unidirectional transmission [54]. These results indicate that CAP modulation provides great potential in terms of signal capacity and power efficiency for LED based POF links. On the other hand, a comparison between CAP and PAM modulation schemes for data transmission over SI-POF has been also illustrated [55]. Using the CAP-16 modulation scheme over 50 m POF link at 5 Gb/s, the measurement results show that CAP offers potentially the same spectral efficiency as a corresponding M-PAM modulation format and provides slightly better performance given a high SNR.

- **Wireless LED-based links**

LED-based wireless visible light communication has also attracted considerable interest in recent years as an alternative solution in next generation indoor wireless LAN in regards to the LED capability to simultaneously provide illumination and communication. Spectral efficient modulation formats like CAP can be employed to increase the link capacity due to the severe bandwidth limitation caused by LED in a VLC system. In [56], a performance comparison between the CAP signal and OFDM signal over high capacity RGB-LED-based WDM visible light communication (VLC) on 25 cm air-transmission has been made. The maximum data rates achieved by CAP and OFDM were 3.22 and 2.93 Gb/s, respectively. The CAP scheme gives competitive performance and provides alternative spectrally efficient modulation for next generation optical wireless networks compared to OFDM. Furthermore, a white phosphorescent LED at data rates of 450 Gb/s on 30 cm air-transmission has been reported [57]. DMT performance was substantially worse than the performance of CAP modulation.

In conclusion, the CAP modulation scheme has gained serious interests in the research community due to its high spectral efficiency, potentially low cost implementation and simplicity compare to modulation formats with carriers. Numerous papers have investigated the employment of the CAP modulation format in standard single mode fibre (SSMF), multimode fibre (MMF) and polymer optical fibre (POF) links. Comparisons of CAP against other schemes also have been demonstrated and the results demonstrate that CAP is an alternative modulation format candidate with competitive performance in optical transmission applications. However, the significant drawback of the CAP based system is that a flat channel frequency response is required. The non-flat frequency response of the transmission system will significantly degrade the system performance. Therefore, in this thesis, a novel equalisation method is

proposed and tested in CAP-based optical data transmissions.

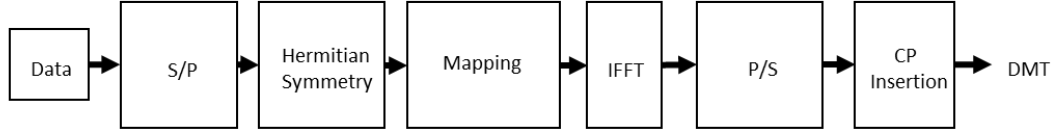
1.2.4. Discrete Multitone (DMT) Modulation

Discrete multitone modulation has been widely adopted in various digital subscriber line applications [58]. This multi-carrier modulation scheme uses a large number of individual carriers to carry the information. DMT can exploit a transmission bandwidth much larger than 3 dB and cope with severe channel conditions. For multimode glass fibre and POF links, DMT transmission has been demonstrated, achieving ~100 Gb for the OM4 based link and gigabit transmission over POF link using LED.

Figure 1.13 shows the block diagram for the generation of a DMT signal based on M subcarriers. The sequential data stream is converted to $(M/2-1)$ data streams. For each subcarrier, the data is encoded based on the modulation selected. The bit-loading method is used which depends on the received SNR to optimize the link performance based on the training sequences consisting of only QAM-4 modulation. For an intensity modulation and direct detection (IM/DD) system, a real-valued DMT signal is required in order to directly drive the optical transmitter. A Hermitian symmetric vector with M components is employed based on the encoded $(M/2-1)$ components of the complex symbol sequence. A real-valued vector is formed by using M -point inverse fast Fourier transform (IFFT) over the Hermitian symmetric vector. A cyclic prefix is inserted to the beginning of the time domain vector preventing the inter-block-interference and then converted to analogue signal for transmission. At the receiver side, an analogue-to-digital (ADC) is used to digitize the received signal. Then the CP is removed and a fast Fourier transform (FFT) is used to convert the time domain signal into the frequency domain. A simple one tap equaliser is employed to recover the signal. The data for each subcarrier is then decoded and a parallel to serial conversion is employed.

The principle of DMT scheme is to combat the link ISI by transmitting many slower modulated subcarriers and using the cyclic prefix. Therefore, it can explore the bandwidth much larger than 3 dB bandwidth of the link with only one tap equaliser. However, the DMT scheme is more complicated than other schemes such as PAM and CAP, and thus requires higher cost and higher energy consumption.

DMT modulation



DMT demodulation

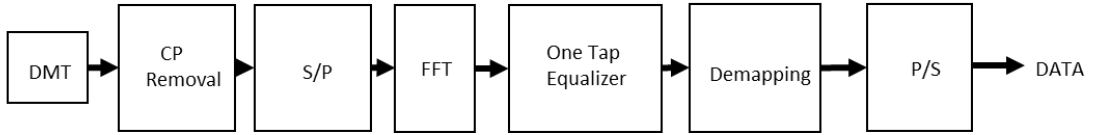


Figure 1.13: Block diagram of DMT modulation and demodulation (S/P: serial to parallel conversion, P/S: parallel to serial conversion, CP: cyclic prefix)

1.3. Mode division multiplexing (MDM) technique

Mode division multiplexing (MDM) is able to increase the bandwidth of the optical fibres by using a single mode or groups of modes to transmit separate data signals in MMF by precise engineering of the launch field. It can be achieved by the spatial light modulator (SLM) [59, 60]. SLM can alter the amplitude and phase of the spatial electric field of the laser, which can be used to design the incident field coupled into an MMF. The desired incident field into an MMF can be coded on the SLM with a priori knowledge of the theoretical inherent field of the MMF [59, 61] or without a priori knowledge by adaptive techniques [60]. Adaptive techniques were proposed to compensate for modal dispersion by using an SLM in MMF. In [62], five adaptive optics configurations were proposed with control permitted over polarization or block wise polarization to minimize modal dispersion. In [63], a reconfigurable SLM based on a mode demultiplexer is able to produce the required spatial filter to accurately excite such modes sharing an azimuthal index.

1.4. offset launch

MMF suffers from mode coupling resulting from random geometrical perturbations in the structure,

particularly at the center of the MMF core. Offset launch is an effective method to avoid beam projection on these perturbations at the MMF core. In the offset launch, a small laser beam is projected to a spot radially offset from the core center [64]. Only a subset of higher-order modes of the total angular span is excited, which have close propagation delays. Therefore, the modal dispersion can be reduced [65-67]. In [68] [69], a novel practical MMF offset launch scheme was demonstrated by selectively exciting one dimensional fifth-order Hermite-Gaussian (HG) modes using a passive beam shaper formed on a fused silica substrate. It achieved 10 Gb/s data transmission over 220 m of MMF. In [59], HG first-order mode, second-order mode, and third-order mode in dual launches over 250 m were demonstrated while 2D- HG modes were excited achieving a transmission rate of 20 Gb/s over a same distance [60].

1.5. Organizations and contributions of the dissertation

1.5.1. Chapters Organization

Chapter 1 gives an overview of the historical development of optical communications and worldwide data traffic demands nowadays over the optical networks today. The multimode glass fibre link and POF link have been introduced. Advanced modulation formats with high spectral efficiency have also been illustrated.

Chapter 2 reviews the fundamentals of multimode glass fibre and POF links including VCSEL, LED, MMF, POF, and PIN/APD receiver.

Chapter 3 proposes and introduces a novel CAP equaliser on a VCSEL based OM4 fibre link. The theoretical modelling and experimental work are carried out to evaluate the link performance. 112 Gb/s data transmission over 150 m OM4 fibre is demonstrated within hard decision forward error correction (HD-FEC) using the CAP equaliser in conjunction with the CAP-16 modulation scheme.

Chapter 4 uses the CAP equaliser on LED based POF link together with an APD receiver. Simulation work on the CAP equaliser and conventional equaliser is detailed studied. The link performance is evaluated by the BER performance at various average optical received power. The CAP equaliser experimentally achieved 4 Gb/s data transmission over 25 m POF and 5 Gb/s over 10 m POF using CAP-16 modulation scheme.

Chapter 5 presents a novel pre- FFE CAP equaliser solving the crosstalk issue at the transmitter side. 56 Gb/s data transmission over 100 m OM4 fibre is demonstrated experimentally and simulation work at a 112 Gb/s data rate over 100 m OM4 fibre is evaluated. A 2 dB improvement of received sensitivity is demonstrated over post- CAP-equaliser at 112 Gb/s over 100 m OM4 fibre.

Chapter 6 proposes a new structure of artificial neural network which further eliminates the nonlinear effects of the link and achieves a 2.4 dB improvement over the CAP equaliser. Moreover, a compact silicon optical equaliser for 50-Gbaud IM/DD is also demonstrated.

Chapter 7 concludes and summarizes the high speed data transmission demonstrations presented in this dissertation. The outlook for future work related to the proposed approaches for further improvements is also discussed.

1.5.2. Contributions of the Dissertation

The main contribution of this dissertation is listed with respect to the system on two different types of multimode waveguides (OM4 and POF).

For multimode glass fibre (OM4) links:

- For the first time, a novel CAP equaliser is proposed and used in the VCSEL based OM4 fibre link for the purpose of solving the crosstalk issues due to the nonlinear phase response of the link. The link performance is also evaluated using DMT scheme. 112 Gb/s data transmission over 150 m OM4 fibre is experimentally achieved within HD-FEC using CAP-16 modulation format.
- For the first time, a novel pre-feed forward equaliser in conjunction with CAP modulation scheme is proposed and tested in the purpose of solving the crosstalk issues at the transmitter side. 56 Gb/s link performance has been experimentally demonstrated. A 2 dB sensitivity improvement is achieved compared to the post- CAP equaliser at 112 Gb/s over 100 m OM4 fibre via simulation.
- For the first time, an artificial neural network (ANN) combined with the CAP equaliser structure has been proposed in order to further eliminate the nonlinear effect of the system.

An improvement of 2.4 dB sensitivity is achieved compared to the CAP equaliser at 112 Gb/s over 100 m OM4 fibre.

- An ultracompact monolithically integrated silicon optical equaliser that used for 50Gb/s transmission system has been experimentally demonstrated.

For POF based links:

- For the first time, 4 Gb/s over 25 m and 5 Gb/s over 10 m POF is achieved using CAP-16 modulation format in conjunction with CAP equaliser. The simulation and experimental results are detailed studied, and the performance of the CAP equaliser has been compared with that of the conventional equaliser over various lengths of POF (1 m, 10 m and 25 m) at 4 Gb/s.

CHAPTER

2

PRINCIPLES OF MULTIMODE FIBRE LINKS

This chapter illustrates the fundamentals building blocks of the VCSEL-MMF link and LED-POF link including VCSEL, LED, MMF, POF and both PIN/APD receivers. OM4 fibre is used in this work owing to its high bandwidth. SI-POF with 1 mm core diameter is chosen for the high speed PMMA-based link because of its low cost. For the receiver, the principles and noise performance of both PIN-based and APD-based receivers are discussed in detail.

2.1. Introduction of multimode waveguides

The optical waveguides were investigated in the form of a transparent rod, which was proposed in 1910 [70] and then demonstrated in the experimental work by Schrieffer in 1920 [71]. However, due to the excessive losses, these transparent dielectric rods were proved to be impractical. In 1966, a serious proposal published by Kao [72] described the optical fibre as a clad waveguide and predicted the utilization of the optical fibre as a practical communication medium, even though the attenuation was as high as 1000 dBkm^{-1} . Kao proved in his paper that the high fibre loss is due to waveguide material impurities, resulting in huge efforts to improve refining technique on the conventional glass. As the technique developed, the fibre loss was achieved as low as 0.2 dBkm^{-1} for the wavelength of 1550 nm [73]. This technology evolution started a new era of light wave communication. A multimode optical waveguide is normally cylindrical and dielectric, which confines electromagnetic energy and guides the light in the direction parallel to the optical axis [74]. Generally, the fibre consists of a core layer which is surrounded by a cladding layer. The refractive index is different between the core and cladding layer. The light is confined in the core area for propagation along the waveguide due to the total internal reflection at the cladding incidence. Besides this confinement, the cladding layer can reduce scattering loss and protect the core from the contaminated outside environments. Two commonly multimode glass fibre types are distinguished by the material index profile (Figure 2.1). The left side is called step-index multimode fibre which has a constant refractive index n_1 in the central core area and n_2 at the cladding layer, where n_2 is smaller than n_1 . The right side shows a more advanced type of fibre called graded-index fibre which has the core index $n_1(r)$ as a function of the radial distance from the centre. The refractive index has the highest value at the core centre and gradually decreases along the fibre radius to the boundary of core and cladding. The index remains constant in the cladding layer. This graded-index can theoretically equalize the group velocities of different excited modes and therefore minimizes the modal dispersion. However, in practice, the refractive index defects from the fabrication process cannot be avoided, resulting in an effective modal bandwidth not exceeding $\text{GHz}\cdot\text{km}$ for a graded-index multimode fibre.

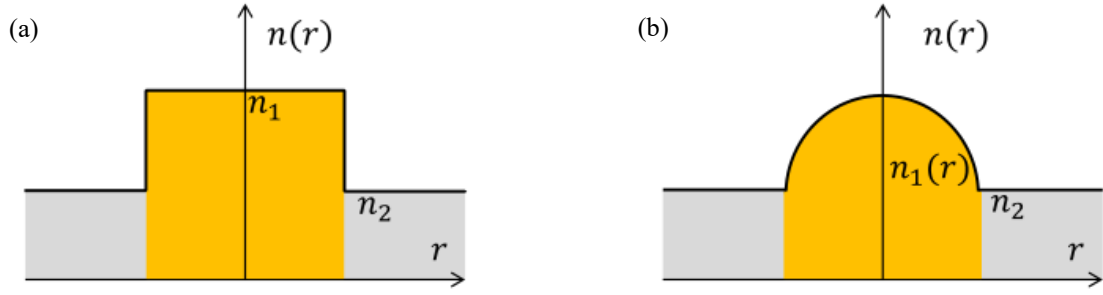


Figure 2.1: Refractive index profiles of (a) step-index and (b) graded-index multimode glass fibres

Graded-index fibre is investigated in the thesis as it provides less modal dispersion and therefore larger bandwidth than the step-index fibre. OM1, OM2, OM3 and OM4 fibre are four commonly used graded-index fibre, which has been detailed introduced in Chapter 1. To achieve single lane >100 Gb/s data transmission, the performance of the OM4 fibre is explored in the thesis.

Recently, another type of multimode optical waveguide from polymer material has attracted increasing research interests owing to its potential applications for the next generation of low cost and high speed networks in home and vehicles. This type of multimode waveguides is called plastic optical fibre. The first POF link was introduced in the late 1960s with the attenuation loss larger than 1000 dB/km due to the incomplete purification of the material used. Although the loss was further reduced to 125 dB/km, glass fibres with attenuation below 1dB/km are still widely available and dominate in the high speed short distance communication system. At the same time, for short reach applications like local area networks, copper cables are good enough for the data rate of tens of Mb/s. Therefore, the development of POF slowed down for quite a long time. However, the new technologies such as Internet require a higher data rate for short distance link in 1990s. New services such as video streaming, file sharing and cloud computing made a huge consumption of bandwidth. With the development of fabrication technologies, POF has been considered as a potential optical transmission medium for short distance owing to its comparable bandwidth to copper cable and easy installation. Moreover, POF is cheaper than copper cable and less fragile than glass fibre[75].

PMMA has become one of the most well-known materials used for POF. Although other materials like polystyrene polymers [76, 77], deuterated polymers [38] are also used for POF, PMMA-based POF is the most popular solution for high speed data communications with its low cost and mature technology. Similar to the multimode fibre, the core profile of the POF can either be step-index or graded-index. The

SI-POF has a core of 980 μm in diameter while the graded-index has a core diameter of 500 μm and 125 μm cladding layer. Although the GI-POF provides a higher bandwidth, the price is relatively high due to more complicated fabrication process. The SI-POF is much cheaper with a bandwidth distance product of $\sim 10 \text{ MHz}\cdot\text{km}$. Therefore, SI-POF is the low cost solution to provide high data rate links in both home and vehicle networks.

2.1.1. Multimode glass fibre

- Graded-index Multimode Glass fibre

Graded-Index multimode fibre has a maximum refractive index at the core centre and it gradually decreases to its minimum refractive index along the fibre radius to the cladding layer. The index profile can be expressed as

$$n(r) = \begin{cases} n_{core}(1 - \Delta(\frac{r}{a})^\alpha)^{\frac{1}{2}} & r < a \\ n_{core}(1 - \Delta)^{\frac{1}{2}} & r \gg a \end{cases} \quad 2-1$$

where n_{core} is the refractive index at the core centre, a is the core radius of the fibre, r is the radial distance from the core centre, α is the profile parameter which decides shape of the profile and Δ is the relative difference of the refractive indices between the core and the cladding given by

$$\Delta = \frac{n_{core}^2 - n_{cladding}^2}{2n_{core}^2} \quad 2-2$$

The light propagation mechanism in a multimode fibre with a graded-index (parabolic) profile is illustrated in Figure 2.1(b). Theoretically, the light propagating in different paths through the multimode glass fibre with graded-index tends to arrive at the fibre end simultaneously (Figure 2.2). Therefore, the dispersion is small and high effective modal bandwidth can be achieved. The light travels through the longer path with smaller refractive index while shorter paths have the larger refractive index. The velocity of light in a certain material can be expressed as

$$v = \frac{c}{n} \quad 2-3$$

Therefore, the velocity of longer paths is higher than the shorter path and therefore the arriving time at the fibre end is equalized provided that a suitable profile parameter α is chosen. A parabolic graded index

profile is commonly used with $\alpha=2$ for various standard glass fibres.

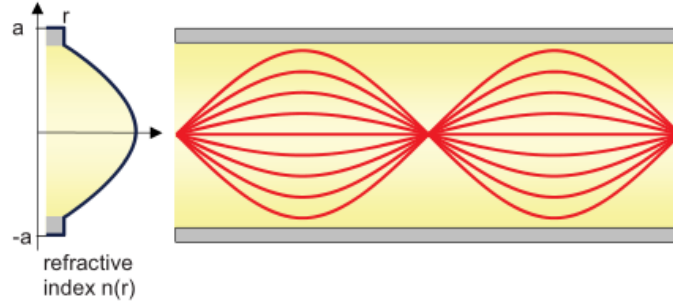


Figure 2.2: Schematic of light propagation in a grade-index multimode glass fibre

The ideal refractive index profile can be determined by mode field theory and all the excited modes of the multimode glass fibre can have the same group velocity along the propagation direction. However, the ideal refractive index strongly depends on the launching beam wavelengths and also fibre material properties and therefore is very sensitive to any subtle inaccuracies. Refractive defects cannot be avoided during the fibre fabrication process, which significantly affects the optimized refractive index. The supported modes are not able to achieve an equalized group velocity due to the refractive defects and the modal delays disperse. The launching power through different modes with different propagation speeds causes the dispersion of the transmission power at the fibre end. Furthermore, the increasing lengths of fibre result in larger modal delays and limit the link reach of a multimode glass fibre. When the modal delay is comparable to the bit period, the pulse distortion is obvious [78].

2.1.1.1 Chromatic dispersion

The frequency dependence of the group velocity results to pulse broadening simply because different spectral components of the pulse do not arrive simultaneously at the fibre output. This is called chromatic dispersion. If $\Delta\omega$ is the spectral width of the pulse, the extent of pulse broadening for a fibre of length L is determined by [79]

$$\Delta T = \frac{d}{d\omega} \left(\frac{L}{v_g} \right) \Delta\omega = L \frac{d\beta^2}{d\omega^2} \Delta\omega = L\beta_2 \Delta\omega \quad 2-4$$

where ω is the angular frequency, β is the phase constant, the group velocity $v_g = \frac{d\omega}{d\beta}$, and $\beta_2 =$

$\left(\frac{d\beta}{d\omega}\right)^2$ is known as the GVD parameter, which determines how much an optical pulse would broaden on propagation inside the fibre. In the optical communication system, it is customary to replace the frequency spread $\Delta\omega$ by $\Delta\lambda$. By using $\omega = \frac{2\pi c}{\lambda}$ and $\Delta\omega = \frac{-2\pi c\Delta\lambda}{\lambda^2}$, Equation 2-4 can be written as 2-5

$$\Delta T = \frac{d}{d\lambda} \left(\frac{L}{v_g} \right) \Delta\lambda = LD\Delta\lambda \quad 2-5$$

$$D = \frac{d}{d\lambda} \left(\frac{1}{v_g} \right) = \frac{-2\pi c}{\lambda^2} \beta_2 \quad 2-6$$

where D is called the dispersion parameter and is expressed in units of ps/(km-nm) defined in 2-6.

In this thesis, the OM4 fibre is used and this type of multimode fibre is designed to be laser optimized.

Considering the narrow spectral width of the 850 nm VCSEL, the chromatic dispersion is relatively small compared to the modal dispersion when using an 850 nm VCSELs as the transmitter.

2.1.1.2 Attenuation

In order to achieve reliable communications, the optical receiver requires a certain level of received optical power to achieve an acceptable signal-to-noise ratio. However, fibre attenuation reduces the transmitted optical power which can directly decide the feasibility of an optical link. In order to obtain a high SNR and a smaller attenuation is always preferred. The fibre attenuation is normally expressed in decibels and defined as the power ratio between the launched power and the received power at the fibre end, which can be written as

$$loss (dB) = 10 \log_{10} \left(\frac{P_{in}}{P_{out}} \right) \quad 2-7$$

If the fibre length is considered, the output power in terms of the input power can be expressed as

$$P_{out} = P_{in} e^{-\alpha L} \quad 2-8$$

where L is the fibre length and α is the attenuation coefficient.

The dB/km is used to express the fibre loss in practice. Combined Equation 2-7 and 2-8

$$\frac{loss}{L} (dB/km) \approx 4.34 \alpha \quad 2-9$$

The major mechanisms for the fibre loss are material absorption, Rayleigh scattering and waveguide

imperfections. The first two cases are wavelength dependent. For the OM4 fibre, the loss at 850 nm wavelength is the first low loss window (2.5 dB/km) and this wavelength is chosen for use in conventional optical systems.

2.1.1.3 Mode groups

In the multimode fibre, the total number of modes supported in a graded-index multimode glass fibre with profile α can be expressed as

$$M_\alpha = \frac{\Delta\alpha}{(2 + \alpha)} a^2 k_0^2 n_{core}^2 \quad 2-10$$

where n_{core} is the core index and k_0 is the wave number, a is the fibre core radius. A group of modes sharing the same mode group number M have the same propagation constant β_M given a specific fibre geometry, which is defined as

$$\beta_M = n_{core} k_0 \sqrt{1 - \Delta \left(\frac{M}{M_\alpha} \right)^{\frac{\alpha}{\alpha+2}}} \quad 2-11$$

The mode group number M can be defined as [80]

$$M = 2\mu + \nu + 1 \quad 2-12$$

where ν is the azimuthal order that decides the number of separations ‘cut’ by the diameter axes of the fibre cross section and μ is the number of radial layers in the profile. The modes with same group have nearly the same differential modal delay and the modal dispersion can be only considered in the differential modal delay between different mode groups.

2.1.1.4. Intermodal dispersion and differential modal delay

The bandwidth of the multimode glass fibre is mainly limited by the intermodal dispersion. Although the design of an ideal graded-index fibre can equalize the arrival times at the fibre output for different mode groups theoretically, the inevitable index defects cause the differences in mode group delays, resulting in dispersed arrival times of the power propagating through different mode groups. The initial

launched pulses will be spread in time, which is a major cause of the signal distortion in multimode fibre links. This is called the pulse broadening effect. The group delay is defined as the first order derivative of the propagation constant in terms of the angular frequency [81].

$$\tau_{group,M} = \frac{d\beta_M(\omega)}{d\omega} \quad 2-13$$

where M is the mode group number. This group delay represents the time required for the light to travel through a unit length of the fibre for the group number M . When a Dirac pulse is transmitted through a particular mode group, the received pulse at the position z along the longitude direction is expressed as

$$h_M(z, t, \omega) = \delta[t - z\tau_{group,M}(\omega)] \quad 2-14$$

where $\delta(t)$ represents the Dirac transmitted pulse. The launched optical pulse excites different mode groups which depend on the injecting beam profile. By defining the power coefficient of each mode group and assuming that the power combination of different modes is linear, the overall impulse response of the multimode glass fibre can be written by

$$h_{fibre}(z, t, \omega) = \sum_{M=3}^{M_{max}} C_M \delta[t - z\tau_{group,M}(\omega)] \quad 2-15$$

The M starts from 3 as the lowest mode group number when the minimum radial order and azimuthal order are 1 and 0, respectively. The differential modal delay is another factor to quantize the mode group delay characteristic. In order to define this, an average group delay is firstly calculated using

$$\tau_{average}(\omega) = \sum_{M=3}^{M_{max}} C_M \tau_{group,M}(\omega) \quad 2-16$$

The average group delay depends on the specific mode group power distribution condition. The differential modal delay (DMD) can then be defined following the definition of standard deviation in statistics.

$$DMD = \sqrt{\sum_{M=3}^{M_{max}} C_M [\tau_{group,M} - \tau_{AVERAGE}]^2} \quad 2-17$$

A large differential modal delay indicates that group velocities of the excited mode groups are widely spread. A small differential modal delay implies that the excited mode groups have close propagation

constants. If there is a large differential modal delay, the launched optical impulse will be dispersed widely over time. Meanwhile, the fibre bandwidth is severely limited by the pulse broadening effect.

2.1.1.5. Multimode fibre standard

The four generation of graded-index multimode fibre are OM1, OM2, OM3 and OM4 fibres with increasing bandwidth-distance products. The OM1 fibre has 62.5 /125 μm core/cladding diameter. All the other three types characterize the fibres with 50/125 μm core/cladding diameter [82].

OM2 fibres are widely used in today's local area networks in combination with 850 nm VCSELs for 10 Gbits/s applications. However, OM2 fibre can only achieve 150 m at this speed while the OM3 and OM4 fibre can extend the distance to 300 m and 550 m. For the recently published 40 GbE and 100 GbE standards, OM3 and OM4 can support up to 100 m and 150 m respectively. OM1 and OM2 are no longer used at these data rates due to their insufficient link budget. 40 GbE and 100 GbE devices will gradually replace the 10 GbE devices. It has been recommended to industrial ventures that OM3 and OM4 should be used for all new installations [83].

2.1.2. Plastic optical fibre

Today, there are two main core materials used for POF: polymethyl methacrylate (PMMA) and perfluorinated polymers [23]. PMMA is commonly used for short-range (up to 100 m) applications in home networks, digital home appliances and automotive networks (MOST) while the perfluorinated polymers are commonly used for higher speed applications such as building LAN wiring [84-86] and data centre wiring and therefore come at much higher cost than PMMA.

In this work, the traditional PMMA POF is studied and the POF refers to PMMA POF if not otherwise mentioned.

2.1.2.1. Attenuation in POF

Figure 2.3 shows the attenuation rates of the PMMA POF against operating wavelengths. This is caused by the absorption spectrum of the PMMA material. The windows for transmission with the lowest

attenuation are around 520 nm, 570 nm and 650 nm[23]. Even in the best scenario, the attenuation rate of a PMMA POF is still hundreds of times higher than that of a glass fibre. Currently, 650 nm is the most commonly used band for POF applications due to the availability of commercial optical sources. Recently, the development of μ LEDs with diameters $\leq 100 \mu\text{m}$ at blue wavelengths shows the potential to employ the other low attenuation windows of the POF.

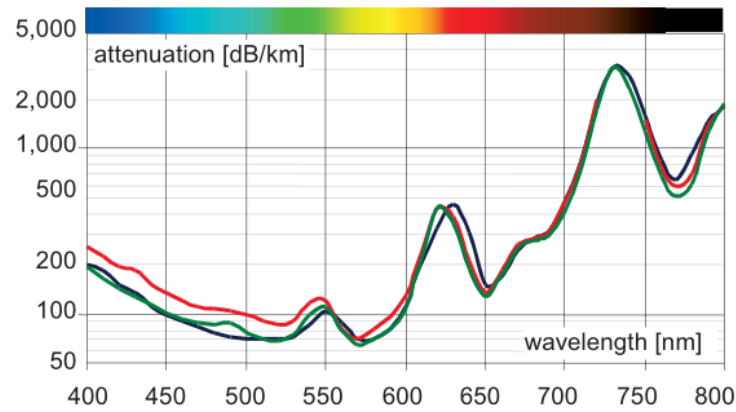


Figure 2.3: Attenuation of different standard-NA SI-POF (measurement by POF-AC) [23]

2.1.2.2. Structure and Profile

The POF usually consists of three layers: the core, the cladding layer, and the protecting jacket. The core is surrounded by the cladding layer which has a lower refractive index. As illustrated in Figure 2.4, Light is confined within the core by total internal reflection. This occurs when the light propagates in a medium with a higher refractive index (n_1) and reaches an outside boundary with a medium of a lower refractive index (n_2). If the incident angle is greater than the critical angle, the light will be entirely reflected with no wave passing to the cladding. This critical angle depends on the refractive index of the two media:

$$\theta_c = \tan^{-1}\left(\frac{n_1}{n_2}\right) \quad 2-18$$

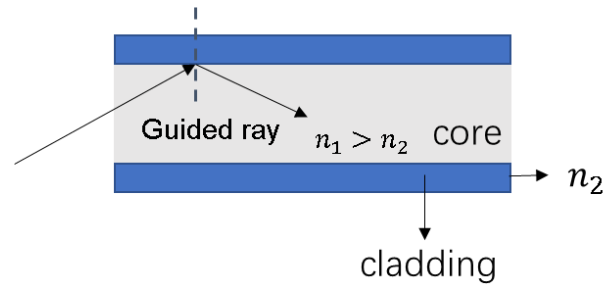


Figure 2.4: illustration of total internal reflection and light confinement within the fibre

Based on the index profile of the core, POF can be further classified as step-Index (SI) POF, multi-step-index (MSI) POF, and graded-index (GI) POF [23, 87].

- **SI-POF**

Figure 2.5 shows the structure and profile of a SI-POF. The refractive index of SI-POF has an abrupt change at the core-cladding interface [88, 89]. Parameters of SI-POF have been standardized by the IEC in 2008 [90] and the core diameter of a SI-POF is usually 980 μm with the cladding layer (10 μm) surrounded. Therefore, the overall diameter is around 1 mm which is 1000 times of that of a single-mode fibre. This makes the installation and light coupling into POF much easier. However, a typical launch can excite tens of thousands of modes and result in multimode dispersion [84]. Therefore, this large mode dispersion significantly reduces its bandwidth [91].

The commercially POF based system can operate up to 100 Mb/s with lengths up to 80 m, and the possibility to reach much more than 100 m has also been demonstrated [92, 93]. The SI-POF has shown a great potential for the next generation short range high speed applications using advanced modulation schemes[55].

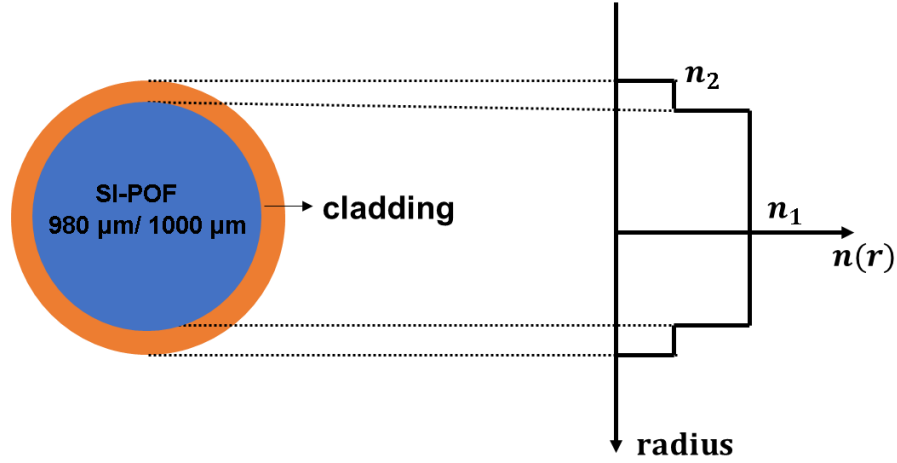


Figure 2.5: structure and refractive index profile of SI-POF

● GI-POF and MSI-POF

The difference between the GI-POF and SI-POF is the refractive index profile. For GI-POF, the refractive index decreases gradually inside the core instead of a constant one for the SI-POF. It was developed to have greater bandwidth than SI-POF [94-96]. The refractive index difference defines the group velocity and by speeding up rays with longer path lengths, the time delay of different beams is reduced, which results in a smaller dispersion compared to SI-POF. The complex refractive index pattern allows an increased bandwidth and also a reduced bending loss. GI-POF based high speed data transmission has been studied [97-99]. However, GI-POF is more expensive [100].

The MSI-POF was brought to the market in the 1990s. It is designed with a core consisting of many layers. For each layer, the refractive index decreases from the centre [101-103]. The fibre combines the advantages of relatively simple fabrication process of SI-POF with the higher bandwidth of GI-POF. The stair-like approximation to a GI-POF increases the bandwidth of the fibre and the fabrication of MSI-POF is similar to that of SI-POF.

2.1.2.3. Comparison of SI-POF, GI-POF, multimode glass fibre (MMF), standard single mode glass fibre (SSMF) and copper coaxial cable

Table 2-1 compares the properties of SI-POF, GI-POF, multimode glass fibre (MMF), single-mode fibre (SSMF) and copper coaxial cable (RG-6). SI-POF has the largest numeric aperture providing

relaxed alignment requirement and easy installation in comparison with MMF and SSMF. The small bending radius also makes POF suitable for home and automotive networks. This work has concentrated on achieving high speed short reach transmissions with low-cost components. Therefore, SI-POF is investigated for this thesis.

Table 2-1 Comparisons of SI-POF, GI-POF, MMF, SSMF, and RG-6[104]

Parameters	SI-POF	GI-POF	MMF	SMF	RG-6
Core diameter	0.98 mm	0.9 mm	0.05 mm	0.01 mm	1 mm
Cladding diameter	1 mm	1 mm	0.125 mm	0.125 mm	NA
Jacket diameter	2.2 mm	2.2 mm	2.5 mm	2.5 mm	8.4 mm
Signal type	Optic	Optic	Optic	Optic	Electrical
Attenuation	165dB/km	165 dB/km	3 dB/km	<1dB/km	<1dB/km
Bandwidth	10MHz/km	150 MHz/km	>1GHz/km	>5GHz/km	7MHz/km
Alignment tolerance	High	Medium	LOW	LOW	Medium
Numeric aperture	0.5	0.35	<0.2	<0.13	NA
Min bending radius	2.5 cm	2.5 cm	5 cm	5 cm	20 cm

2.1.2.4. Mode and dispersion of SI-POF

The light propagation in a fibre follows Maxwell's equations. Optical modes are solutions that satisfy the boundary conditions. The spatial distribution of a specific optical mode does not change with propagation. In a step index circular waveguide, the number of modes depends on normalized frequency V , which is a function of the wavelength of light (λ), the fibre radius (a), and the refractive index of the core (n_1) and cladding (n_2):

$$V = \frac{2\pi a}{\lambda} \sqrt{n_1^2 - n_2^2} \quad 2-19$$

For the SSME, the value of the normalized frequency is usually < 2.405 . If $V \gg 1$, the number of modes M can be deduced from 2-10 ($\alpha \rightarrow \infty$) expressed as:

$$M = \frac{k_0^2 a^2}{2} (n_1^2 - n_2^2) = \frac{V^2}{2} \quad 2-20$$

where k_0 is the wave number. The POF used in this work is ESKA™ Mega SI-POF and the number of modes M can be estimated as 10^6 . Therefore, this large number of excited modes causes severe signal distortion on a POF based link. At the receiver end, different path lengths of the fibre modes arrive at different times, generating the modal dispersion. A graded index profile reduces this modal dispersion and therefore provides an increased bandwidth. Chromatic dispersion is another source of signal distortion and results from different wavelengths travelling with different speeds through POF.

2.1.2.5. Advantages of POFs

The large core size of SI-POF can provide great mechanical flexibility and a high numerical aperture (NA). POFs can be handled more easily than glass fibres and require less expensive tools for connection and splicing in comparison with those for glass fibres. With just a razor blade, POF can be easily cut and no cleaver and polishing tools are required.

POF products can even bend to 25 mm with no extra optical attenuation [105]. This makes POF an perfect solution for applications with a very tight bend radius where glass fibre products are not suitable. Owing to the flexibility and ease of handling, easier connectivity can be achieved, and DIY is possible for untrained people. In addition, the manufactory of POF is also not expensive. The large core size of

POFs does not require highly accurate alignment and therefore low-cost transmitters, connectors and receivers can be used for the POF links. Moreover, the maintenance of POF system is also much cheaper than glass or copper. Furthermore, POF systems provide better immunity to noisy electromagnetic interference from other appliances and parallel channels [104]. Therefore, POF can perform well in a deteriorating environment.

2.2. LED transmitters for POF links

The optical transmitter is used to convert the electrical signal into its optical part, which then propagates through the optical channel. An optical source is the major component of the optical transmitter. The optical source generation mechanism is based on two fundamental emissions: spontaneous emission and stimulated emission. For the spontaneous emission, an electron falls from an excited state to a ground state and emits a photon with a random propagating direction and therefore there is no apparent phase relationship with other emitted photons [106]. LED usually relies on this mechanism. The stimulated emission is generated by an existing photon which falls from an excited level and stimulates an electron, causing the generation of second photon. This process can be repeated to generate more photons. Lasers emit light through this process with narrower spectrum than that for spontaneous emission. The LED provides a rather large output beam size and therefore it is usually used in multimode waveguide systems. To support efficient data transmission over POF, LED sources with emission wavelengths matching the low attenuation windows of POF are required. Figure 2.6 shows the external efficiencies (data from the current datasheets of various manufactures) for available LED. The red light LEDs at 650 nm are the most commonly used with POF. With the rapid development of GaN/InGaN technology, the efficiency of an LED in the direction of the short wavelength spectrum has increased dramatically. It can be expected that the current gap will be closed into the red range. Blue LEDs in the range of 430 nm to 470 nm have also been used for POF systems. The attenuation of PMMA POF at 470 nm is indeed about 20 dB/km higher than at 520 nm, but the blue LEDs are considerably more efficient and as a rule can be modulated more quickly.

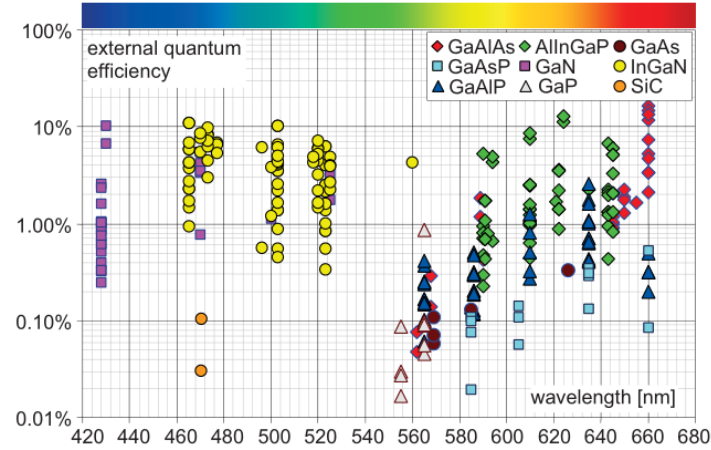


Figure 2.6: Efficiency of various LED material systems [23]

The modulation bandwidth of conventional LEDs is usually limited to $\sim 200\text{MHz}$ and LEDs are mainly used for low speed and low-cost applications. An overview of the switching speed of the available LEDs used for POF links at various wavelengths is illustrated in Figure 2.7. Diodes that have a lower efficiency usually exhibit very low switching speeds. GaN based LEDs are very well suited for data transmission due to their high switching speeds.

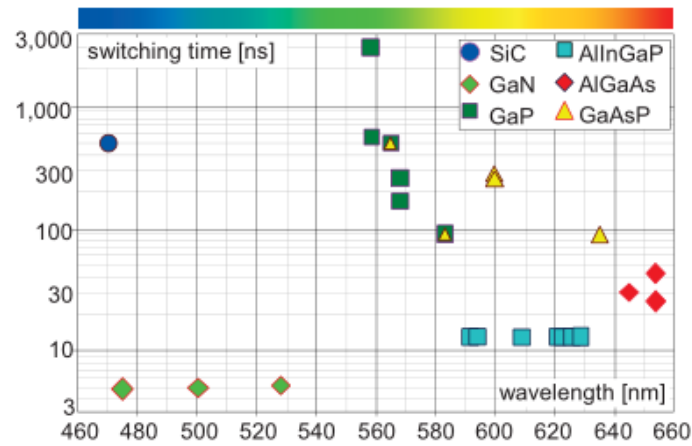


Figure 2.7: Switching times of various LED material systems [23]

In practice, the majority of commercially available POF transmitters are LEDs. The following advantages make LED attractive for POF based system.

Cost

The fabrication of the LEDs is much easier than laser diodes leading to reduced cost and high yields.

Reliability

LEDs are insensitive to gradual degradations and are able to provide long working lifetimes with reliable performance.

Temperature dependence

Compared to laser diodes, a change in temperature does not introduce much wavelengths shift. Figure 2.8 shows the temperature-dependent spectra of a blue LED (SHR700) in the -20 °C to + 70 °C range. The temperature compensation circuits are unnecessary, which leads to a simpler driving circuitry.

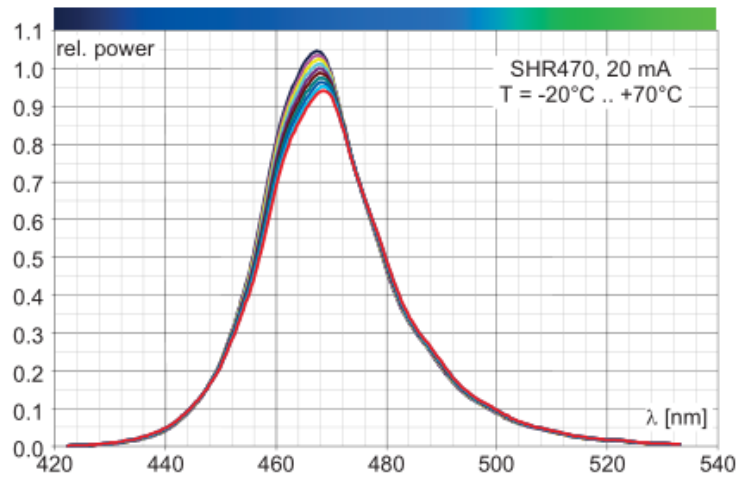


Figure 2.8: Spectrum of a blue LED (SHR470) [23]

Laser diodes have also been employed in system experiments at high data rate [107-109] owing to its larger bandwidth. In this work, POF links using LED transmitters are explored as they are eye-safe, and cost- and energy-efficient.

2.2.1. Resonant Cavity LEDs

Resonant cavity LEDs are becoming more and more popular for optical communications owing to their higher modulation bandwidths and radiation powers compared to conventional surface or edge emitter. Recently, the RC-LED has attracted intensive research interests on POF based system [104]. The basic structure of a RC-LED is shown in Figure 2.9, which consists of a micro-cavity with two parallel distributed Bragg reflectors and a multiple quantum well (MQW) surrounding the micro-cavity [110].

This structure amplifies the spontaneous emission from the high reflectivity of the bottom DBR by the self-photon-pumping and also makes the RC-LED a device with a narrower linewidth.

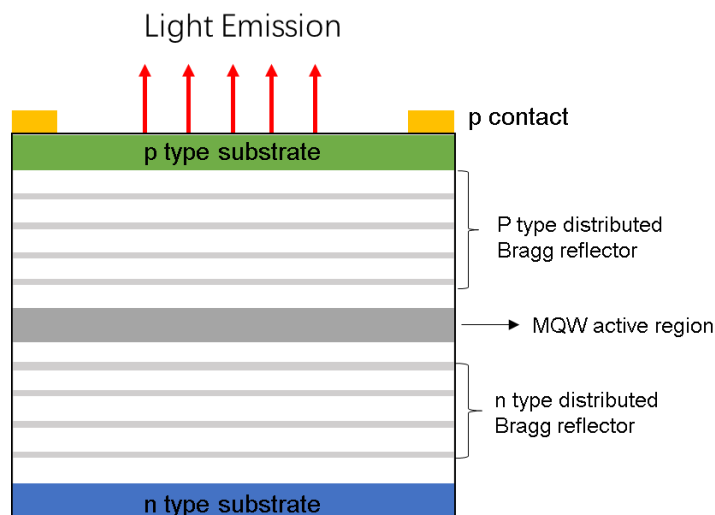


Figure 2.9: Structure of a RC-LED

2.2.2. μ LEDs

μ LEDs have been recently investigated for high speed POF links. In comparison with normal LEDs, the dimensions of μ LEDs are much smaller ($\leq 100 \mu\text{m}$). Intensive research has been carried out on μ LEDs due to their large bandwidth and high emission power. μ LEDs have great potential for both guided highspeed visible light communications (VLC) and free-space transmission. In this work, high speed POF links using μ LEDs are explored. The fabrication of μ LEDs devices is from commercially available epitaxial wafers grown on c-plane sapphire substrates using standard photolithography techniques [25, 111]. μ LEDs devices are usually fabricated into arrays with the multiple quantum well structure as the active regions. Figure 2.10 (b) shows a cross-sectional schematic of a GaN μ LED. For every pixel, there is only one common n-contact and the individual p-contact pad allowing each of them to be addressed individually. Figure 2.10(a) shows an image of a blue μ LED array. The μ LED arrays can be designed to a circular shape to match the geometry of a POF (Figure 2.10(c)). The micro-pixelated structure and their dimension make them compatible with CMOS control electronics which can be designed to drive individual pixels and achieve parallel data transmission using multiple μ LEDs [111].

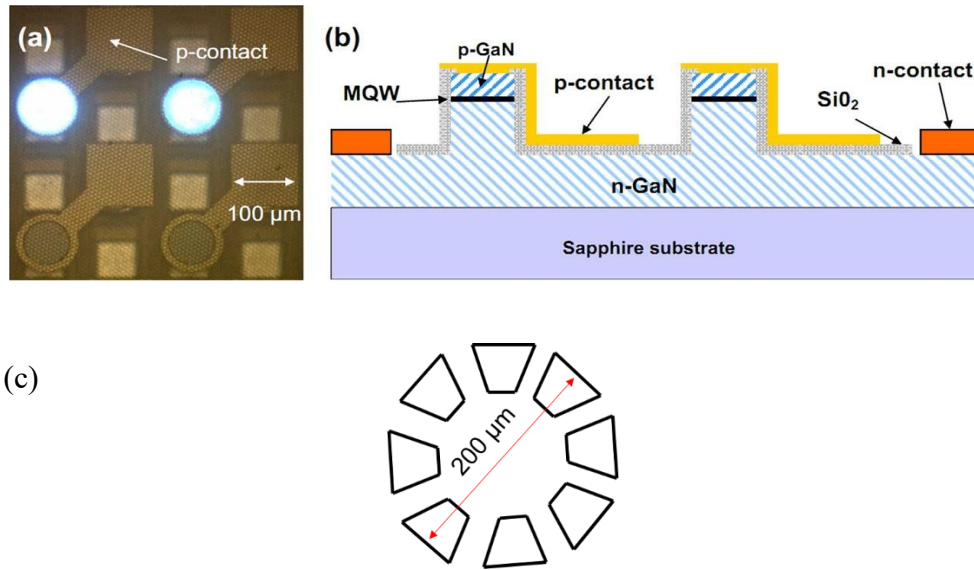


Figure 2.10: Schematic of (a) microscope image of a violet μ LED array (b) the cross-sectional of the μ LED array design and (c) the circular segmented μ LED arrays [111]

GaN μ LEDs allow solid-state visible light sources to be commercialized for multiple applications such as lighting, display and signaling due to their capability to generate light across the ultraviolet-blue-green part of the spectrum. Moreover, μ LEDs are also able to exploit the low-loss transmission windows of POF in the visible spectrum. μ LEDs exhibits high modulating bandwidths up to 400 MHz (Figure 2.11) due to their reduced pixel diameters and they are very attractive in use for high speed visible light communications [111].

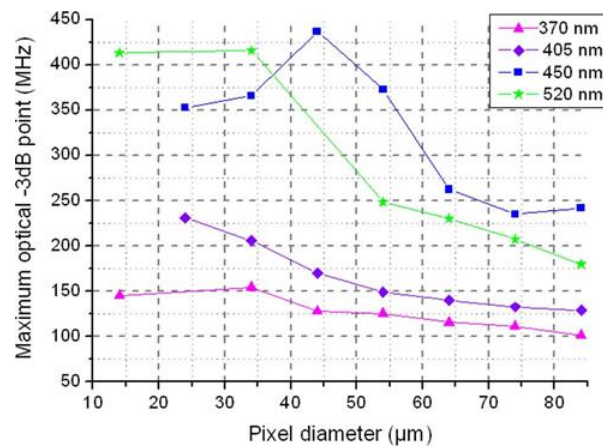


Figure 2.11: Maximum modulation bandwidths of μ LEDs of different diameters of the violet, blue and green μ LEDs [111]

2.3. VCSEL transmitters for MMF fibre links

Vertical-Cavity Surface-Emitting Lasers (VCSELs) were first invented in the mid 1980s, and soon became very popular for short reach applications such as fibre channels, intra-systems links and Ethernet. In 1996, VCSELs became an alternative solution for short range datacom and local area networks replacing edge-emitter lasers as they have lower manufacturing costs and higher reliability compared to the edge-emitters. VCSELs operating at the 850 nm wavelength are probably the most mature VCSEL technology to date as it has several fibre-based standards for short-haul datacoms. Products using 850-nm VCSELs for 10 Gigabit Ethernet have been commercially available on the market for some time [112].

2.3.1. Structure

Figure 2.12 shows the basic structure of a VCSEL. Semiconductor lasers consist of the substrate which has layers of semiconductor material grown on top. For VCSELs and also edge-emitters, this growth is finished in a molecular-beam-epitaxy or metal-organic-chemical-vapor-deposition growth reactor. In VCSELs, the active layer between two highly reflective mirrors (distributed Bragg reflectors) consists of several quarter-wavelength-thick layers of semiconductors of high and low refractive index alternatively. The mirrors reflectivity is between 99.5~99.9 %. Therefore, the light oscillates perpendicular to the layers and propagates through the top (or bottom) of the device. A p-on-n doping sequence is preferred to n-on-p owing to the usually lower defect densities of n-type substrate and reduced absorption of n-type mirrors [112]. Edge-emitters consists of cleaved bars dived from the wafers. Owing to the high index of refraction contrast between the semiconductor material and air, these two cleaved faces act as mirrors. Therefore, the light oscillates parallel to the layers, which differentiates the edge-emitters and the VCSELs.

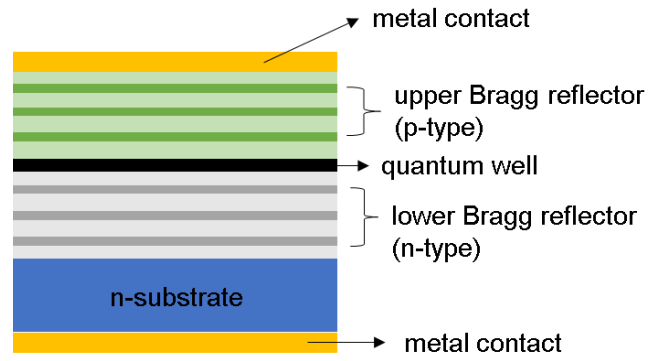


Figure 2.12: schematic of a VCSEL structure

2.3.2. VCSELs advantages

There are many advantages offered by the VCSEL technology which are summarized in the following aspects [113].

- **Wavelength stability**

The lasing wavelength is stable and is fixed by the short Fabry-Perot cavity. Figure 2.13 shows the emission spectrum of a 5 mm x 5 mm VCSEL array, resulting in spectral widths of 0.7~0.8 nm (full-width at half maximum). This 2-D VCSEL array are made of thousands of small, low single-mode power devices and its output can be focused into a very small, low-diverging spot using a micro-lens array / focusing-lens system. Therefore, this technology enables the coupling of ~100W power from a single source into a 400 μ m diameter fibre.

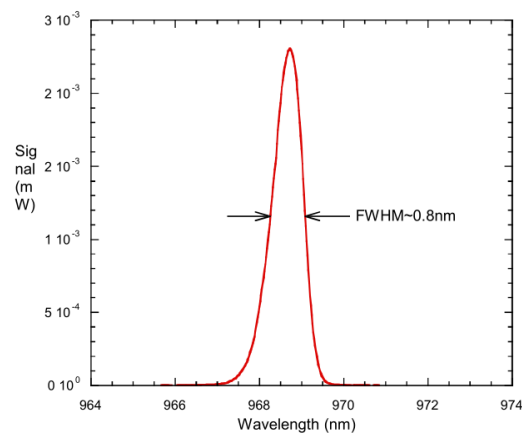


Figure 2.13: Emission spectrum of a 5 mm x 5 mm VCSEL array at 100 W output power (120A)

[114]

- **Wavelength uniformity and spectral width**

The growth technology has provided less than 2 nm standard deviation for the cavity wavelength, which allows for the use of 2-D arrays of VCSEL with very little wavelength variation between the elements of arrays. In contrast, the edge-emitter suffers from significant wavelength variations since there is no intrinsic mechanism to stabilize the wavelength and therefore a wide spectral width is generated.

- **Temperature sensitivity of wavelength**

The emission wavelength is much less sensitive (around 5 times) than the edge-emitters. The lasing wavelengths in VCSELS depends on the optical thickness of the longitudinal-mode-cavity which has a weak dependence on temperature. For the edge-emitters, the lasing wavelength is defined by the peak-gain wavelength which is more dependent on temperature. Over a 20 °C change in temperature, the emission wavelength in a VCSEL only varies by about 1.4 nm compared to the 7 nm variation for edge-emitters [113].

- **High temperature operation and high power emission**

VCSELS can be operated at temperatures up to 80°C without the use of a cooling system. Also, owing to their stable wavelength, the cooling system design can be considerably simplified. The VCSELS can have around 1200 W/cm² compared to the maximum 500 W/cm² delivered by edge-emitters.

- **Cost**

The simple processing and heat-sink technology make the package of 2-D VCSELS much easier than an equivalent edge-emitter bar-stack.

- **Reliability**

VCSELS are not subject to catastrophic damage and therefore it can achieve much higher reliability than edge-emitters.

- **Test**

The VCSELS can be tested on the wafer through a wafer probe machine, for lower costs and a simpler procedure that in turn raises yield for manufacturers. The edge-emitting lasers requires manufacturers to dice the wafers and mount the chips before the lasers can be tested, which drives up the costs.

2.3.3. Emission spectrum, L-I curve and bandwidth performance

Figure 2.14 shows the spectrum (a), LI curve (b) of the VCSELs used in the experiment bias at 12 mA. A peak value is achieved at 850 nm and threshold current is $< 2\text{mA}$. The bandwidth performance of this high-speed 850 nm VCSEL has been stated in [115] (Figure 2.15). The modulation bandwidth is increasing with the increased bias current and the maximum 3 dB bandwidth of 28 GHz can be achieved at bias current of 7.4 mA.

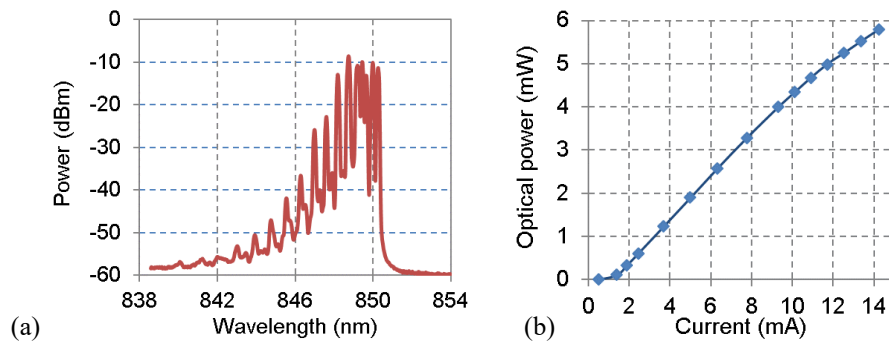


Figure 2.14: (a) Emitted spectrum at 12 mA bias and (b) optical power coupled in the 50 μm MMF

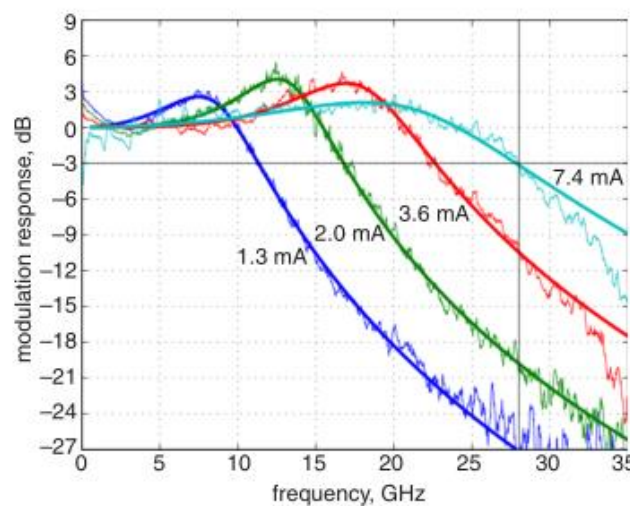


Figure 2.15: Measured small signal modulation response at increasing bias currents for the 850 nm

VCSEL [115]

2.4. Receivers

An optical receiver is used to convert the optical signal into the electrical domain. One of the key parameters is the receiver sensitivity which is defined as the minimum magnitude of the input signal required to produce an output signal within a specific bit error rate (BER) [79]. It depends on the detector responsivity, receiver bandwidth and noise performance. Photodetector is the main component of the receiver, which can be mainly categorized as APD and PIN detectors.

2.4.1. PIN photodetector

A simple PIN detector consists of a p-n junction with a layer of undoped semiconductor sandwiched between the p- and n- material, as shown in Figure 2.16. The intrinsic region offers a high resistance, and most of the voltage drops across it when the photodetector is reverse biased. If the energy of the incident photons is greater or equal to the bandgap energy of the photodetector, an electron is excited from the valence band to the conduction band. The electron flows from the p- side to the n- side, while the hole flows in the opposite direction and hence the photocurrent is generated.

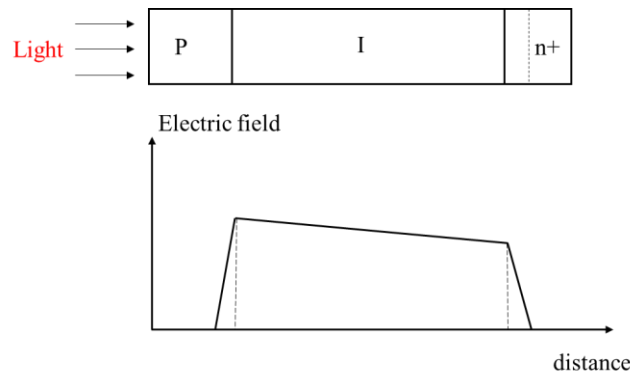


Figure 2.16: Schematic of the basic PIN detector structure with electric field distribution under reverse bias [79]

The photocurrent I_p is proportional to the input optical power P_{in} :

$$I_p = R \times P_{in} \quad 2-21$$

where R is the responsivity of the photodetector (A/W). The responsivity R depends on the quantum efficiency of the device. The wider the intrinsic layer, the higher the quantum efficiency. However, the bandwidth of the photodetector is reduced if the width of the intrinsic layer increases, as it takes longer for the generated carriers to drift across the depletion layer. Outside the intrinsic layer, electron-hole pairs are collected by electrodes through diffusion which is inherently a slower response than drift. A semiconductor material with a larger bandgap than the incident light energy can be used to solve this problem.

2.4.1.1 PIN noise performance

The receiver sensitivity highly relies on the PIN noise performance. Shot noise and thermal noise are the two fundamental noise mechanisms in the receiver.

- **Thermal noise**

Thermal noise is generated by the random thermal motion of electrons in a resistor which leads a random fluctuation in the current even in the absence of an applied voltage [79]. The thermal noise can be modelled as a Gaussian random process with up to 1 THz independent spectral density. It can be expressed as

$$\sigma_T^2 = \frac{4k_B T}{R_L} \Delta f \quad 2-22$$

where σ_T is the root mean square value of the noise current introduced by thermal noise; R_L is the load resistor and Δf is the effective noise bandwidth. In practice, many other electrical components including electrical amplifier and additional noise can also introduce noise. Therefore, the noise figure F_n is introduced to represent the factor by which thermal noise is enhanced by resistors used in pre- and main amplifiers. This can be expressed by

$$\sigma_T^2 = \frac{4k_B T}{R_L} F_n \Delta f \quad 2-23$$

- **Shot noise**

The shot noise is generated by a collection of random pulses corresponding to the electron-hole pairs

and the RMS value can be expressed as

$$\sigma_s^2 = 2qI_p\Delta f \quad 2-24$$

where I_p is the photo current and Δf is the effective noise bandwidth. The dark current also generates shot noise, and thus total shot noise can be given by

$$\sigma_s^2 = 2q(I_p + I_d)\Delta f \quad 2-25$$

- **Overall receiver noise**

For the PIN receiver, the overall noise is the summation of two noise currents due to the independence of the thermal noise and the shot noise, which is expressed as

$$\sigma^2 = \sigma_s^2 + \sigma_T^2 = 2q(I_p + I_d)\Delta f + \left(\frac{4k_B T}{R_L}\right)F_n\Delta f \quad 2-26$$

2.4.2. Avalanche photodetector

An APD is designed to be a semiconductor electronic device that has high sensitivity and can make use of the photoelectric effect to realize the conversion of light to electricity. In comparison with a PIN detector, an APD has higher responsivity owing to the photocurrent multiplication in the APD. The electron with sufficient energy can convey its kinetic energy to an electron within the valance band which generates a new electron-hole pair [79]. The whole phenomenon is called impact ionization and it can lead to the photocurrent multiplication in an APD.

APDs are used in situations when the optical power for the receiver is limited. Figure 2.17 shows the electric field strength at various parts of the APD under reverse bias. The multiplication region where the impact ionization happens is the major difference [79] compared to the PIN receiver.

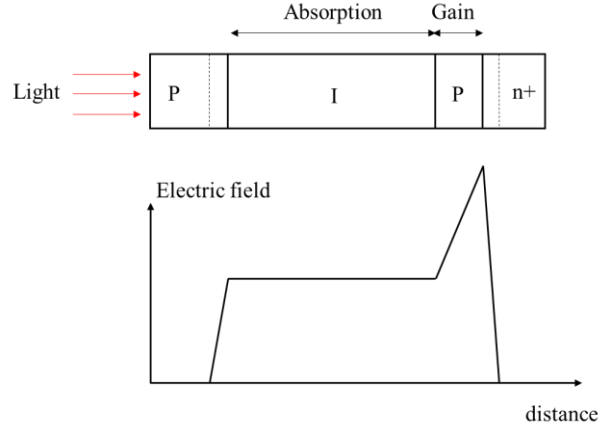


Figure 2.17: An APD together with the electric field distribution inside various layers under reverse bias [79]

According to Figure 2.17, the intrinsic layer is the absorption layer where a majority of the incident photons are absorbed and generate the primary carriers. Electrons that are generated in the intrinsic layer move to the n^+ layer owing to the electric field that is developed and the drift speed depends on the strength of the electric field. However, the carriers may collide with the lattice and the movement speed of the electrons would become saturated as the electrical field's strength increases. With the further increase of the reverse bias, the high electric field in the multiplication region will cause the generation of secondary electron-hole pairs through impact ionization. As a consequence, a single primary electron through the absorption of a single photon generates secondary electron-hole pairs, which then generates extra electron-hole pairs. This process will provide an internal current gain and the APD gain is also called the avalanche gain or multiplication factor (M). The phenomenon occurs under the condition that the strength of the electric field is about 2×10^5 V/cm in a typical material. the APD should be operated when the reverse bias voltage is high in order to achieve a good avalanche gain. Higher reverse bias voltage leads to higher avalanche gain. The electrical current that is generated by the APD for an input optical power of P_{in} is given as

$$I_{APD} = M \times R \times P_{in} \quad 2-27$$

where R refers to the APD's responsivity when there is no avalanche gain and M refers to the avalanche gain. The avalanche gain depends on the semiconductor materials used and the electric field that is applied [79].

2.4.1.2. PIN junction capacitance and bandwidth

PIN photodiodes can potentially provide a large bandwidth for glass fibre systems. However, for POF applications, they require a large active area to match the large POF core dimension. Therefore, the junction capacitance of such receivers is larger than the PIN diodes for glass fibre systems due to the large photodiode surfaces. This junction capacitance together with the input resistance of the circuit forms a low-pass filter limiting the entire bandwidth of the receiver. Figure 2.18 shows the bandwidth performance of the large area PIN detectors used for POF systems.

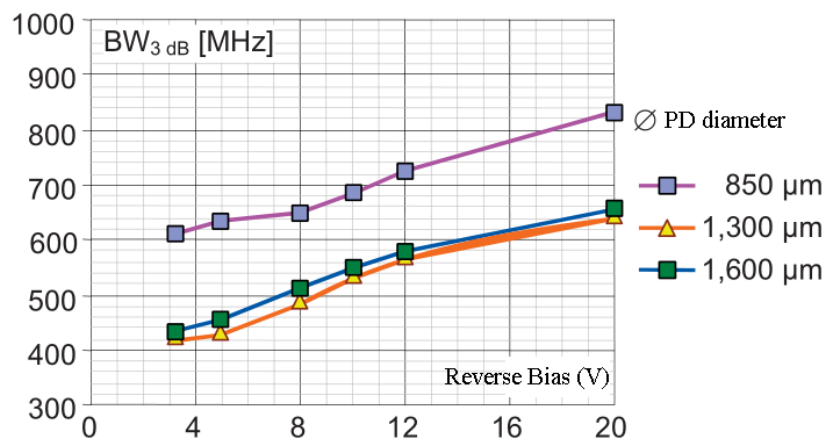


Figure 2.18: Measured receiver bandwidths for PIN detectors of various sizes and reverse bias voltage levels [23]

2.4.2.1. APD noise performance

Similar to PIN detectors, shot noise and thermal noise are also the two basic noise mechanisms in an APD receiver. The APD receiver's thermal noise is same as that in PIN detectors since the noise comes from the electrical circuit. However, the shot noise generation mechanisms are different for APD and PIN.

The APD multiplication process caused by impact ionization leads to the generation of secondary electron-hole pairs with statistical fluctuations. Every individual carrier's ionization is random, and the avalanche gain M shows the average multiplication level. As a result, the multiplication noise leads to an

extra shot noise, which results in a larger APD shot noise in comparison with that in a PIN detector. In addition, the dark current is enhanced through the avalanche multiplication process and an excess noise is generated. The total APD shot noise can be shown as follows

$$\sigma_s^2 = 2qM^2F_A(RP_{in} + I_d)\Delta f \quad 2-28$$

where F_A is the excess noise factor. The overall noise performance of the APD receiver is

$$\sigma_{APD}^2 = \sigma_s^2 + \sigma_T^2 = 2qM^2F_A(RP_{in} + I_d)\Delta f + \left(\frac{4k_B T}{R_L} F_n \Delta f\right) \quad 2-29$$

The thermal noise dominates the receiver noise as the APD's gain is low and the SNR improves with the avalanche gain. However, as the avalanche gain continues to increase, the shot noise will then dominate the noise and the increase of the noise is even larger than the increase of the signal amplitude, after which the SNR then reduces as the improved avalanche noise. Therefore, an optimal avalanche gain M_{opt} for the APD must exist providing a largest SNR to the received signal for a given input optical power.

2.5. Conclusion

In this chapter, the fundamentals building blocks of the VCSEL-MMF link and LED-POF link are reviewed, including VCSEL, LED, MMF, POF and both PIN/APD receivers.

For the VCSEL-MMF link, the basic structure of VCSLE is described and its advantages such as stable wavelengths, temperature insensitivity and high reliability are studied in details. The high bandwidth performance achieved by the 850 nm VCSEL makes it suitable for high speed short range data communications where MMFs have dominated owing to its low cost and high capacity compared to other media such as copper cables. The performance of MMF is mainly limited by modal dispersion. As 40 GbE and 100 GbE published, OM1 and OM2 fibre has not been considered in the IEEE802.3ba standard due to their low bandwidths. Therefore, OM3 and OM4 fibres with higher bandwidth are expected to replace OM1 and OM2 fibres in the future.

Various types of POF are available with different core index profiles. In this work, SI-POF with a core diameter of 1 mm is used for high-speed LED-POF links owing to its cost-effectiveness. Its large core diameter makes a much easier installation and optical coupling. However, a large number of excited modes results in multimode dispersion, which severely degrades the system performance.

In addition, both PIN/APD receivers are studied in this chapter. APD receivers demonstrate a higher responsivity than PIN detectors owing to the photocurrent multiplication mechanism.

CHAPTER

3

VCSEL BASED OM4 LINK USING CAP MODULATON SCHEME AND A NOVEL EQUALISER

A novel equaliser structure named the CAP equaliser is proposed for use in short-reach high-speed optical links. The proposed equaliser uses the data transmitted on both I- and Q- channels of the link in order to recover the transmitted symbol on each one of them to mitigate the impairment due to the non-linear phase response of the link. The significant performance improvement that this equaliser can achieve over a conventional DFE and FFE equaliser of the same length is demonstrated via simulation studies and data transmission tests on a short-reach VCSEL-based OM4 MMF links. The use of the CAP equaliser enables CAP-based 112 Gb/s data transmission over 100 and 150 m of OM4 MMF with a receiver sensitivity of -1.9 dBm and 0.5 dBm respectively for the HD-FEC BER threshold of 3.8×10^{-3} . The conventional FFE and DFE equaliser fails to support the same data rate over the same links while the use of the DMT modulation yields a poorer receiver sensitivity.

3.1. Introduction

In recent years, datacenter optical interconnects have attracted lots of attention owing to fast growing bandwidth demand from big Internet service providers, with Internet services evolving from e-mails and web-browsing to video streaming, social networking and cloud computing. The Internet services running in datacenters provides a massive number of servers which are connected and work together like a supercomputer, generating huge amount of Internet traffic both inside and outside of datacenters [116]. However, high-bandwidth cost and large power consumption rises challenges for an improved link capacity. With the network speed moving to 100G, the low bandwidth of MMF limits both distances and data transmission rate. Current research is now focused on improving the achievable data rates in short-range optical links. 400 Gb/s optical links are being targeted as the next generation of short-reach communication links inside data centres [117]. This target can be achieved with different configurations such as by deploying 16 lanes each operating at 25 Gb/s or 8 lanes at 50 Gb/s. However, such multi-lane configurations impose stringent requirements in terms of the power consumption, footprint and number of active and passive components in the link [112, 118]. A single-lane 100 Gb/s data link can provide some important advantages such as smaller footprint and lower power consumption, facilitating the implementation of next generation 400 Gb/s optical links.

The majority of short-reach optical links inside data centres consists of multimode fibre (MMF) links based on 850 nm multimode (MM) vertical cavity surface-emitting lasers (VCSELs). MM VCSELs are attractive components for use in such links as they exhibit relatively high output powers (> 1 mW) and large bandwidths (> 20 GHz) [119], are power efficient due to their low threshold current (~ 1 mA), are low cost, can be formed in large arrays and are readily interfaced with multimode ribbon fibres. Additionally, they are relatively insensitive to temperature effects, hence don't require temperature control and have a large enough output spectrum to minimize modal noise effects [120]. Record-high data rates of 70 Gb/s and 64 Gb/s have been achieved using non-return-to-zero (NRZ) modulation [121, 122]. Similarly, there has been increasing interest in recent years on single mode (SM) VCSELs operating at longer wavelengths (~ 1.31 μm and 1.55 μm) as they can enable low-cost optical links over SSMF and therefore achieve longer optical links (> 1 km) in data centre environments[123, 124].

However, achieving data rates ≥ 100 Gb/s over VCSEL-based MMF links using a single source is

challenging due to the limited bandwidth of the active devices and of the multimode fibre itself. Therefore, recent research has concentrated on spectrally-efficient, advanced modulation formats, such as pulse amplitude modulation (PAM) [125], carrier-less amplitude and phase (CAP) modulation [126] and discrete multitone (DMT) modulation [127]. Additionally, equalisation is typically used at the receiver (Rx) in high-speed links in order to mitigate the inter-symbol interference (ISI) caused by the limited bandwidth of the active components and fibre allowing successful recovery of the transmitted symbols. The equalisers typically employed comprise feed-forward (FFE) and decision feedback (DFE) equalisers [128].

Numerous high-speed VCSEL-based links achieving >100 Gb/s transmission over MMF have been reported in recent years by deploying multi-carrier and multi-level modulation schemes with equalisation. For example, a multiband-CAP modulation has been employed to achieve 100 Gb/s data rate over 10 m OM4 MMF [126]. 150 Gb/s and 112 Gb/s data transmission have been reported over 100 m of OM4 MMF fibre using duobinary PAM-4 [10] and DMT [129] respectively. In [12], pre-distortion and DMT modulation have been employed to demonstrate the transmission of 122 Gb/s over 10 m of OM4 MMF with a bit-error-rate (BER) within the soft-decision forward error correction (SD-FEC) threshold.

CAP modulation is a particularly interesting modulation scheme as it utilizes two orthogonal passband filters (in-phase and quadrature) to encode the baseband signal rather than employing sine and cosine carriers and is easier to implement than quadrature amplitude modulation (QAM) schemes [42] as it can be implemented with suitable hardware designs. Multi-carrier CAP schemes (M-CAP) have also been proposed and demonstrated in high-speed links [11]. However, single-carrier CAP has lower system complexity as smaller number of filters are employed compared to M-CAP. Furthermore, it offers important advantages over the equivalent PAM scheme, namely removing baseline wander whilst requiring similar bandwidth with very small additional implementation complexity. However, if the phase response of the link is non-linear, CAP modulation suffers from crosstalk between the in-phase (I-) and quadrature phase (Q-) channels. We propose a novel equaliser for use with CAP modulation, named the CAP equaliser. The new equaliser mitigates the effect of the non-linear phase response in the link, and therefore significantly improves the link performance over conventional FFE and DFE equalisers. In this chapter, the 112 Gb/s data transmission over 100 m and 150 m OM4 fibre demonstrated here includes 7% FEC overhead. Therefore, the net data transmission is 104 Gb/s.

3.2. Simulation model

3.2.1. VCSEL

We consider the simplest form of laser rate equations [130]. They are commonly called the lumped element rate equations which do not consider the variations of electron density or photon density within the laser cavity. The rate equations here have provided amount of equalisation that is required to improve transmitted or received waveform qualities and therefore it is sufficient to demonstrate equalizer principles and compare their performances.

$$\frac{dN}{dt} = \frac{I}{eV_a} - \frac{N}{\tau_{sp}} - g_0 \frac{(N - N_0)}{(1 + \varepsilon S)} S \quad 3-1$$

$$\frac{dS}{dt} = \Gamma g_0 \frac{(N - N_0)}{(1 + \varepsilon S)} S - \frac{\Gamma \beta N}{\tau_{sp}} - \frac{S}{\tau_{ph}} \quad 3-2$$

The lumped element rate equations describe the relationship between the average carrier density N , and the average photon density S . The other parameters of the equations are listed in Table 3-1.

Table 3-1: parameters used in the basic rate equations

Symbol	Quantity
I	drive current
e	electronic charge
β	spontaneous emission factor
Γ	optical overlap factor
V_a	effective volume of the active region
ε	gain saturation constant
τ_{sp}	spontaneous emission lifetime
τ_{ph}	lifetime of a photon in the cavity
g_0	gain constant
N_0	carrier density at transparency

Table 3-2 shows the rate equation parameters for various types of VCSELs, which has been stated in [130]. In this model, parameters for a 50 G PAM4 850 VCSEL is used as its high bandwidth and ability for multilevel encoding.

Table 3-2: Rate equation parameters for various types of VCSELs

Parameter	Type of Laser		
	10G NRZ 850 nm	25G NRZ 850 nm	50G PAM4 850 nm
	VCSEL	VCSEL	VCSEL
e	1.60E-19	1.60E-19	1.60E-19
Γ	0.165	0.18	0.1
β	0.001	0.001	0.001
V_a	7.630E-18	3.80E-18	3.80E-18
τ_{sp}	2.0E-09	4.0E-09	5.0E-09
τ_{ph}	1.0E-11	5E10-12	5.25E10-12
g_0	4.95E-12	1.2E-11	1.425E-11
ε	4.25E-23	4.125E-23	8.250E-23
N_0	1.07E+24	5.0E+24	5.0E+24

Figure 3.1 (a) shows the measured frequency response and modelling results at both 5 mA and 7.5 mA under different temperature conditions, indicating a good match between the experiment and simulation results. Measured eye diagram of Broadcom's 25Gbaud PM4 VCSEL over 1 m MMF is shown in Figure 3.1(b) with noise presented while Figure 3.1(c) shows a modelled eye (no noise) over 1m MMF overlaid with the measured eye.

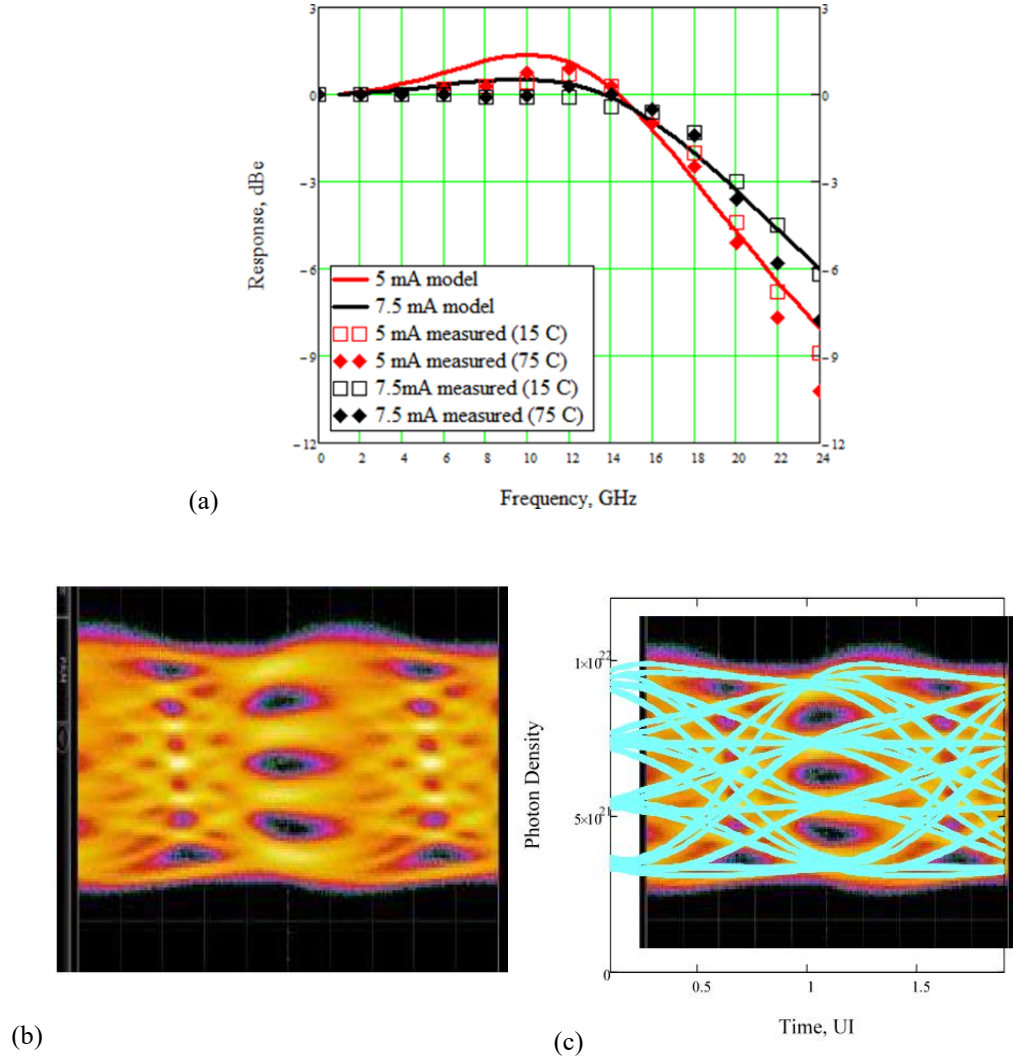


Figure 3.1: (a) Measured and modelled frequency response at 5 mA and 7.5 mA under different temperature conditions [130] (b) measured eye diagram of Broadcom's 25G PAM4 VCSEL and (c) modelled eye diagram overlapped with the measured eye diagram [130]

3.2.2. MMF (OM4) fibre

The light coupled into the OM4 fibre generates a large number of modes and causes modal dispersion. For a multimode OM4 fibre, it was found in [131] that the frequency response can be well modelled using a Gaussian filter. In the simulation, 100 OM4 fibre is the transmission channel, which has ~ 24 GHz bandwidth. The impulse response is given by

$$h(t) = \frac{1}{\sigma\sqrt{2\pi}} e^{\frac{-t^2}{2\sigma^2}} \quad 3-3$$

where the standard deviation σ can expressed as

$$\sigma = \frac{\sqrt{0.6 \times \ln(10)}}{2\pi f_c} = \frac{0.1871}{f_c} \quad 3-4$$

where f_c is the -3 dB bandwidth of the SI-POF.

If the Fourier transform is taken then the normalized frequency response can be written as

$$H(f) = e^{\frac{-4\pi^2 f^2 \sigma^2}{2}} \quad 3-5$$

The frequency response of the Gaussian OM4 model is shown in Figure 3.2.

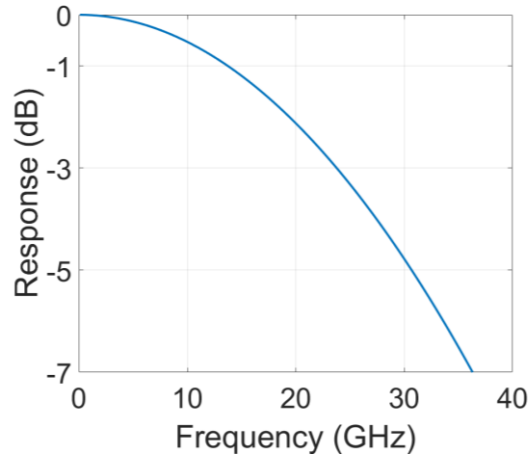


Figure 3.2: Frequency Response of the Gaussian OM4 fibre model.

3.2.3. PIN receiver

The receiver in a fibre link can be also be modelled using a raised cosine response[131], which has the normalized impulse response expressed as

$$h(t) = \frac{\sin(5.5\pi f_r)}{2\pi(1 - (5.5\pi f_r)^2)} \quad 3-6$$

where f_r is the -3 dB bandwidth of the receiver. The frequency response can be expressed as

$$H(f) = \cos\left(\frac{2\pi f}{11f_r}\right)^2$$

3-7

The bandwidth for the PIN receiver (D30-850M) used in this work is 30 GHz which is stated in the manual [23]. Therefore, a raised cosine filter with a bandwidth of 30 GHz is used in the system modelling.

Figure 3.3 shows the frequency response.

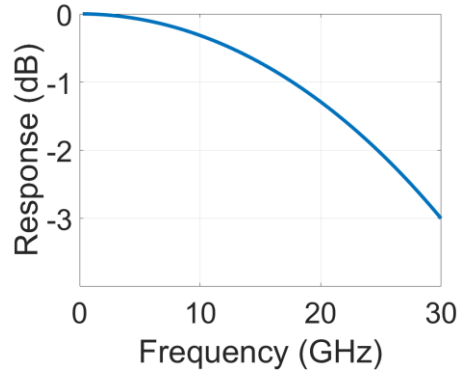


Figure 3.3: Frequency response of the PIN receiver model with 30 GHz bandwidth

3.2.4. Noise Model

The noise model is based on the experimental measurement. The root-mean-square (RMS) value of total noises in the link is measured at various levels of average received optical power without input RF signals using the histogram function of an oscilloscope, as illustrated in Figure 3.4. Figure 3.5 illustrates the measured noise performance against different received optical power. It is clearly seen that RMS value of the noise slightly increases with the increased received optical power.

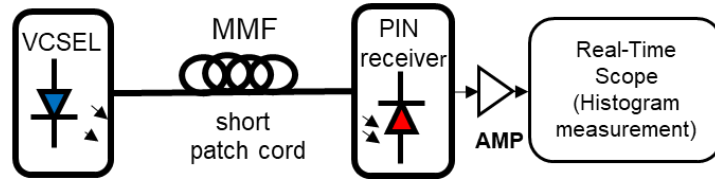


Figure 3.4: Experimental setup for receiver noise measurement

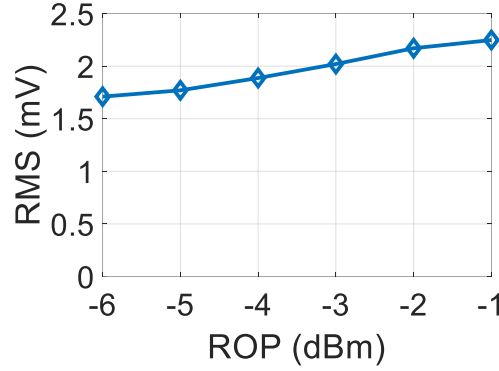


Figure 3.5: Measured RMS value of the total noise at various received optical power (ROP: receive optical power)

3.2.5. Equalisation

In this work, a feed-forward equalisation combined with decision-feedback equaliser is employed in the link. A pulse will spread out when passing through a dispersive channel, and ISI can be generated as the pulses spread out beyond their symbol periods and interfere with adjacent pulses, causing errors in the decision device at the receiver output. Therefore, a filter that is able to compensate for the distortion is required to reshape the signal back to its original one. This filter can be realized by the equalisation technique.

Equalisation has been widely used in copper cable, radio frequency (RF) and optical links [132, 133] in order to mitigate the ISI induced by the link's bandwidth limitation[134, 135]. The most commonly used equalisers are FFE and DFE which are more effective in suppressing large amount of ISI than less complex linear equalisers [128]. They have been proven to provide significant performance improvements and extend the transmission capability.

In a dispersive optical channel, ISI come from both ends of the symbols. Figure 3.6 illustrates the interferences between symbols in a continuous time transmission.

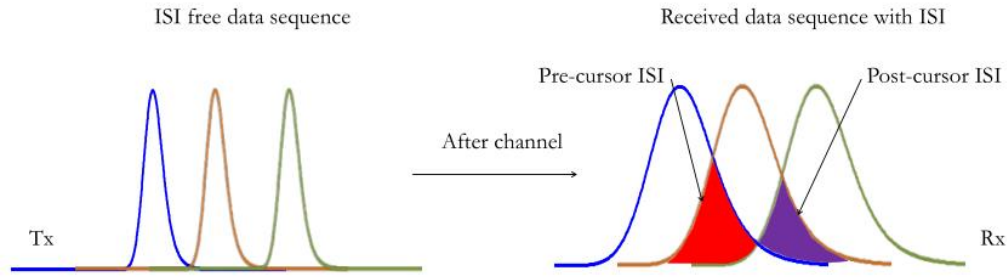


Figure 3.6: Pre-cursor ISI and post-cursor ISI of a symbol after dispersive channel

The ISI coming from the later time which is on the left is called pre-cursor ISI and from earlier time (the right side) is called post-cursor ISI. The decision feedback equaliser (DFE) gather the information from the decision of previous symbols. Therefore, the post-cursor from the earlier symbol can easily be suppressed by the DFE. The feed forward equaliser (FFE) relies on the information from the current and later symbols. Therefore, the pre-cursor can be suppressed by FFE. FFE is using a finite impulse response (FIR) and DFE is using an infinite impulse response (IIR) filter. Later in this section the structure of FFE and DFE will be introduced separately.

The feed forward equaliser effectively amplifies the high frequency components of the channel in order to compensate the channel dispersion. Therefore, it always brings noise enhancement to the system. However, the decision feedback equaliser utilizes the decisions from the previous symbols which will not introduce the noise enhancement penalty although it may cause the error propagation due to the feedback structure. Combined with DFE, the total number of tap lengths can be reduced in comparison with the linear FFE for the same amount of ISI mitigation [136]. The least mean square (LMS) algorithm is used for the equaliser training process in order to find optimum coefficients.

3.2.5.1 Feed forward equaliser (FFE)

The structure of an FFE is in the same structure as an FIR filter. As illustrated in Figure 3.7, the input signal is sampled at half symbol rate ($T/2$) and the delayed samples are then multiplied by the corresponding tap values which have been pre-adapted to give preferable equaliser structure. The output is expected to remove pre-cursor ISI and recovers symbols. During the feed-forward equalisation process, the noise is also amplified, resulting in an enhanced noise level.

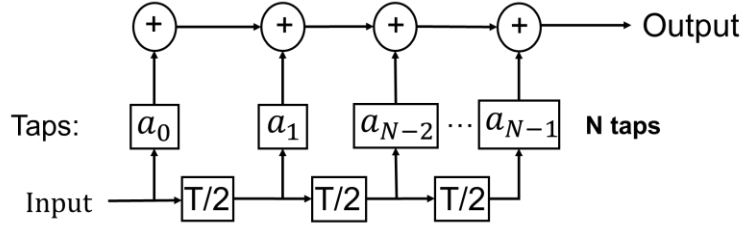


Figure 3.7: Pre-cursor ISI and post-cursor ISI of a symbol after dispersive channel

3.2.5.2. Decision feedback equaliser (DFE)

As shown in Figure 3.8, A DFE is a nonlinear equaliser which can cancel ISI while minimizing any noise enhancement. The DFE can be implemented as an IIR filter, and it utilizes the decisions from the previous symbol to recover the signal, which therefore only eliminates post-cursor ISI. The output is through the multiplication of previous decision with individual tap values.

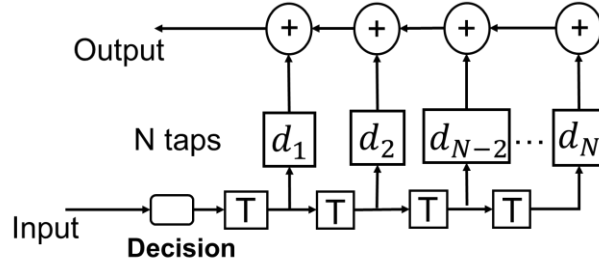


Figure 3.8: Schematic of a Decision feedback equaliser

3.2.5.3. FFE and DFE

The combination of FFE and DFE can eliminate both pre- and post- cursor ISI. The structure of FFE and DFE is illustrated in Figure 3.9. The operation of an FFE and DFE based equaliser, for the case where the FFE operates on two samples per symbol, is described by the equation

$$r_k = \sum_{n=0}^{N-1} a_n s_{2k+N-1-n} + \sum_{m=1}^M d_m \hat{r}_{k-m} \quad 3-8$$

where r_k is the symbol after application of the equaliser (i.e. the recovered symbol) and \hat{r}_{k-m} is the

decision on the k -th received symbol, N and M are the FFE and DFE tap lengths, a_n and d_m are the FFE and DFE tap coefficients respectively and $S_{2k+N-1-n}$ is the received sample for given k, n and N .

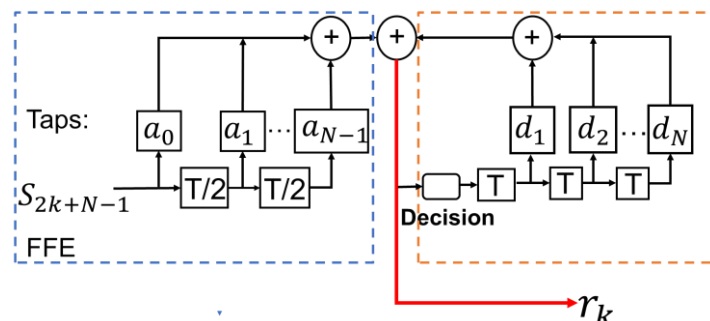


Figure 3.9: detailed structure of the conventional FFE and DFE

3.2.5.4. Noise enhancement factor

DFE employs information from the previous decision, which does not affect the noise as no actual received value is used while the FFE utilizes the received waveforms including the noise value and amplifies the high frequency component of the noise in order to recover the signals. Assuming white noises, the noise enhancement factor α is defined to indicate the times of the noise being amplified, which can be written by

$$\alpha = \sqrt{\sum_{k=1}^n a_k^2} \quad 3-8$$

where a_k is the k^{th} tap coefficients of FFE. The root-mean-square (RMS) of the noise after FFE and DFE is then calculated as

$$\sigma_{\text{new}} = \alpha \times \sigma_{\text{received}} \quad 3-9$$

where σ_{received} is the RMS value of the noise before the FFE and DFE.

3.2.6. Error vector magnitude (EVM)

Various imperfections such as noise and dispersion result in the movement of constellation points from ideal locations. As a result, EVM is introduced to describe the effective distance of the received symbols

from the ideal position in the constellation diagram. It measures and quantifies the quality of the received signals. Mathematically, EVM is defined by a root mean square of errors σ_{err} , for a series of randomly M transmitted data and includes all the impairments, which can be illustrated in Equation 3-10 and 3-11.

$$E_{err,i} = E_{r,i} - E_{t,i} \quad 3-10$$

$$\sigma_{err}^2 = \frac{1}{M} \sum_{i=1}^I |E_{err,i}|^2 \quad 3-11$$

For different modulation formats, EVM can be normalized by the power of the longest ideal constellation vector $E_{t,m}$

$$EVM_m(\%) = \frac{\sigma_{err}}{\sqrt{E_{t,m}}} \times 100\% \quad 3-12$$

In this work, EVM is used to evaluate the equaliser performance. The imperfections in the simulation and experiment is mainly caused by residual inter-symbol-interference (ISI).

3.2.7. Forward Error Correction

Forward error-correction coding (FEC) is a type of digital signal processing technique in order to improve data reliability by introducing a known structure into a data sequence prior to transmission or storage. In fibre-optic communication systems, the standard FEC scheme is based on RS codes: (255, 239) in G.975 standard [137]. Although novel FEC schemes such as iteratively decodable codes, turbo [138], and low-density parity-check (LDPC) [139] has been developed for optical transmission systems, the widely applied RS codes are used in this thesis for the error correction. The purpose of this work concentrates on advanced equalisation technique so that different FEC codes performances are not compared here. Furthermore, This standard FEC scheme is operated at 7% overhead hard decision with the bit error rate (BER) limit of 3.8×10^{-3} referring to the hard decision FEC (HD-FEC), which can be found in [140].

3.3. Simulation Results

The main parameters of components are listed in Table3-3. The values of the parameters are chosen to match the parameters of the devices used in the experimental data transmission tests. The dynamic

behaviour of the VCSEL is modelled with a rate equation model which provides the output light waveform for a given modulating signal and bias condition. Its parameters are based on published data on commercially-available directly modulated VCSELs. The fibre and receiver are modelled with a Gaussian and a raised-cosine response, respectively.

Table 3-3: Link simulation parameters

Component	Response type	-3 dB _o / -6 dB _e bandwidth
VCSEL	Rate equation based	25 GHz
100 m OM4 MMF	Gaussian	24 GHz
Receiver	Raised-cosine	30 GHz

3.3.1. CAP-16 based link performance

As discussed in Chapter 1, CAP modulation uses two passband filters to encode the signal at the transmitter side and demodulated at the receiver side. Generally, the high-speed CAP based transmission system is shown in Figure 3.10 including the generation and demodulation of CAP signals. FFE and DFE is employed to recover the distorted signals at the receiver side after demodulation process.

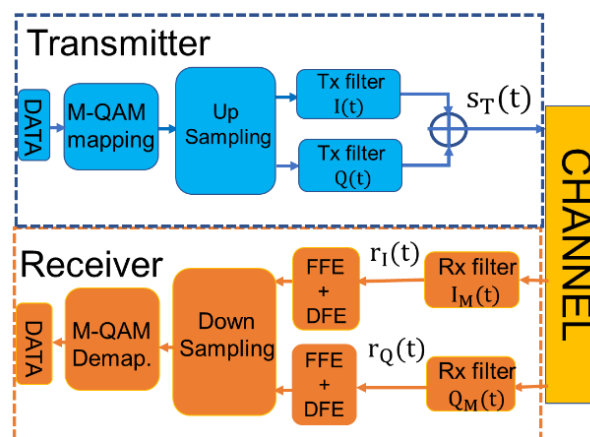


Figure 3.10: Typical CAP-based transmission

Figure 3.11 illustrates the block diagram of simulation model. The normalized composite CAP signal in conjunction with DC bias drives the VCSEL model and convolved with the impulse response of MMF, receiver, respectively. The received signal is then demodulated by two matched filters and then employs FFE and DFE to suppress ISI. The BER is calculated considering the measured noise RMS value and noise enhancement factor introduced by the equaliser.

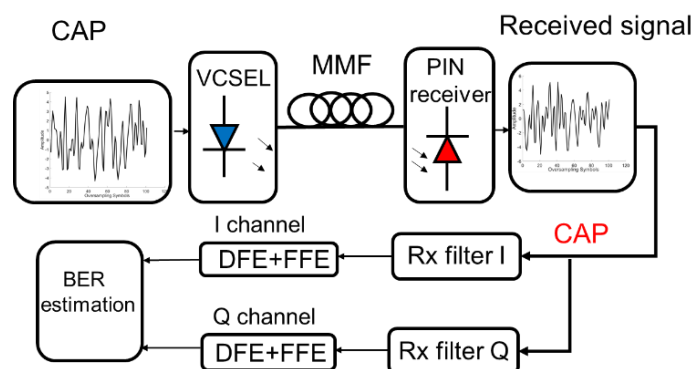


Figure 3.11: Block diagram of link model used for CAP

3.3.1.1. Demodulation

Figure 3.12(a) illustrates the eye diagram of I- channel based on CAP-16 modulation scheme. This is the ideal situation which does not introduce any link impairments. The demodulation map is shown in Figure 3.12(b). In order to investigate the channel dispersion, constellation diagram before equalisation at various symbol rates over 100 m OM4 fibre are investigated in Figure 3.13: (a) 5 Gbaud, (b) 15 Gbaud, and (c) 25 Gbaud. It can be clearly seen that symbols are recovered in the case of (a) and (b), whereas symbols fail to be recovered in the case (c).

Therefore, equalisation technique is employed to recover the signals at high data rate. As introduced in the section 3.2, FFE and DFE is employed in the link to effectively suppress ISI. Specifically, for the CAP modulation, besides the ISI introduced by the limited bandwidth, the nonlinear phase response of the link also significantly degrades the system performance by introducing crosstalk between I- and Q- channel. However, the conventional equaliser cannot solve this crosstalk issue introduced by the link which will be further discussed in the following section.

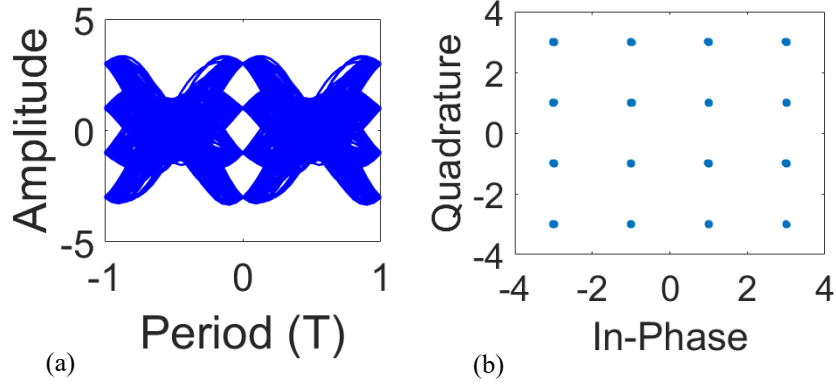


Figure 3.12: Ideal (a) I- channel eye diagram and (b) constellation diagram

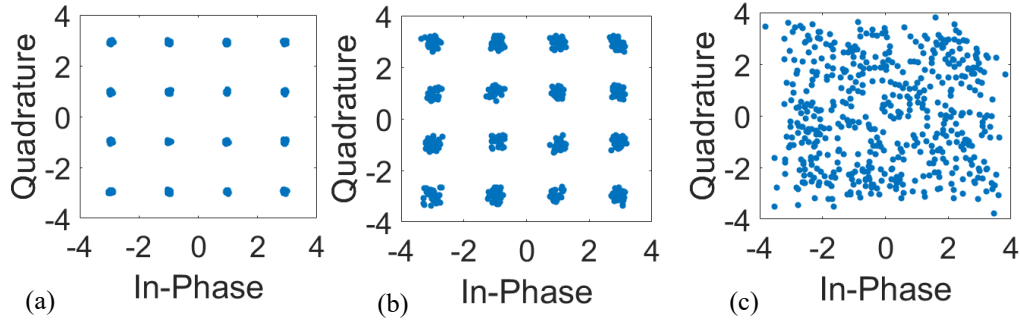


Figure 3.13: Demodulation results over 100 m OM4 fibre at various symbol rate: (a) 5 Gbaud(20 Gb/s), (b) 15 Gbaud (45 Gb/s) and (c) 25 Gbaud (100 Gb/s)

3.3.1.2. Nonlinear phase response

The input data is divided into two parallel data streams (QAM-mapping), which are then up-sampled and encoded by the in-phase (I-) and quadrature (Q-) channel pulse shaping filters. The two channels are combined, and the resulting composite signal modulates the optical transmitter. For example, CAP-16 is generated by the addition of two PAM-4 streams encoded with the I- and Q- channel filters, respectively. The impulse response of the I- and Q- channel filters is formed by the product of a square root raised cosine (SRRC) filter and a cosine (I-channel) or sine (Q-channel) function. The mathematical expression that describes the transmitted CAP signal $s_T(t)$ is given in **3-13**.

$$s_T(t) = D_I(t) \otimes I(t) + D_Q(t) \otimes Q(t) \quad \text{3-13}$$

where $I(t)$ and $Q(t)$ are the pre-defined pulse shaping functions of the I- and Q-channel transmit (Tx) filters and “ \otimes ” is the convolution operator. $D_I(t)$ and $D_Q(t)$ represent the I- and Q-channel symbol streams. At the receiver end (Rx), the time domain demodulated signal $r_I(t)$ and $r_Q(t)$ can be expressed as **3-14** and **3-15**.

$$r_I(t) = s_R(t) \otimes I_M(t) \quad \text{3-14}$$

$$r_Q(t) = s_R(t) \otimes Q_M(t) \quad \text{3-15}$$

The condition for separating the I- and Q- channel symbols at the receiver side (Rx) is stated in **3-16** and **3-17**.

$$\angle I_M(\omega) \equiv \angle Q(\omega) + \frac{\pi}{2} \quad \text{3-16}$$

$$\angle Q_M(\omega) \equiv \angle I(\omega) + \frac{\pi}{2} \quad \text{3-17}$$

where $\angle I(\omega)$ and $\angle Q(\omega)$ are the phase spectrum of I- and Q- Tx filters, $\angle I_M(\omega)$ and $\angle Q_M(\omega)$ are the phase spectrum of I- and Q- Rx matched filters. The phase difference of $\frac{\pi}{2}$ which appears in **3-16** and **3-17** indicates the orthogonality of I- and Q-channels, and guarantees the independent demodulation of the I- and Q- channels without any crosstalk. Assuming that the optical link has an impulse response $h(t)$, the received signal $s_R(t)$ is given by the expression **3-18**.

$$s_R(t) = s_T(t) \otimes h(t) \quad \text{3-18}$$

Combining **3-13** with **3-18**, the $s_R(t)$ can be expressed as

$$s_R(t) = D_I(t) \otimes \hat{I}(t) + D_Q(t) \otimes \hat{Q}(t) \quad \text{3-19}$$

where $\hat{I}(t) = I(t) \otimes h(t)$ and $\hat{Q}(t) = Q(t) \otimes h(t)$. The functions $\hat{I}(t)$ and $\hat{Q}(t)$ describe the combined response of the transmit I- and Q-filters and the optical link. If the link has linear phase response $\angle H(\omega) = k\omega$, the phase spectrum of the combined response of the transmit filters and optical link $\angle \hat{I}(\omega)$ and $\angle \hat{Q}(\omega)$ become $\angle I(\omega) + k\omega$ and $\angle Q(\omega) + k\omega$ respectively. This additional linear phase response can be mitigated by time-shifting the received signal by k : the time-domain received signal is $s_R(t - k)$ and its phase spectrum becomes $\angle S_R(\omega) - k\omega$. As a result, the phase spectrum can

be corrected by $(-\omega k)$, which will shift back $\angle \hat{I}(\omega)$ and $\angle \hat{Q}(\omega)$ to $\angle I(\omega)$ and $\angle Q(\omega)$. Therefore, a linear link phase response does not introduce any signal transmission impairment.

However, if the link has a non-linear phase response $\sigma(\omega)$, the phase spectrum of the combined response of the transmit filter and optical link becomes

$$\angle \hat{I}(\omega) \equiv \angle I(\omega) + \angle \sigma(\omega) \quad 3-20$$

$$\angle \hat{Q}(\omega) \equiv \angle Q(\omega) + \angle \sigma(\omega) \quad 3-21$$

Now, in order to maintain the signal orthogonality and be able to separate the two channels perfectly at the receiver, the following equations for the phase response of the matched filters $\angle I_M(\omega)$ and $\angle Q_M(\omega)$ need to be satisfied

$$\angle I_M(\omega) \equiv \angle Q(\omega) + \angle \sigma(\omega) + \frac{\pi}{2} \quad 3-22$$

$$\angle Q_M(\omega) \equiv \angle I(\omega) + \angle \sigma(\omega) + \frac{\pi}{2} \quad 3-23$$

However, the matched filter $I_M(t)$ and $Q_M(t)$ are pre-defined, and can only satisfy **3-16** and **3-17**. Due to the nonlinear phase response term $\angle \sigma(\omega)$, equations **3-22** and **3-23** cannot be satisfied. As a result, crosstalk between the two channels is generated. For channels suffering linear distortion it is common to use a combination of FFE and DFE equalisers to recover the transmitted symbols, as shown in Figure 3.14. However, these conventional equalisers cannot correct non-linear distortion and so cannot combat the crosstalk due to the non-linearity of the channel. Therefore, a novel equaliser, here named the CAP equaliser, is introduced to solve this issue.

3.3.1.3. CAP equaliser structure

. In the context of CAP-based transmission, such an FFE and DFE (conventional) equaliser is applied separately on each channel to recover the transmitted data [Figure 3.14(a)]. However, such equaliser cannot mitigate the channel crosstalk described above due to the non-linear phase response of the link. The proposed new (CAP) equaliser structure utilises the signals received on both channels to mitigate the Q- channel crosstalk and recover the I- transmitted symbols is shown in Figure 3.14(b). The detailed structure of this novel equaliser is shown in Figure 3.15.

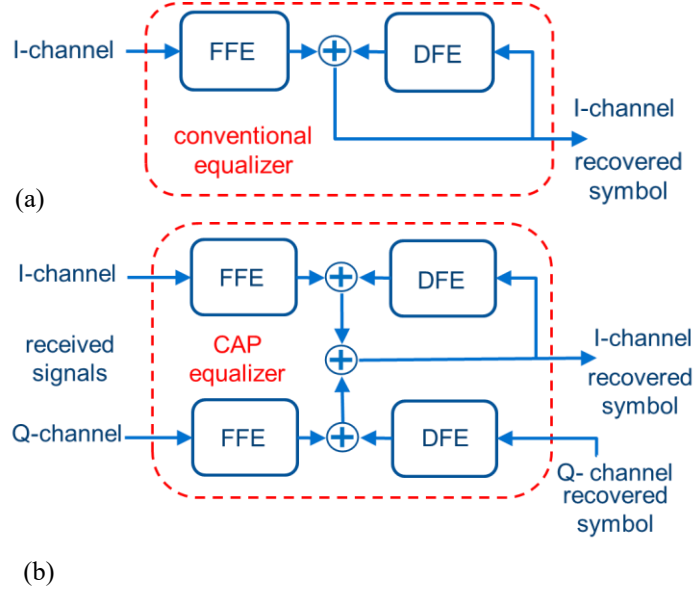


Figure 3.14: Structure of (a) a conventional FFE and DFE equaliser and (b) the proposed CAP equaliser for I- channel recovery. Similar structure can be applied for Q- channel

For CAP-based transmission, a separate FFE and DFE equaliser is employed on each channel to recover the transmitted symbols. However, as indicated above, the non-linear phase response of the link generates channel crosstalk which prohibits the perfect separation of the two channels at the receiver. This issue cannot be solved by this conventional equaliser as explained in section 3.3.2.2. As a result, we propose a new FFE and DFE equaliser for CAP-based transmission that aims to mitigate this issue. The detailed structure of this novel equaliser with delay lines for I- channel and Q- channel is shown in Figure 3.15(a) and (b), respectively. They have same structure but with different tap coefficients and comprises an FFE and DFE part similar to the conventional, but utilizes the symbols received on both channels to recover the symbols transmitted on each one of them. Equation 3-24 provides the expression used to recover the transmitted symbols on the I-channel for this new CAP equaliser:

$$r_k^I = \sum_{n=0}^{N-1} a_n^I S_{2k+N-1-n}^I + \sum_{m=1}^V d_m^I \hat{r}_{k-m}^I + \sum_{p=0}^{P-1} a_p^Q S_{2k+P-1-p}^Q + \sum_{l=1}^L d_l^Q \hat{r}_{k-l}^Q \quad 3-24$$

where r_k^I is the recovered I-channel k -th symbol, \hat{r}_{k-m}^I and \hat{r}_{k-l}^Q are the previous $k-m$ and $k-l$ symbol decisions on I- and Q- channel respectively, a_n^I and d_m^I are the I-channel FFE and DFE tap coefficients,

a_p^Q and d_l^Q are the Q-channel FFE and DFE tap coefficients. A similar expression is used to recover the transmitted symbols on the Q-channel but with different coefficient values. It is shown in the simulation studies described below that only a small number of additional taps operating on the other channel are required to achieve significant performance improvement. As a result, the implementation of the proposed CAP equaliser requires small additional complexity in the system implementation.

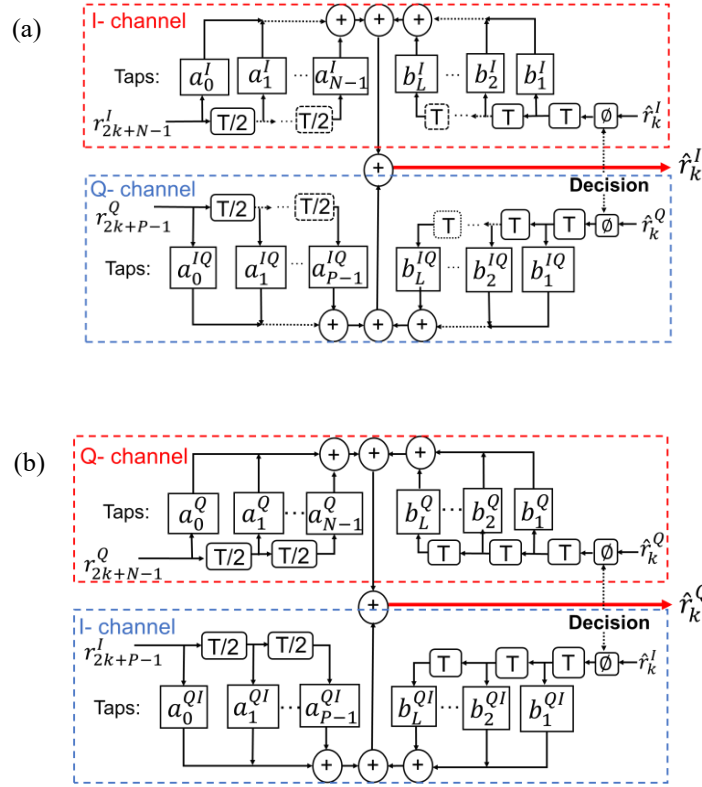


Figure 3.15: The CAP equaliser (CAP-EQ) applied on I- channel (a) and Q- channel (b).

3.3.2. Link performance

3.3.2.1. Simulated results

The performance of various links is studied with a link model to simulate the performance of a VCSEL-based OM4 MMF link. At the receiver end, equalisation is employed to mitigate the ISI of the link. The magnitude and phase of the link's frequency response was calculated for a 100 m long MMF OM4 (Figure 3.16). The phase of the signal at the transmitter side (transmitted signal) and at the receiver side (received signal) are obtained by the Fast Fourier Transforms, respectively. The nonlinear phase

response of the link is calculated by subtracting the phase of transmitted signal from the phase of the received signal. The nonlinear phase response is accumulated from the dynamic model of the VCSEL, the OM4 fibre and also the PIN receiver. The real-value FIR filter can result to a nonlinear phase response when its coefficients are designed to be non-symmetric.

The nonlinear phase response of the link can be clearly seen for Figure 3.16. The performance of the link was calculated when 112 Gb/s CAP-16 modulation (encoded PAM-4 for I-/Q- channel) was applied and when the proposed new CAP and a conventional FFE-DFE equaliser with the same length and tap spacing were used. The tap spacing for the FFE section of both types of equaliser was half of a symbol period ($T/2$).

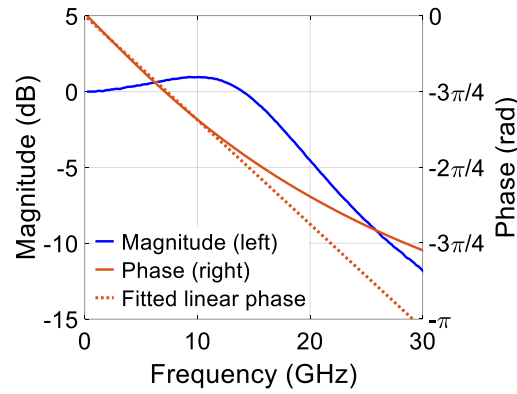


Figure 3.16: Simulated magnitude and phase of the frequency response for the VCSEL-based 100 m OM4 MMF link.

For CAP-based transmission, the data pattern used to train the equaliser consisted of a $2^{11}-1$ pseudo-random binary sequence (PRBS) which was encoded with a random order into CAP-16 symbols. The training pattern was used to obtain the weight of the equaliser taps using the least mean squares (LMS) algorithm. The data pattern used in the data transmission tests consisted of the same PRBS encoded in the normal order to form the transmitted CAP-16 symbols.

Initially, a representative simulation is performed to demonstrate the channel crosstalk impairment due to the non-linear phase response of the link. A short symbol stream ($2^{11}-1$ PRBS) is transmitted over the I-channel of the link at both (i) low (9 GBaud, 36 Gb/s) and (ii) high (28 GBaud, 112 Gb/s) symbol rates

when the Q-channel is off (no data) and on (transmitting data). For the case of low speed transmission, the spectrum of the transmitted signal mainly falls within the linear range of the phase response of the link (< 10 GHz, Figure 3.16) and therefore the orthogonality of the I- and Q-channels is well maintained over the link. As a result, the operation of the Q-channel should not affect the received signal on the I-channel. On the contrary, at the high symbol rate of 28 GBaud, the phase response is non-linear within the signal bandwidth and therefore, the operation of the Q-channel introduces crosstalk distorting the received signal. Figure 3.17 shows the demodulated I-channel symbols for the two modes of operation (Q-channel on/off) and two symbol rates before equalisation. It can be clearly seen that the operation of the Q-channel only distorts the received signal on the I-channel at the high symbol rate, indicating the presence of the channel crosstalk due to the non-linear phase response. Similar crosstalk issues also exist for the Q-channel.

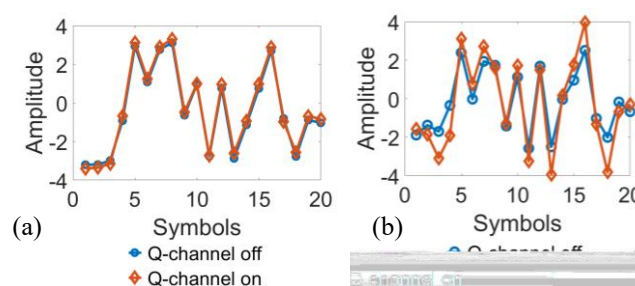


Figure 3.17: Demodulated I- channel symbols for the two modes of operation before equalisation at two different symbol rates: (a) 9 GBaud(36 Gb/s); (b) 28 GBaud (112 Gb/s).

Additionally, the two types of equalisers (conventional and CAP) are employed to recover the transmitted symbols on the I-channel for the high symbol rate transmission (112 Gb/s) when the Q-channel is transmitting data. Figure 3.18 shows the obtained error for the equaliser training for the two equalisers. The signal recovery is only successful when the root-mean-square (RMS) errors can finally converge to an acceptable value (RMS error <1). It can be clearly seen that the training interacted RMS errors of the conventional equaliser converge to ~ 1.6 while the proposed CAP equaliser converges that to ~ 0.4 . Therefore, the conventional equaliser fails for the signal recovery. In contrast, the CAP equaliser is able to recover that and is able to support this link.

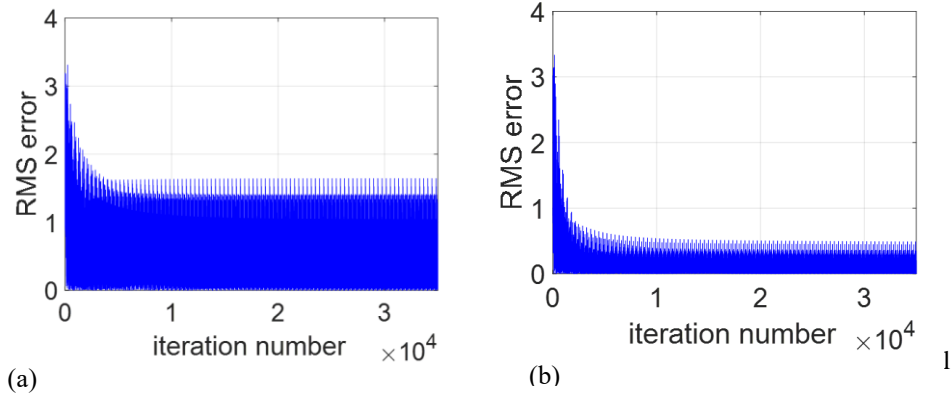


Figure 3.18: Obtained RMS errors for the LMS training algorithm at 112 Gb/s over 100 m OM4 fibre:

(a) conventional and (b) the CAP equaliser. (RMS: root mean square)

Figure 3.19 shows the demodulation results obtained with the simulation model for 112 Gb/s CAP-based data transmission over a 100 m OM4 MMF link in the cases where the conventional and CAP equalisers were employed at the receiver: (a) and (c) constellation diagrams, and (b) and (d) eye diagrams for the I-channel after equalisation. The conventional equaliser used 25 FFE taps and 25 DFE taps while the CAP equaliser used the same total tap length (20+20 from the I- (main) channel and 5+5 from the Q- (crosstalk) channel). The noise of the received signal has not been included in the diagrams to allow better visualization of the residual ISI in the link and direct comparison of the performance achieved with the two equalisers. Clearly the proposed CAP equaliser yields good constellation and eye diagrams, whereas the conventional equaliser fails to recover the transmitted signal. The CAP equaliser clearly outperforms the conventional equaliser.

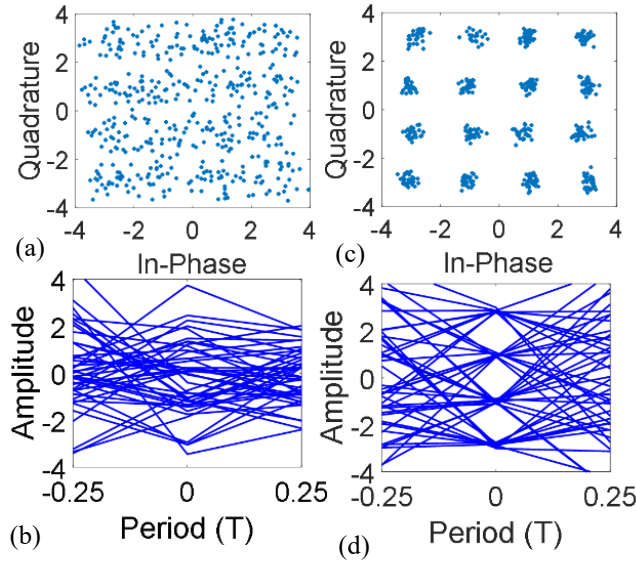


Figure 3.19: Simulation results (constellation diagrams and eye diagram for the I-channel after equalisation) for CAP-based 112 Gb/s data transmission over 100 m of OM4 MMF when (a-b) the conventional equaliser and (c-d) the proposed CAP equaliser is employed

Figure 3.20 shows the error vector magnitude with the increased number of conventional equaliser taps in order to deduce an appropriate tap numbers for the FFE and DFE. The tap number is equally split between the FFE and DFE (i.e. 20-taps correspond to a 10-tap DFE and 10-tap FFE) for both I- and Q-channels. It has been clearly shown that the EVM saturates at ~16% with 40 total number of taps and further increase of tap number will not take much effects. Therefore, the reference performance for the comparison of CAP equaliser and conventional equaliser starts from 20 FFE taps and 20 DFE taps on both I- and Q- channels.

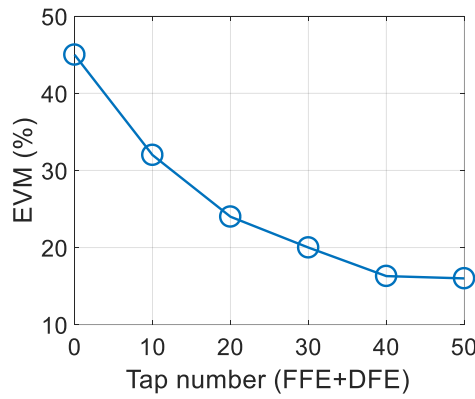


Figure 3. 20: Calculated EVM as a function of the number of taps for the conventional equaliser for 112 Gb/s data transmission over 100 m OM4 MMF.

In order to assess the additional complexity required for successful signal recovery at this data rate, the error vector magnitude (EVM) was calculated as function of the number of additional taps introduced for each type of equaliser (Figure 3.21). The reference performance obtained for 0 additional taps corresponds to a 20-tap FFE and 20-tap DFE conventional equaliser on the I- and Q-channel. The additional taps are equally split between the FFE and DFE (i.e. 2 additional taps correspond to a 21-tap DFE and 21-tap FFE). For the conventional equaliser the additional taps are introduced only in the FFE and DFE of the same channel, while for the CAP equaliser the additional taps are introduced in the FFE and DFE of the other channel. Figure 3.21 shows that the conventional equaliser can only achieve an EVM of ~16% and that increasing the number of taps does not provide any significant performance improvements in the link. This is due to the fact that no further suppression of the ISI can be achieved with this type of equaliser. On the contrary, the introduction of equaliser taps on the other channel in the proposed CAP equaliser, results in a significant reduction of the EVM, with ~4% achieved for only 10 additional taps (5 additional DFE and 5 additional FFE taps) from the other channel. The performance improvement for this equaliser also saturates beyond 10 additional taps as the effectiveness of the equaliser cannot be further improved.

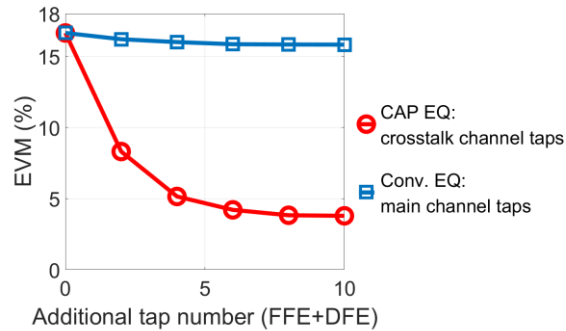


Figure 3.21: Calculated EVM as a function of the additional number of taps for both types of equaliser for 112 Gb/s data transmission over 100 m OM4 MMF (Conv: conventional, EQ: equaliser).

At a data rate of 112 Gb/s, the performance of the same link was also simulated when DMT modulation, with adaptive power and bit loading, PAM-4 and PAM-16 modulation were used. This was to allow comparison with the performance obtained with conventional CAP-based transmission and the newly proposed CAP equaliser. A PRBS pattern of the same length as the one used for the CAP-based

transmission is employed to encode the transmitted symbols on each subcarrier. The DMT signal generation contains serial to parallel conversion, adaptive power and bit loading, Hermitian-symmetry operation, inverse fast Fourier transformation (IFFT, length 512), cyclic prefix insertion (15 samples), parallel-serial conversion and clipping (ratio: 5 dB) [127]. The bit and power loading scheme used is shown in Figure 3.23(a) and it is based on the estimation of the signal-to-noise ratio (SNR) of the received signal for training sequences consisting of only QAM-4 modulation subcarriers. The power of each subcarrier shown in Figure 3.23(a) is calculated as the ratio of its power to the power of the first subcarrier and expressed in dB. At the receiver end, a single-tap equaliser was employed for the DMT transmission to recover the transmitted symbols, while for PAM-based transmission a conventional FFE and DFE equaliser with the same length and tap spacing as the CAP equaliser was employed. Figure 3.22 shows the recovered eye diagram of PAM-4 modulation.

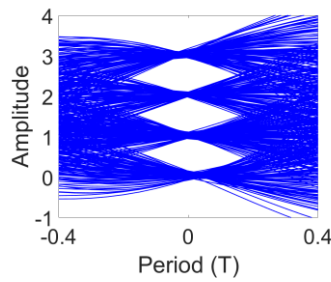


Figure 3.22: recovered eye diagram of PAM-4 based link at 112 Gb/s over 100 m OM4 fibre

The BER performance of the CAP, PAM-4 and DMT based links is plotted in Figure 3.23(b). The green line indicates the HD-FEC limit. The receiver sensitivity to achieve the BER threshold for HD-FEC limit of 3.8×10^{-3} was found to be -2.4 dBm, -1.2 dBm and -0.7 dBm for the CAP-16, PAM-4 and DMT- based links respectively. The use of the proposed CAP equaliser provided a 1.2 dB and 1.7 dB improvement in receiver sensitivity over PAM-4 and DMT respectively. The DMT-based signal transmission suffered from high peak-to-average power ratio (PAPR) and clipping ratio power penalty which resulted in a poorer performance. It was also found that PAM-16 transmission fails at this data rate as the transmitted symbols could not be successfully recovered at the receiver. The eye diagrams are shown in Figure 3.24.

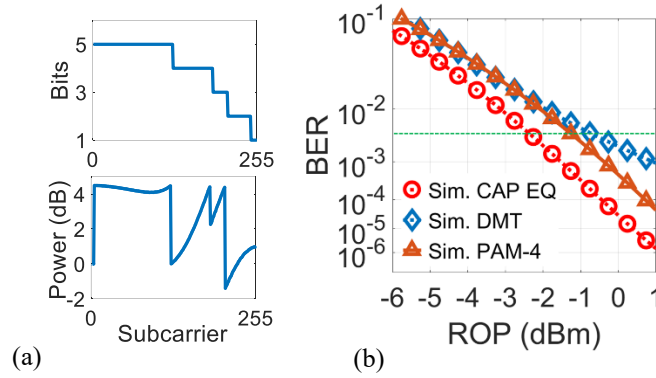


Figure 3.23: (a) Adaptive power and bit loading in the DMT modulation scheme. (b) BER plots comparison for the CAP-16 with CAP equaliser, PAM-4 and DMT scheme at 112 Gb/s over 100 m of OM4 MMF (ROP: received optical power).

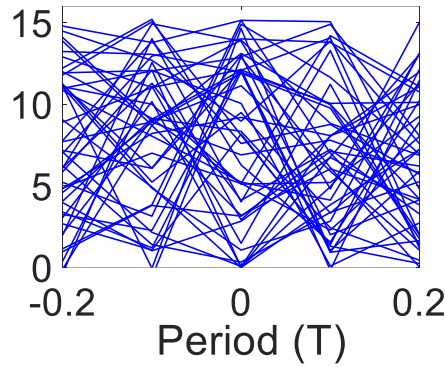


Figure 3.24: recovered eye diagram of PAM-16 based link at 112 Gb/s over 100 m OM4 fibre

As a short PRBS length may cause the absence of some amplitude transitions in the transmitted CAP waveforms, the BER performance of the link is also evaluated for a longer PRBS pattern of $2^{15}-1$ when the tap coefficients of the CAP equaliser are kept the same as the ones used for the transmission of the $2^{11}-1$ data pattern. The obtained BER is shown in Figure 3.25 and is compared with that obtained for the shorter pattern. A very similar performance is observed with a small difference of 0.3 dB obtained in the receiver sensitivity required to achieve the BER threshold of 3.8×10^{-3} for HD-FEC due to the use of the longer pattern.

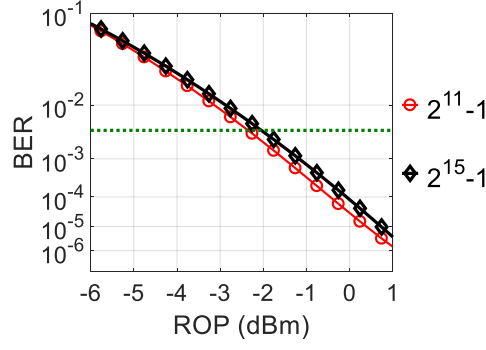


Figure 3.25: Simulated BER results for the 112 Gb/s CAP-16 based data transmission over 100 m of OM4 MMF using a $2^{11}-1$ and $2^{15}-1$ PRBS pattern (ROP: received optical power)

3.3.2.2. Experimental results

Data transmission measurements were carried out on an OM4 MMF link using an 850 nm MM VCSEL. The schematic of experimental setup is shown in Figure 3.26.

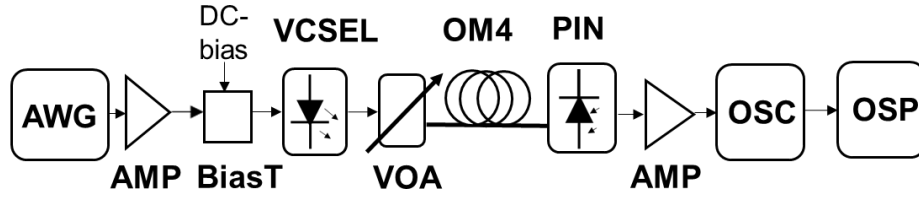


Figure 3.26: Experiment setup used in the data transmission tests (AWG: arbitrary waveform generator, AMP: electrical amplifier, VOA: variable optical attenuator, OSC: real-time oscilloscope, OSP: offline signal processing)

At the transmitter end, a 92 GS/s arbitrary waveform generator (AWG, Keysight M8196A) with a 32 GHz analogue bandwidth was used to generate the high-speed modulating signal and a 38 GHz RF amplifier (SHF 806E) was employed to amplify the signal to a peak-to-peak amplitude of 1.5 V. The RF modulating signal was fed to an 850 nm MM VCSEL via a 40 GHz bias tee. The VCSEL had a 3 dB bandwidth of 25 GHz and emitted ~ 7 dBm at the bias current of 12 mA. The emitted light was coupled to a 50 μm MMF patchcord via a pair of 16 \times microscope objectives (numerical aperture of 0.32). A

multimode variable optical attenuator (VOA, Agilent N7766A) was employed to adjust the level of the received optical power. Two different lengths of 50 μm OM4 MMF were tested: 100 m and 150 m. The performance for the back-to-back (b2b) link (no OM4 fibre) was also measured to provide a reference for the link performance. At the receiver end, a fibre-coupled 30 GHz PIN photodiode (D30-850M) was used to convert the received optical signal to its electrical counterpart, while a 40 GHz RF amplifier (SHF 807) amplified the electrical signal. The received waveform including 250 periods of the signals was captured with a 70 GHz sampling oscilloscope (Tektronix DPO77002SX). The averaged waveform was calculated and offline processed using Matlab. The offline signal processing included demodulation, equalisation and BER estimation as illustrated in Figure 3.11. As in the simulation studies, for the CAP-based transmission, the matched filter and equaliser (conventional or CAP equaliser) was applied on each channel to recover the transmitted symbols. The conventional equaliser comprised a 27-tap FFE and a 27-tap DFE for each channel, while each part of the CAP equaliser (FFE and DFE) consisted of 22 taps for the main channel and 5 taps for the other (crosstalk) channel. As a result, both equalisers had the same total length. For the DMT-based transmission, adaptive power and bit loading were employed at the transmitter while at the receiver a single-tap equaliser was used to recover the signal. The estimation of the BER was based on the assumption of Gaussian white noise using the measured root-mean-square noise amplitude for the different levels of average received optical power and considering the noise enhancement introduced by the equaliser.

Figure 3.27 shows the constellation diagram of the averaged received signals for 112 Gb/s CAP-based transmission for the back-to-back (b2b) link and the 100 m and 150 m OM4 MMF links when the conventional and CAP equalisers are employed. It is clear from Figure 3.27(a)-(c) that the conventional equaliser enables signal recovery only for the b2b link and fails for both the 100 m and 150 m MMF links. On the other hand, the use of the proposed CAP equaliser yields clear constellation diagrams for all link lengths allowing the successful recovery of the transmitted symbols in all cases, as shown in Figure 3.27(d)-(f).

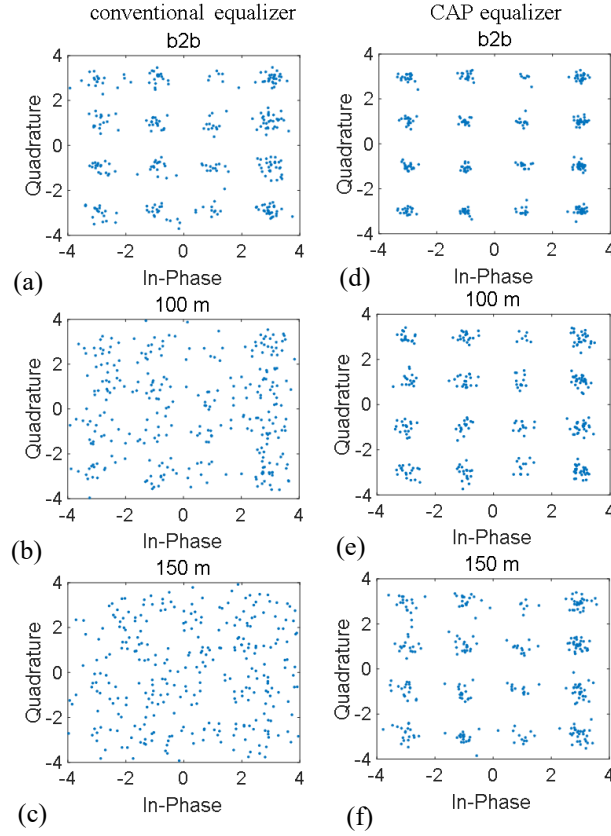


Figure 3.27: Constellation diagrams at 112 Gb/s for a received optical power of 0 dBm for the different links and types of employed equalisers: (a)-(c) conventional equaliser and (d)-(f) CAP equaliser

Figure 3.28 shows the error convergence obtained for the two equalisers with the LMS algorithm over 100 m OM4 fibre. For the conventional equaliser, the RMS errors can only converge to a value of ~ 2 and clearly further increasement of the iteration number does not take much effects. In contrast, the CAP equaliser is able to recover the signal as the RMS errors converse to ~ 0.6 . Based on the measured noise, the BER is estimated by adding the appropriate amount of noise, considering the effect of the noise enhancement of the equaliser, to the equalized waveforms.

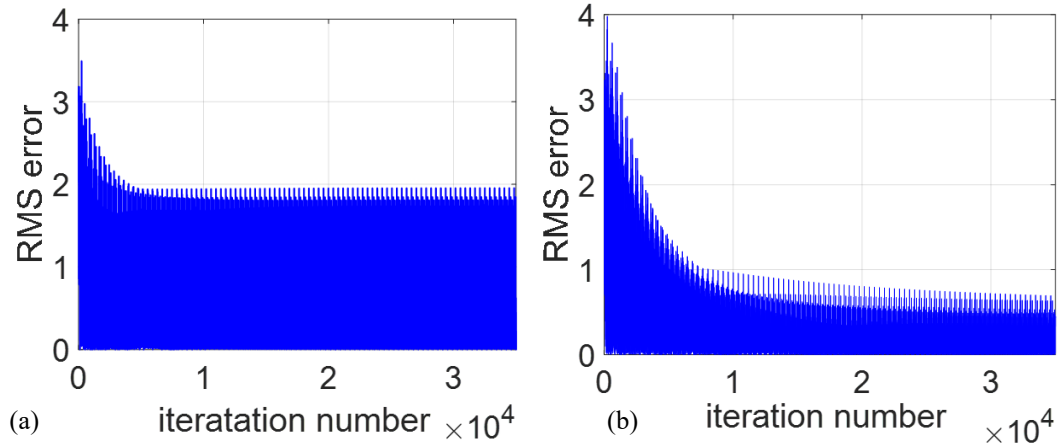


Figure 3.28: Training interacted error lines for 112 Gb/s over 100 m OM4 fibre: (a) conventional equaliser, (b) CAP equaliser. (RMS: root mean square)

Figure 3.29 shows the BER curves obtained for the different links tested. As noted above, the link with the conventional equaliser only works for the b2b case and as a result, only this BER curve is plotted. The use of the equaliser link with the CAP equaliser demonstrates a receiver sensitivity for the HD-FEC BER threshold of -3.8 dBm, -1.9 dBm and 0.5 dBm for the b2b, 100 m and 150 m OM4 MMF link respectively. As in the simulation studies, the BER performance of the 100 m OM4 MMF link when CAP-based transmission and the CAP equaliser are employed are compared with that obtained when DMT modulation is applied. The DMT parameters used in the data transmission tests are the same as the ones used in the simulations. The adaptive power and bit loading scheme applied in the data transmission experiments is shown in Figure 3.30(a). The obtained BER curves at 112 Gb/s for the two modulation schemes are shown in Figure 3.30(b) as well as the respective plots obtained via the link model. Relatively good agreement between the experimental and simulation results is obtained, with a 0.5 dB difference observed in the obtained receiver sensitivities. The use of CAP modulation in conjunction with the CAP equaliser outperforms the DMT scheme by ~2 dB, achieving a receiver sensitivity of -1.9 dBm for the HD-FEC BER threshold of 3.8×10^{-3} . However, at the BER curve of 10^{-4} , the simulation result has ~1.5 dB difference with the experiment results. This is due to the other nonlinearity effects accumulated from the VCSEL, fibre and receiver such as the square-law effect which are not taken into the simulation model leading to the different gradients of the two BER curves. Considering the purpose to present the principle and the performance of this novel CAP equaliser, the simulation results has

demonstrated the improved performance achieved by this CAP equaliser, which is also according with the experiment results.

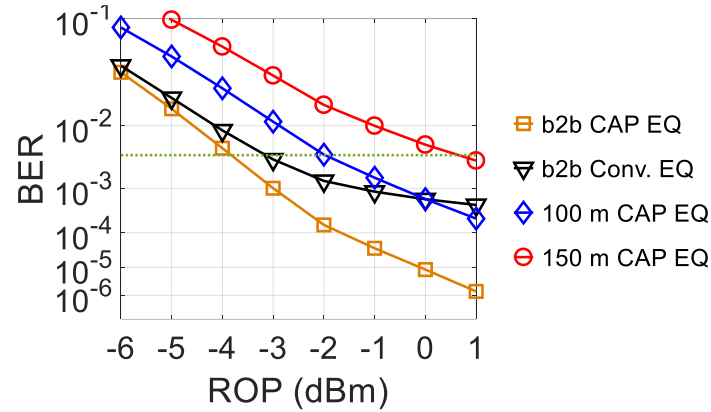


Figure 3.29: Experimental results at 112 Gb/s: comparison of BER performance for the CAP equaliser and conventional equaliser for the (b2b), 100 m and 150 m OM4 MMF links (ROP: received optical power).

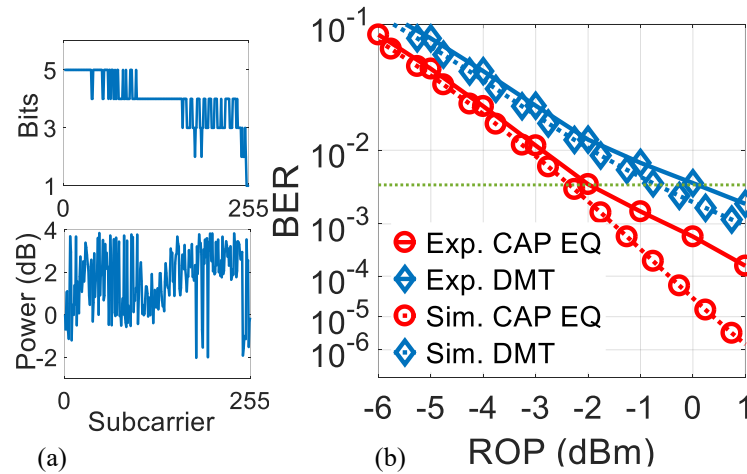


Figure 3.30: (a) Bit and power loading used in the DMT scheme and (b) comparison of BER performance obtained at 112 Gb/s over 100 m OM4 MMF with the CAP equaliser and DMT scheme (Exp.: experimental, Sim.: simulated, ROP: received optical power)

3.4. Conclusion

In this chapter, a novel equaliser structure named the CAP equaliser is proposed for use in conjunction with CAP modulation short-reach high-speed optical links. The proposed equaliser uses the data transmitted on both I- and Q- channels of the link in order to recover the transmitted symbol on each one of them to mitigate the impairment due to the non-linear phase response of the link. In this simulation, the VCSEL is modelled as rate equations; the OM4 fibre is modelled as a Gaussian filter and the raised cosine filter is used for the receiver. The significant performance improvement that this equaliser can achieve over a conventional DFE and FFE equaliser of the same length was demonstrated via simulation studies and data transmission tests on short-reach VCSEL-based OM4 MMF links. Both simulation and experiment results demonstrated that the proposed CAP equaliser greatly outperforms the conventional equaliser, and that the combination of CAP modulation and the proposed CAP equaliser provides better BER performance over the use of adaptive DMT and PAM modulation on the same link. The use of the CAP equaliser enabled CAP-based 112 Gb/s data transmission including 7% FEC overhead (net data transmission 104 Gb/s) over 100 and 150 m of OM4 MMF with a receiver sensitivity of -1.9 dBm and 0.5 dBm respectively for the HD-FEC BER threshold of 3.8×10^{-3} . The conventional FFE and DFE equaliser failed to support the same data rate over the same links while the use of the DMT modulation yielded poorer receiver sensitivity. The proposed CAP equaliser can be implemented without significant additional complexity over the conventional FFE/DFE equaliser structure.

In summary, both simulation and experimental studies have shown the advantage of using the CAP equaliser for VCSEL based OM4 fibre link. Simulation studies have shown a very small additional complexity required compared to the conventional FFE and DFE, which demonstrated the potential use of the CAP equaliser in high-speed optical communication system.

CHAPTER

4

LED-POF LINK USING CAP MODULATION SCHEME AND A NOVEL EQUALISER

4 Gb/s over 25 m and 5 Gb/s over 10 m data transmissions are demonstrated using the CAP equaliser, which shows a significant improvement over the conventional equaliser by both simulation and experiment results. At 4 Gb/s data transmission, the CAP equaliser outperforms the conventional equaliser over all fibre lengths and improves the receiver sensitivity by 0.5 dB and 2.3 dB for b2b and 10 m cases. The conventional equaliser fails to recover the signal at 4 Gb/s over 25 m POF and 5 Gb/s over 10 m POF while the CAP equaliser yields good constellation diagrams for both scenarios.

4.1. Introduction

Step-index plastic optical fibre (SI-POF) has attracted much interest in recent years for use in short-reach (< 50 m) data communication links, such as in-home, automotive and in-plane networks, owing to its low cost, high coupling efficiency from light-emitting diodes (LEDs), ease of installation and high resilience to bending. Visible light LEDs are attractive sources for use in low-cost SI-POF links as they match the low attenuation spectrum and large core size (typically 1 mm in diameter) of standard POFs. The increasing demand for bandwidth in in-home applications, such as ultra-high definition television (8K/16K), and the desire for enhanced passenger experience in car and plane journeys, pushes the required transmission capacity beyond 1 Gb/s over such low-cost links. However, the low bandwidth of POF ($200 \text{ MHz} \times 50 \text{ m}$) and LEDs (typically $\sim 100 \text{ MHz}$) has limited the achievable performance of such links using simple modulation schemes and receivers. As a result, advanced modulation schemes, such as carrierless amplitude and phase modulation (CAP) and pulse amplitude modulation (PAM) have been considered for use in LED-based POF links in order to increase spectral efficiency and achieve data rates $> 1 \text{ Gb/s}$. In addition, equalisation is typically employed in such links in order to mitigate the inter-symbol-interference (ISI) arising from the link dispersion where it enables successful recovery of the transmitted symbols at the receiver. Remarkable results have been achieved using a combination of these techniques. For example, data transmission of 3 Gb/s PAM-8 over 25 m POF [134] and 1.5 Gb/s CAP-64 over 50 m POF [51] have been demonstrated using conventional feedforward (FFE) and decision feedback (DFE) equalisers. In addition, in [141], 5 Gb/s data transmission based on PAM-8 has been reported over 20 m POF using a non-linear Volterra equaliser. It has been experimentally shown that M-CAP modulation provides a better performance over the respective \sqrt{M} -PAM modulation that yields the same spectral efficiency when the received SNR is high enough [55]. However, CAP-based transmission can suffer from I and Q channel crosstalk interference (CCI) when the employed symbol rate exceeds the frequency range where the phase response of the link is linear. In that case, the induced CCI cannot be mitigated by conventional FFE and DFE equalisers. As a result, we proposed a novel equaliser type, named CAP equaliser, which simultaneously suppresses the ISI and CCI in the link, enabling the transmission of higher data rates than these achieved with conventional FFE and DFE equalisers. In this chapter, we apply this new equaliser for the first time in LED-based POF optical links and demonstrate the improvements it can bring in CAP-based data transmission in such links. In this chapter, quoted

transmission data rate includes 7% FEC overhead. We report successful transmission of 4 Gb/s over 25 m POF and 5 Gb/s over 10 m POF using CAP-16 modulation and the proposed CAP equaliser including 7% HD-FEC overhead. Therefore, the net data transmission achieved are 3.7 Gb/s over 25 m POF and 4.7 Gb/s over 10 m POF. The same links using conventional FFE and DFE equalisers fail at these data rates. The new equaliser can be implemented with minimal additional complexity over the conventional FFE and DFE equaliser. Furthermore, the advanced modulation scheme requires a high SNR at the receiver side which imposes a challenge for PIN receiver. Therefore, an APD receiver is used to improve the link performance and the link length. The APD receiver can provide a higher receiver sensitivity than a conventional PIN receiver, enabling a high data rate or longer link reach.

4.2. Simulation model

As illustrated in Figure 4.1, a link model is developed to evaluate the performance of the link. The simulation model consists of an LED transmitter, SI-POF channel and APD receiver and each component employed in the model is studied based on the actual component used in the experiment. At the receiver side, FFE and DFE are employed at the receiver side to suppress ISI and recover signals.

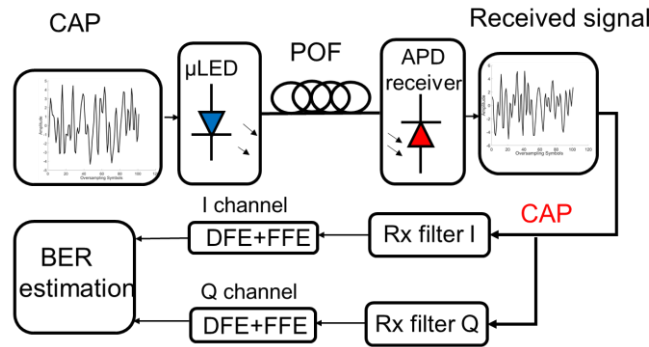


Figure 4.1: Schematic of simulation model

4.2.1. LED

The impulse response of LEDs has been studied in [131] and an exponential impulse response is proposed. The normalized exponential response can be expressed as

$$h_s(t) = \frac{1}{\tau_s} e^{-\frac{t}{\tau_s}} \quad 4-1$$

where τ_s is the time constant of the exponential response. If the 3dBo bandwidth is f_s , the time constant is given by

$$\tau_s = \frac{\sqrt{10^{0.6} - 1}}{2\pi f_s} \quad 4-2$$

The frequency response of the exponential mode is expressed as

$$H_s(f) = (1 + 4\pi^2 f^2 \tau_s^2)^{-\frac{1}{2}} \quad 4-3$$

The μ LED bandwidth is set to be 150 MHz, which is based on the actual measured bandwidth of the μ LED employed in the experimental demonstration. Figure 4.2 shows the frequency response of the exponential LED model with 150 MHz bandwidth.

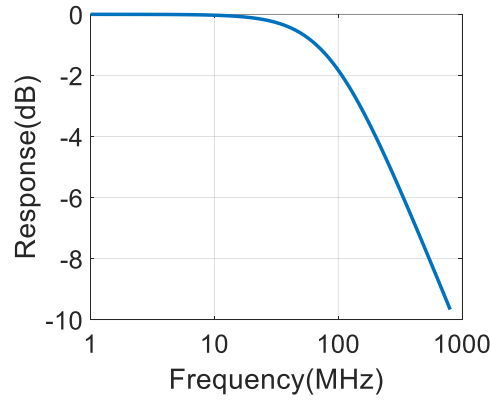


Figure 4.2: Frequency response of the LED model with 150 MHz bandwidth

4.2.2. SI-POF

The core diameter of the SI-POF used in the demonstration is 1mm and light coupled into the SI-POF generates a large number of modes. As stated in Chapter 3, this dispersive channel can be modelled as a Gaussian filter [131]. The bandwidth of the POF channel depends on the link length and the SI-POF used in this work (ESKATM Mega) and the bandwidth distance product of t is 10 MHz·km. The impulse response of the Gaussian model is given by:

$$h(t) = \frac{1}{\sigma\sqrt{2\pi}} e^{\frac{-t^2}{2\sigma^2}} \quad 4-4$$

The frequency response of the SI-POF model at various length is shown in Figure 4.3

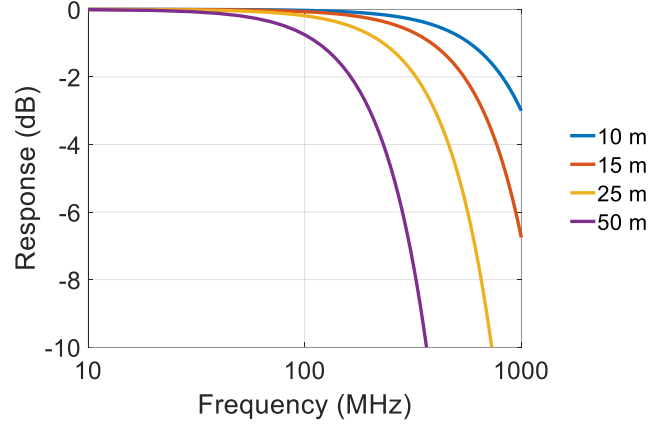


Figure 4.3: Frequency response of the Gaussian POF model for various length

4.2.3. Simulation model of APD receiver

The receiver used in a fibre link can be modelled using a raised cosine frequency response [131]. The normalized impulse response can be written as

$$h(t) = \frac{\sin(5.5\pi t f_r)}{2\pi t(1 - (5.5\pi t f_r)^2)} \quad 4-5$$

The bandwidth of the APD receiver used in this work (First Sensor AD800-11) is measured to be 650 MHz at its operating voltage of 80V which has the optimized multiplication gain. Therefore, a bandwidth of 650 MHz is used in the system modelling. The receiver sensitivity is 0.275 A/W and the frequency response of the APD receiver is illustrated in Figure 4.4.

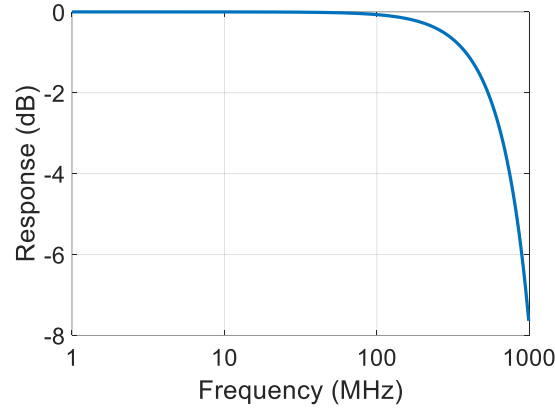


Figure 4.4: Frequency response of raised cosine model of the APD receiver with 650 MHz bandwidth

4.2.4. Overall frequency response and phase response

The μ LED, POF and APD receiver is modelled as exponential, Gaussian and raised cosine response, respectively. Figure 4.5 shows the frequency and phase response of the link based on 25 m POF. It can be clearly seen the nonlinear phase response of the link. The -3 dB bandwidth of the link is ~ 130 MHz, which is limited by the lowest component of the link (LED: 150MHz).

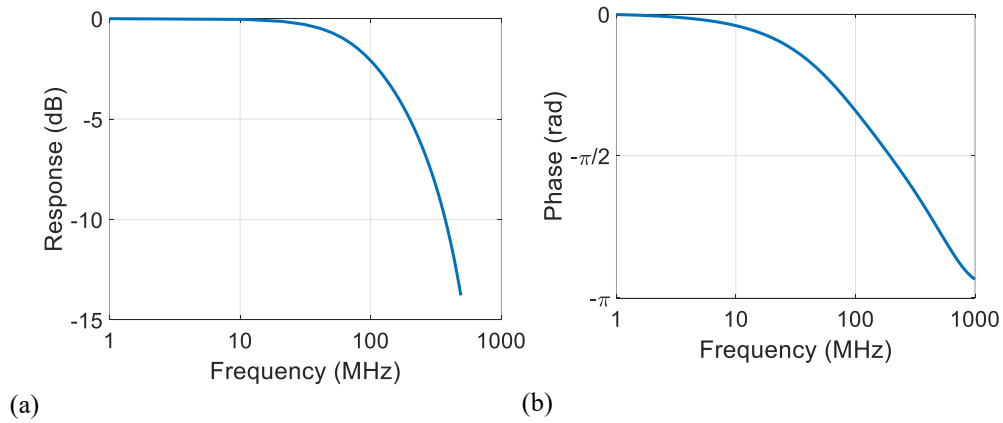


Figure 4.5: Simulated frequency response (a) frequency response and (b) phase response

4.2.5. APD noise measurement

Another important characteristic of the receiver is the noise performance. The APD receiver noise is a

function of the avalanche gain M . In [142], the optimized gain of the APD used in the link is measured to be 14 under the reverse bias of 80 V. The experiment setup to measure the APD-based receiver noise under the optimized gain is shown in Figure 4.6. The total noise of the link is obtained at different level of received optical power without the input RF signal. The noise is considered as additive white Gaussian noise and the standard deviation of the noise can be measured using the histogram function of an oscilloscope.

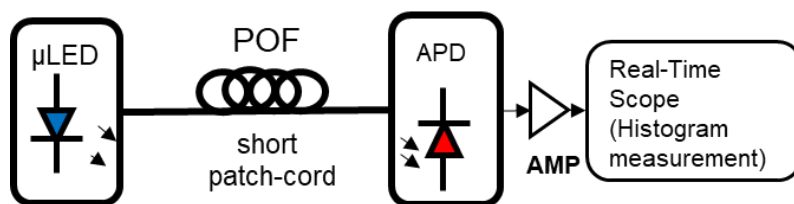


Figure 4.6: Experimental setup for receiver noise measurement

Figure 4.7(a) shows the measured noise performance as a function of the average APD photocurrent. Figure 4.7(b) illustrates the relationship between the APD current and the received optical power. The measured APD receiver noise characteristic is used in the simulation model to evaluate the APD-based link performance.

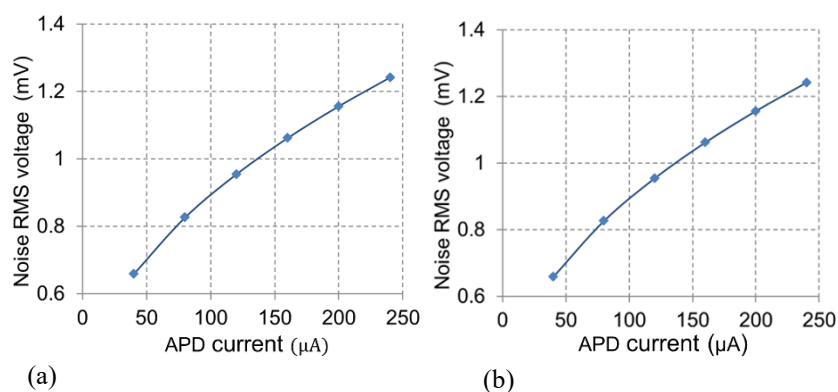


Figure 4.7: Measured APD current versus (a) noise RMS voltage and (b) received optical power

4.3. Simulation results

Based on the system simulation model, the LED-POF links are simulated using Matlab. The parameters of the simulation models are summarized in Table 4-1. The LED-POF link is investigated using the proposed model with CAP-16 modulation scheme. The ideal modulated signal is generated based on PRBS sequence and passes through the LED, POF and receiver with the predefined response. At the receiver side, the signal is demodulated by two matched filters and equalisation is used to suppress ISI and recover the received signal. In addition, the BER is calculated considering the noise enhancement introduced by the equaliser.

Table 4-1: Summary of simulation parameters

μ LED Transmitter	SI-POF Channel	APD receiver
Wavelength: 450 nm	Attenuation: 0.2 dB/m at	Response: Raised
Emission Power: 0 dBm	450 nm	cosine
Response: Exponential	Response: Gaussian	Bandwidth: 650
Bandwidth: 150 MHz	Bandwidth: 10 MHz \times km	MHz

In order to illustrate the link dispersion, the received waveform at 4 Gb/s over 25 m POF is illustrated in Figure 4.8. It can be clearly seen that the received signal is severely distorted. In order to further address this issue, Figure 4.9 shows the constellation diagram of the received signals before equalisation over 25 m of POF at various data rates.

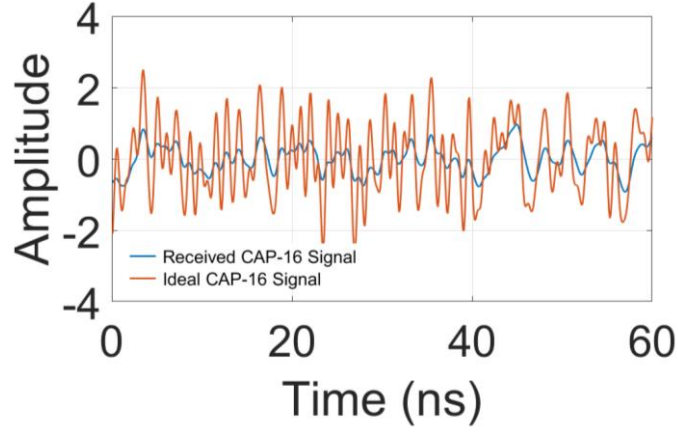


Figure 4.8: ideal and received waveforms over 25 m POF at 4Gb/s.

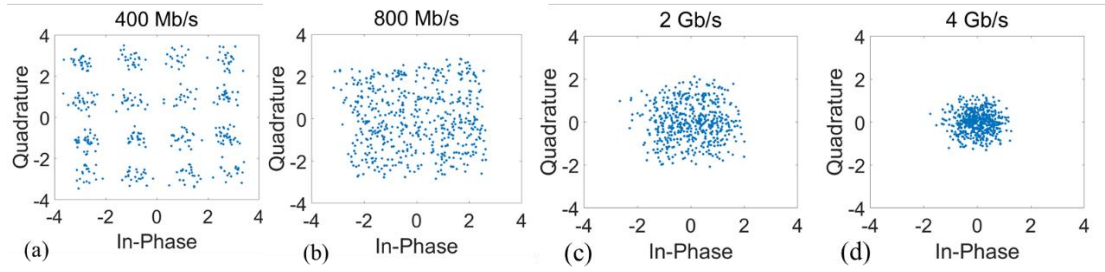


Figure 4.9: Constellation diagram (before equalisation) over 25 m POF length at various data rate: (a) 400 Mb/s (100 MBaud), (b) 800 Mb/s (200 MBaud), (c) 2 Gb/s (500 MBaud) and (d) 4 Gb/s (1 GBaud)

The demodulated symbols can be clearly distinguished only at 400 Mb/s while the demodulated symbols are not able to be decoded at the other data rates due to the ISI introduced by limited bandwidth. Therefore, equalisation technique (FFE and DFE) is applied to suppress the ISI and recover the demodulated symbols.

As demonstrated in Chapter 3, the crosstalk issue due to the nonlinear phase response is firstly studied. PRBS-11 is used as the transmitted data at both: (a) low (100 MBaud, 400 Mb/s) and (b) high (1GBaud, 4Gb/s) symbol rates with the Q- channel off (no data) and on (transmitting data). Figure 4.10 shows the normalized demodulated I- channel symbols for the two modes of operation at two symbol rates before equalisation. It can be clearly seen that the Q- channel only distorts the received signal on the I- channel at 1GBaud (4 Gb/s), demonstrating the presence of the channel crosstalk due to the non-linear phase response at high data(symbol) rate.

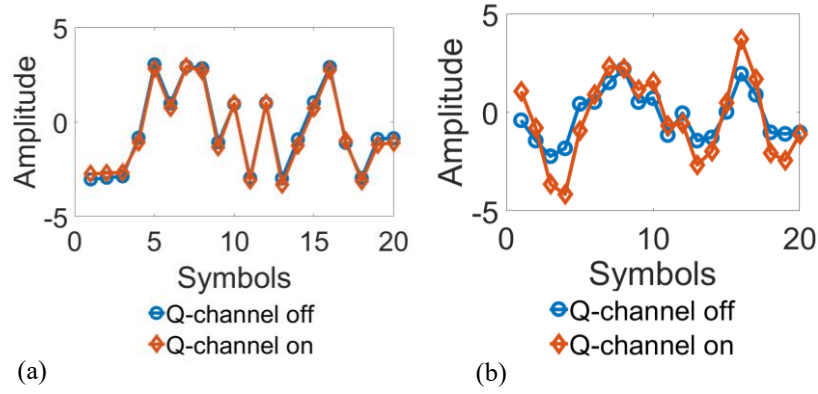


Figure 4.10: Demodulated I- channel symbols for the two modes of operation before equalisation at two different symbol rates (a) 100 MBaud (400 Mb/s) and (b) 1 Gbaud (4 Gb/s)

The principle of FFE and DFE has been detailed introduced in the previous Chapter 3. The conventional equaliser has 60 FFE taps and 60 DFE taps while the CAP equaliser has 45 FFE taps and 45 DFE taps on the main channel and 15 FFE taps and 15 DFE taps on the other channel. Therefore, both types of equalisers have same total tap length. Figure 4.11 shows the error vector magnitude (EVM) of recovered symbols based on the conventional equaliser with different tap lengths.

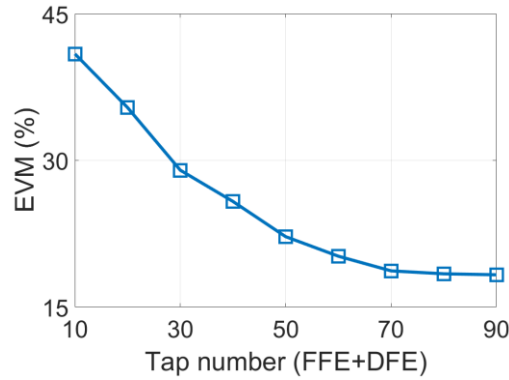


Figure 4. 11: Calculated EVM as a function of the number of taps for the conventional equaliser for 4 Gb/s transmission over 25 m POF.

The results clearly demonstrated the performance of conventional equaliser saturates with ~ 45 FFE and 45 DFE taps at EVM of $\sim 18\%$. Therefore, the performance of CAP equaliser is based on the main channel 45 FFE and 45 DFE taps. Additional taps are added on both main channel and the other channel to further evaluate the equalisers performance. Figure 4.12 illustrates that the increased tap length from the main channel does not lead to an improved performance while the additional tap lengths from the crosstalk channel improve the EVM performance and finally saturates with 15 FFE and 15 DFE crosstalk

channel taps at a value of $\sim 3\%$.

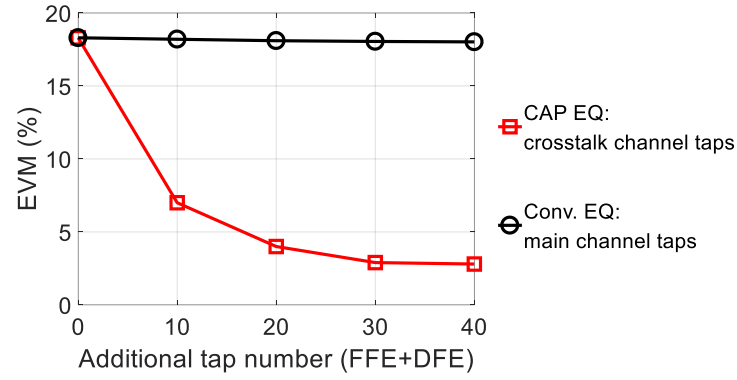


Figure 4. 12: Calculated EVM as a function of the number of additional taps from the main and other channels for 4 Gb/s transmission over 25 m POF.

Figure 4.13 shows the demodulated map after both CAP and conventional FFE and DFE at 4 Gb/s over various lengths of POFs. Both equalisers have same tap spacing (half symbol period). The conventional equaliser can support the link length up to 10 m and fails at 25 m length, while the CAP equaliser recovers symbols over all lengths of POF with very clear constellation diagrams.

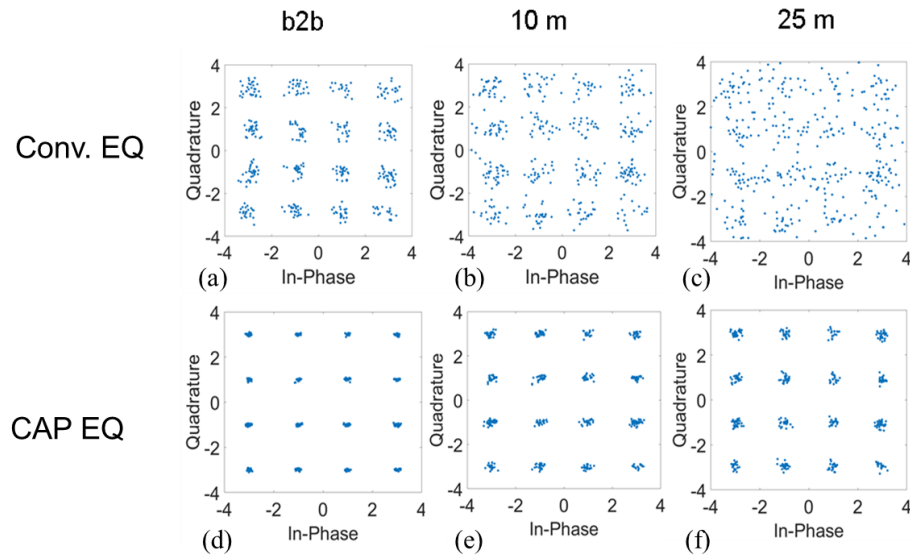


Figure 4.13: Demodulated I- channel symbols for the two modes of operation before equalisation at two different symbol rates (a) 100 MBaud (400 Mb/s) and (b) 1 Gbaud (4 Gb/s)

Figure 4.14 shows the interacted training RMS errors for both types of equalisers over 25 m POF at 4 Gb/s. The error line cannot converge to a satisfied level (<1) for the conventional equaliser, whereas the CAP equaliser achieves a very small error, converging to a range of 0.1. For all link lengths, CAP

equaliser has much smaller ISI than the conventional equaliser.

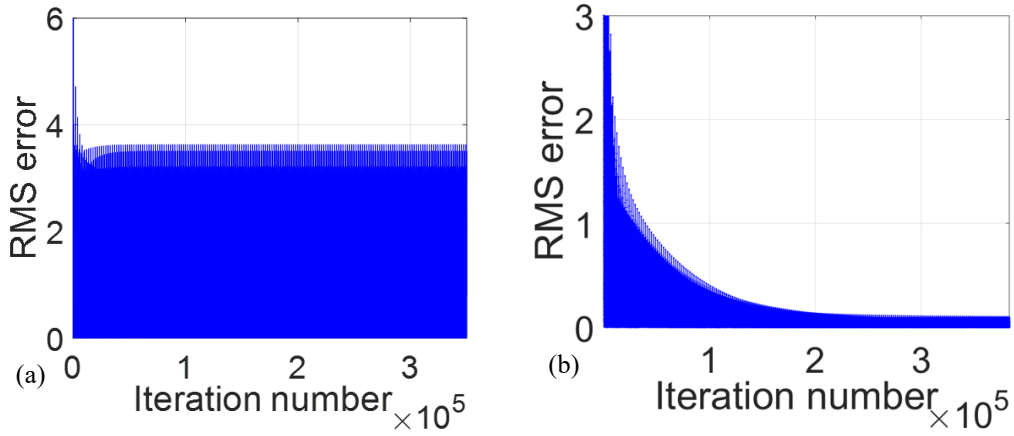


Figure 4.14: Interacted training RMS errors over 25 m POF at 4 Gb/s using: (a) conventional equaliser and (b) CAP equaliser

The BER estimation is based on the measured noise performance. The load resistance is 50 ohms while the amplifier gain is set to be 20. The BER performance of CAP equaliser at 4 Gb/s over 25 m is shown in Figure 4.15. The CAP equaliser achieves better performance over the conventional equaliser owing to the much smaller residual ISI. For 10 m data transmission based on CAP equaliser, it achieves lower BER result than the conventional equaliser at b2b case when the received optical power is larger than -14 dBm. The similar results can be also found for 25 m data transmission based on CAP equaliser. The reason is that the link performance based on conventional equaliser is severely influenced by the residual ISI. At the data rate of 4 Gb/s, CAP equaliser achieves HD-FEC limit with receiver sensitivity of -20 dBm, -18.3 dBm and -15.2 dBm for b2b, 10 m and 25 m POF length, respectively. In comparison with the conventional equaliser, it improves the sensitivity by 0.2 dB and 1.3 dB for the b2b and 10 m link length.

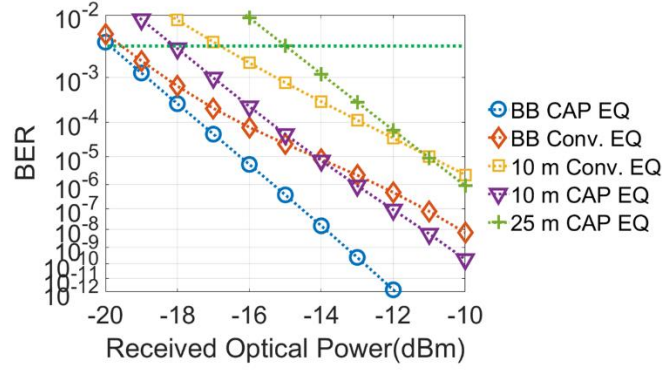


Figure 4.15: Simulated BER results at various link lengths (b2b, 10 m, 25 m) with both equalisers at 4 Gb/s.

4.4. Experimental results

The experimental setup used in this work is illustrated in Figure 4.16(a). A 450 nm GaN micro-pixelated LED (μ LED) [6] is used as the transmitter and an 800 μ m-diameter APD (First Sensor AD800-11) is employed at the receiver. The light-current and bandwidth-current characteristics of the LED used in this work are shown in Figure 4.16(b). At the transmitter side, the CAP-16 modulating signal is generated by an arbitrary waveform generator (AWG, Tektronix 70000A), is amplified by an RF amplifier (SHF826B) to 3 V peak-to-peak amplitude and is fed to the μ LED via a bias tee. The μ LED is biased at 6.2 V (60 mA bias current) and the emitted light is coupled into a 1 mm in diameter Eska-Mega POF via an optical lens. It can be clearly seen from Figure 4.16(b) (black line) that the μ LED exhibits a 3 dB bandwidth of ~ 140 MHz at this bias current. At the receiver side, the light from the POF is coupled to the APD receiver via a pair of optical lenses. The received signal is amplified either by a 1 GHz low noise amplifier (ZFL-1000LN) for the 4 Gb/s transmission tests or by a 2.2 GHz transimpedance amplifier (Femto HAS-X-1-2-40) for the 5 Gb/s tests and captured by a digital phosphor oscilloscope (Tektronix DPO77002SX) for offline signal processing. This includes demodulation, equalisation and the bit error rate (BER) calculation.

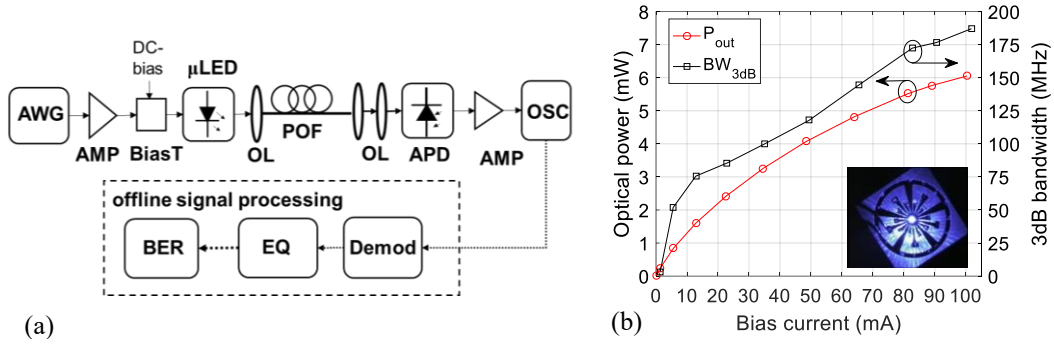


Figure 4.16: Schematic of experimental setup for μ LED-POF link (AWG: arbitrary waveform generator, AMP: electrical amplifier, OA: optical attenuator, OSC: real time oscilloscope, OSP: offline signal processing)

Similar to simulation results, Figure 4.17 shows the constellation diagram before equaliser over 1 m (b2b), 10 m and 25 m POF length at 4 Gb/s. It can be clearly seen that the signal is severely distorted and is not able to be decoded if no further signal processing technique applied.

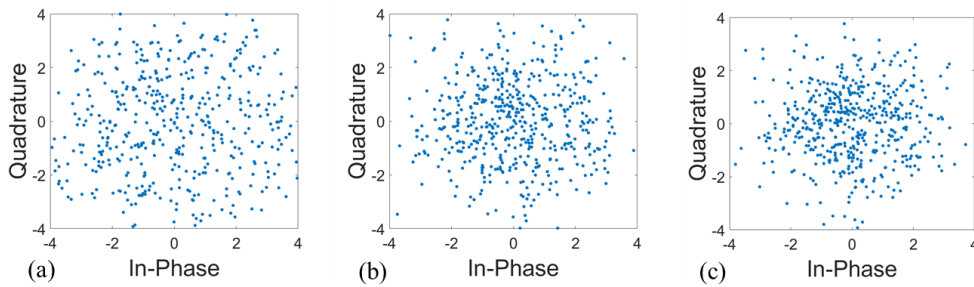


Figure 4.17: Constellation diagram before equalisation at 4 Gb/s for APD current of 240 μ A for (a) b2b, (b) 10 m and (c) 25 m POF link lengths

Figure 4.18 shows the constellation diagram of the received signals after equalisation for both types of equalisers. The conventional equaliser can successfully recover the transmitted symbols for the b2b and 10 m POF link but fails for the 25 m POF link at this data rate. The CAP equaliser yields clear constellation diagrams for all POF lengths supporting 4 Gb/s data transmission up to 25 m POF.

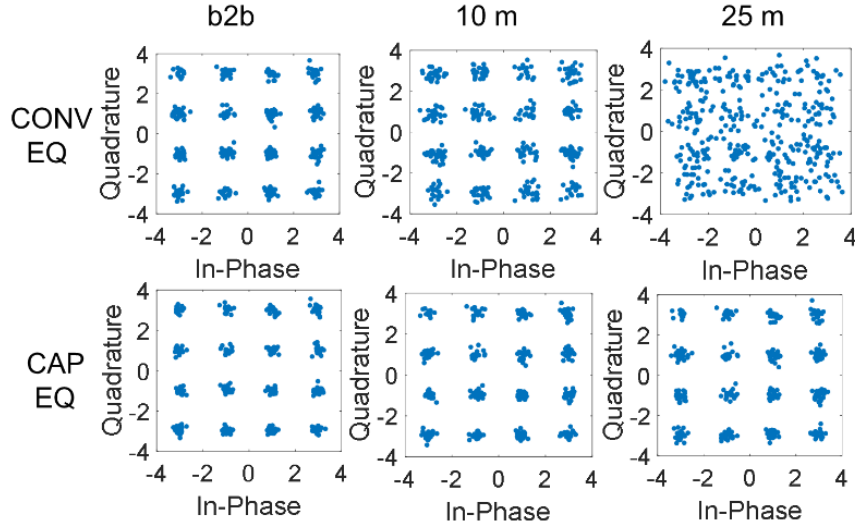


Figure 4.18: Constellation diagrams at 4Gb/s for APD current of 240 μ A for the different links and types of employed equalisers (CONV: conventional, EQ: equaliser)

Figure 4.19 shows the obtained BER plots for both equalisers for the links studied. The BER plot for the conventional equaliser and 25 m link does not appear as data transmission fails at this data rate. Clearly the CAP equaliser outperforms the conventional equaliser over all POF lengths. The receiver sensitivity to achieve the required HD-FEC limit is found to be -17.2, -14.6 dBm for 10 m and 25 m POF link respectively, when the CAP equaliser is used. The obtained values are an improvement in receiver sensitivity over the conventional equaliser of 1.3 dB for 10 m POF link. Performance improvements are greater when the high-speed data transmission over the link becomes more challenging. Figure 4.20 shows the simulated and experimental BER results at 4 Gb/s including FEC overhead over 25 m POF length. A good match between the experiment and simulation result with a difference of <1 dB at $\text{BER}=10^{-3}$. The simulation model here includes the bandwidth limitation for the link while the nonlinear effects except the nonlinear phase accumulated from the μLED , POF and also APD received does not include in the simulation, which cause difference of the gradients between two BER curves in Fig 4.20. However, this effect dose not influence the demonstration of this novel CAP equaliser.

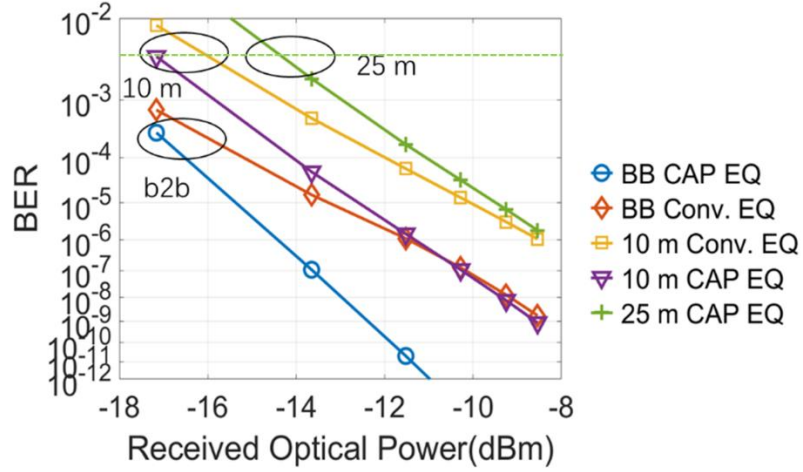


Figure 4.19: Experimental BER performance for both types of equalisers over 1 m (b2b), 10 m and 25 m PO lengths at 4 Gb/s

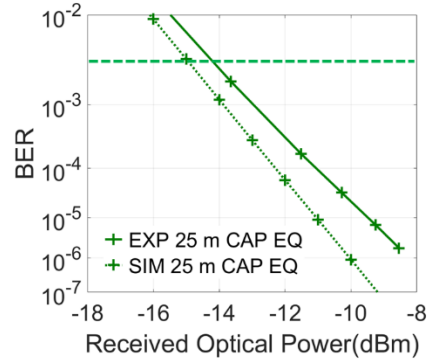


Figure 4.20: Simulated and Experimental BER performance over 25 m PO length at 4 Gb/s

The potential to achieve higher data rates over the 10 m PO length link is further explored. Figure 4.21(a) and (b) show respectively the constellation diagram of the received signal after equalisation for 5 Gb/s CAP-16 transmission over 10 m PO length using the conventional and CAP equaliser. The link using the conventional equaliser fails at 5 Gb/s over the 10 m PO length. The BER performance of the link employing the CAP equaliser is shown in Figure 4.21(c). The receiver sensitivity is found to be -15.8 dBm for 5 Gb/s data transmission including 7% FEC overhead. In comparison with 4 Gb/s over 25 m, although the data rate slightly increase, it has ~ 1 dB receiver sensitivity improvement owing to the shorter PO length.

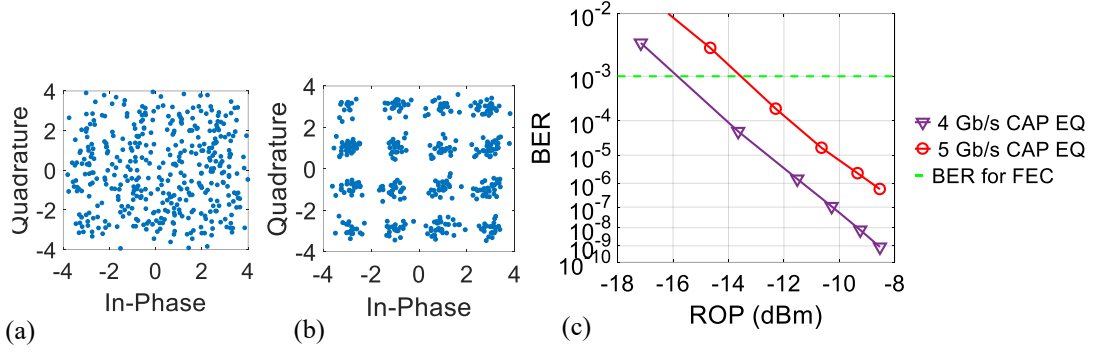


Figure 4.21: Constellation diagram of the equalized waveforms for (a) the conventional and (b) the CAP equaliser at 5 Gb/s over the 10 m POF link and (c) BER performance obtained with the CAP equaliser at 4 Gb/s and 5 Gb/s over 10 m POF (EQ: equaliser ROP: received optical power)

4.5. Conclusion

In this chapter, the net data transmission of 3.7 Gb/s data transmission over 25 m and 4.7 Gb/s over 10 m has been demonstrated using CAP equaliser, which has shown a significant improvement over the conventional equaliser by both simulation and experiment results.

A simulation link using APD receiver in conjunction with CAP-16 modulation scheme is developed. In the simulation, the μ LED is modelled with an exponential response; the SI-POF is assumed having a Gaussian response and a raised cosine response is used for the APD receiver. At the receiver side, conventional equaliser (FFE and DFE) and CAP equaliser is employed to suppress the ISI introduced by the limited bandwidth. Simulation results has shown the conventional equaliser can only support up to 10 m data transmission at 4 Gb/s while the CAP equaliser can extend the data transmission to 25 m POF length. Moreover, the CAP equaliser achieves much smaller residual ISI than the conventional one and better BER performance for all link lengths (b2b, 10 m and 25 m).

CAP-16 based POF link is also built experimentally in this work using a GaN μ LED and an APD receiver. The link performance is based on the equalized waveforms and measured APD noise. For 4 Gb/s data transmission, both CAP equaliser and conventional equaliser are tested at various link lengths (b2b, 10 m and 25 m). Similar results are obtained in the experiment. The CAP equaliser outperforms the conventional equaliser over all fibre lengths. It improves the receiver sensitivity by 0.5 dB and 2.3 dB

for b2b and 10 m cases. The conventional equaliser fails to recover the signal over 25 m POF while the CAP equaliser yields a good constellation diagram over this distance. In addition, 5 Gb/s over 10 m POF data transmission has also been achieved by CAP equaliser while the conventional one fails to recover the received signal.

In summary, both simulation and experimental studies have demonstrated the significant improved link performance using CAP equaliser over that based on conventional equaliser, which indicates the potential use of CAP equaliser in LED-POF links to improve the link performance and transmission capacity.

CHAPTER

5

A FEED-FORWARD

PRE-EQUALISER FOR CAP BASED

HIGH SPEED SHORT REACH OPTICAL LINKS

A novel type of pre-equaliser named pre-CAP-equaliser is proposed for the first time for use in short-reach optical links employing CAP modulation scheme. The proposed equaliser uses the symbols transmitted on both channel symbols to pre-equalize the transmitted waveforms and mitigate cross channel interference due to the nonlinear phase response of the link. The data transmission experiments at 56 Gb/s demonstrate a 0.7 improvement in receiver sensitivity respectively over the corresponding CAP-based post-equalisation scheme. Simulation studies indicate that a larger sensitivity improvement of 2 dB can be achieved at 112 Gb/s using the proposed scheme owing to the efficient suppression of the noise enhancement power penalty.

5.1. Introduction

Equalisation can be applied both at transmitter, referred to as pre-equalisation, and receiver side known as post-equalisation [132, 143, 144]. Pre-equalisation has been widely utilized in recent publications [145-147]. Equalisation at the transmitter provides a better noise performance as the pre-equaliser affects only the transmitted signal while the use of the post-equaliser introducing the noise enhancement power penalty which degrades the system performance. In addition, post-equaliser struggles with the narrowband filtering impairments. Various studies have been reported in literature comparing the two schemes. For example, in [145] the use of feed-forward pre-equalisation is studied in the context of a free-space LED-based visible light communication (VLC) link using PAM and is compared with post-equalisation. An improved receiver sensitivity up to 5 dB is achieved when pre-equalisation is employed. Similarly, in [146] and [147], it is demonstrated that the use of pre-equalisation outperforms post-equalisation in the same link.

In this work, we present a new type of pre-equaliser named CAP pre-equaliser, which can provide significant improvements in the performance of high-speed optical links based on CAP modulation. We have experimentally demonstrated a novel equaliser, namely CAP equaliser, on the VCSEL OM4 link with significant performance improvement over the conventional equaliser although a similar equaliser structure for DPSK has also been explored in [148] but only validates on the simulation level. In this work, we take this concept further and propose the use of a similar type of equaliser appropriately modified for use at the transmitter side of the link (pre-equalisation). We describe its structure and operation and demonstrate the improvements it can bring in link performance using simulation studies and experiments in a VCSEL-based 100 m OM4 MMF link operating at 56 and 112 Gb/s including 7% FEC overhead. Therefore, the net data transmission is 52 Gb/s and 104 Gb/s, respectively. It is shown that the proposed pre-equalisation scheme using the new CAP equaliser outperforms the respective post-equalisation scheme achieving a 2 dB improvement in receiver sensitivity for the 112 Gb/s 100 m OM4 link.

5.2. Feed-forward pre-equaliser structure

In CAP-based systems, the transmitted signal $s_T(t)$ is the superposition of the modulating signals $s_I(t)$ and $s_Q(t)$ on the I- and Q- channels and can be described as

$$s_T(t) = s_I(t) + s_Q(t) = D_I \otimes I(t) + D_Q \otimes Q(t) \quad 5-1$$

where D_I and D_Q are the I- and Q- channel encoded symbols and $I(t)$ and $Q(t)$ are the I- and Q- channel transmitter (Tx) passband filter functions. At the receiver side, the received signal on each channel is demodulated by the respective matched filter and is given by

$$s_{r,I}(t) = s_T(t) \otimes h(t) \otimes I_M(t) \quad 5-2$$

$$s_{r,Q}(t) = s_T(t) \otimes h(t) \otimes Q_M(t) \quad 5-3$$

where $h(t)$ is the impulse response of the link, and $I_M(t)$ and $Q_M(t)$ are the receiver (Rx) matched filters of the I- and Q- channel respectively. The received symbols r_I and r_Q on each channel are obtained after sampling the respective received waveform $s_{r,I}(t)$ and $s_{r,Q}(t)$. However, CAP-based transmission suffers from a non-linear link phase response which destroys the signal orthogonality and generates crosstalk between the two channels. In order to mitigate this issue, we recently proposed a novel type of equaliser, named CAP-equaliser which uses the symbols transmitted on both channels to recover the symbol transmitted on each. It comprises a combination of a FFE and a DFE applied on both the main channel (where the symbol decision is made) and the other (crosstalk) channel. It has already been shown in Chapter 3 and Chapter 4 that only a small number of additional taps operating on the crosstalk channel are required to achieve significant performance improvements in the link. Figure 5.1 shows post-CAP-equaliser operation principle

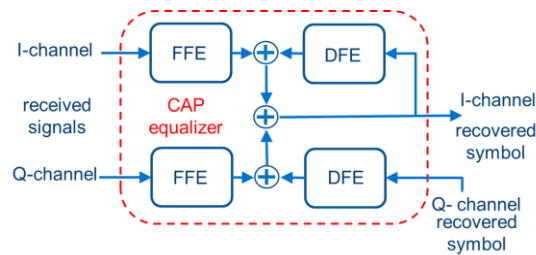


Figure 5.1: CAP equaliser operation principle

As introduced in Chapter 3 and Chapter 4, Figure 5.2 illustrates the basic structure of this new CAP equaliser applied to recover the I- channel symbols when the FFE tap delay is set to half of the symbol period ($T/2$).

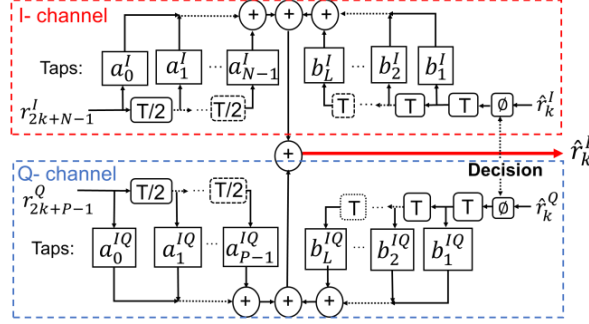


Figure 5.2: The CAP equaliser (CAP-EQ) applied on I- channel

Same structure can also be applied to recover Q- channel symbols. Equation 5-4 gives the expression used to obtain the k -th demodulated symbol \hat{r}_k^I on the I-channel

$$\hat{r}_k^I = \sum_{n=0}^{N-1} a_n^I r_{2k+N-1-n}^I + \sum_{m=1}^V b_m^I \phi(\hat{r}_{k-m}^I) + \sum_{p=0}^{P-1} a_p^{IQ} r_{2k+N-1-p}^Q + \sum_{l=1}^L b_l^{IQ} \phi(\hat{r}_{k-l}^Q) \quad 5-4$$

where r_i^I and r_j^Q are the corresponding i -th I- and j -th Q-channel demodulated symbols sampling at half of symbol period, N , V , P , Q are the number of taps for the FFE and DFE part for the I- and Q-channels respectively, a_n^I and b_m^I are the coefficients of the n -th FFE and m -th DFE taps from I- (main) channel, and a_p^{IQ} and b_l^{IQ} are the p -th FFE and l -th DFE taps from the Q- (crosstalk) channel. $\phi(\cdot)$ represents the decision function. For the same CAP equaliser structure applied on Q- channel, we can expect a_n^Q and b_m^Q for the n -th FFE and m -th DFE taps from Q- (main) channel, and a_p^{QI} and b_l^{QI} for the p -th FFE and l -th DFE taps from the I- (crosstalk) channel. The detailed structure of the Q-channel CAP equaliser is shown in Figure 5.3.

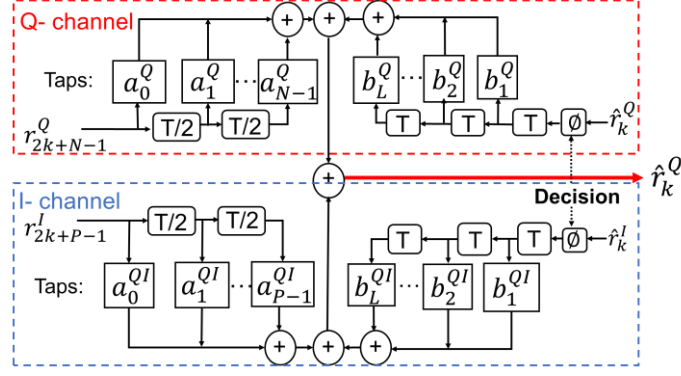


Figure 5.3: The CAP equaliser (CAP-EQ) applied on Q- channel

Theoretically, the main channel FFE taps a^I and a^Q have same values. However, the crosstalk channel taps a^{IQ} and a^{QI} have different values. The relationship between crosstalk channel FFE taps a^{IQ} and a^{QI} are deduced in the following. The crosstalk interferences from either I- or Q- channel to the other one are expressed in **5-5** and **5-6**

$$C_{IQ}(t) = D_I(t) \otimes I(t) \otimes h(t) \otimes Q_M(t) \quad \text{5-5}$$

$$C_{QI}(t) = D_Q(t) \otimes Q(t) \otimes h(t) \otimes I_M(t) \quad \text{5-6}$$

where $C_{IQ}(t)$ refers to crosstalk from I- channel to Q- channel and $C_{QI}(t)$ refers to the crosstalk from Q- channel to I- channel. The relationship between transmitter side filters and matched filters can be expressed in **5-7** and **5-8**

$$I_M(t) = I(t) \quad \text{5-7}$$

$$Q_M(t) = -Q(t) \quad \text{5-8}$$

Combined **5-5** with **5-8** and **5-6** with **5-7**, the crosstalk interferences can be further expressed as

$$C_{IQ} = -[I(t) \otimes h(t) \otimes Q(t)] \otimes D_I(t) \quad \text{5-9}$$

$$C_{QI} = [I(t) \otimes h(t) \otimes Q(t)] \otimes D_Q(t) \quad \text{5-10}$$

Therefore, the crosstalk channel taps a^{IQ} and a^{QI} have opposite values theoretically. Same relationships for DFE main channel taps (b^I and b^Q) and crosstalk channel taps (b^{IQ} and b^{QI}) can also be obtained.

In this work, we propose to transfer the FFE part of the CAP equaliser at the transmitter side in order to simultaneously suppress the noise enhancement penalty and mitigate pre-cursor ISI and CCI in the link. The structure of the proposed CAP pre-equaliser is shown in Figure 5.4. It can be clearly seen that the crosstalk issue from the other channel is pre-compensated for both $s_I(t)$ and $s_Q(t)$.

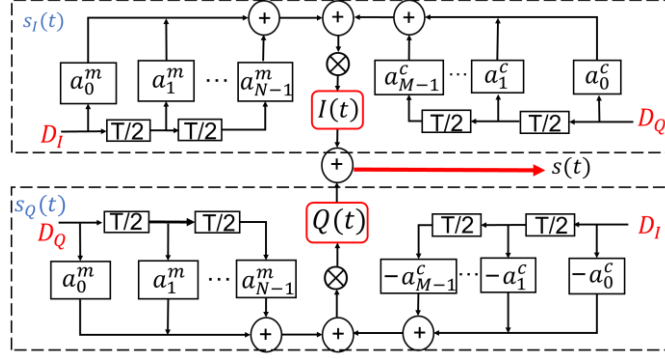


Figure 5.4: Structure of the proposed FFE pre-equaliser

The expressions that give the modulating signals $s_I(t)$ and $s_Q(t)$ on each channel are provided in 5-11 and 5-12.

$$s_I(t) = \left(\sum_{n=0}^{N-1} D_I \left[\frac{nk}{2} \right] a_n^m + \sum_{n=0}^{M-1} D_Q \left[\frac{nk}{2} \right] a_n^c \right) \otimes I(t) \quad 5-11$$

$$s_Q(t) = \left(\sum_{n=0}^{N-1} D_Q \left[\frac{nk}{2} \right] a_n^m - \sum_{n=0}^{M-1} D_I \left[\frac{nk}{2} \right] a_n^c \right) \otimes Q(t) \quad 5-12$$

where D_I and D_Q are up-sampled encoded symbols on the I- and Q-channel respectively, k is the up-sampling ratio for the symbols, $I(t)$ and $Q(t)$ are the I- and Q-channel transmitter filter, a_m is the main channel taps and a_c is the crosstalk channel taps (Figure 5.2). Their values are based on the average value of trained main and crosstalk post-CAP-equaliser coefficients shown in 5-13 and 5-14.

$$a^m = \frac{1}{2}(a^I + a^Q) \quad 5-13$$

$$a^c = \frac{1}{2}(a^{IQ} - a^{QI}) \quad 5-14$$

where a^I and b^I are the I-channel main and crosstalk FFE taps, and a^Q and b^Q are the Q-channel

main and crosstalk FFE taps respectively.

At the receiver side, a novel DFE structure in conjunction with one tap FFE (no delay line, just a single scaling factor) is employed to recover the transmitted symbol on each channel. The equaliser scales the received symbol and uses the previous V and L decisions on the main and crosstalk channel respectively to mitigate post-cursor ISI. Figure 5.5 shows the structure of this novel DFE structure applied on I-channel. The recovered symbol \hat{r}_k^I on I- channel is given by:

$$\hat{r}_k^I = c \cdot r_k^I + \sum_{m=1}^V \phi(\hat{r}_{k-m}^I) b_m^I + \sum_{n=1}^L \phi(\hat{r}_{k-n}^Q) b_n^{IQ} \quad 5-15$$

where r_k^I is the k -th received symbol on the I- channel , b_m^I and b_n^{IQ} are the m -th and n -th DFE tap coefficients of the I- (main) and Q- (crosstalk) channel respectively and c is a scaling factor. Same structure is also employed on Q- channel for symbols recovering.

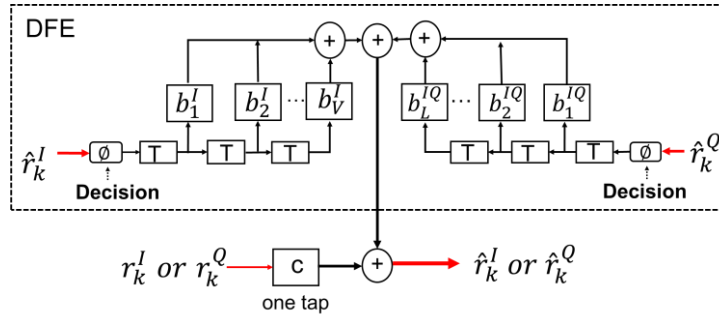


Figure 5.5: The DFE structure at the receiver side applied on I- channel

5.3. Simulation Results

The performance of a high-speed short-reach optical link is studied when the CAP equaliser is employed both at the transmitter and receiver side using an appropriate link model. The link parameters used in the simulation is same as those in the Chapter 3. Figure 5.6(a) shows the post-equalisation based link schematic while Figure 5.6(b) illustrates the link schematic based on the pre-equalisation method. The VCSEL dynamic behaviour is simulated with a rate equation model whose parameters are based on published data of commercially-available VCSEL devices. The response of OM4 MMF and PIN receiver are modelled with a Gaussian and a raised-cosine response respectively.

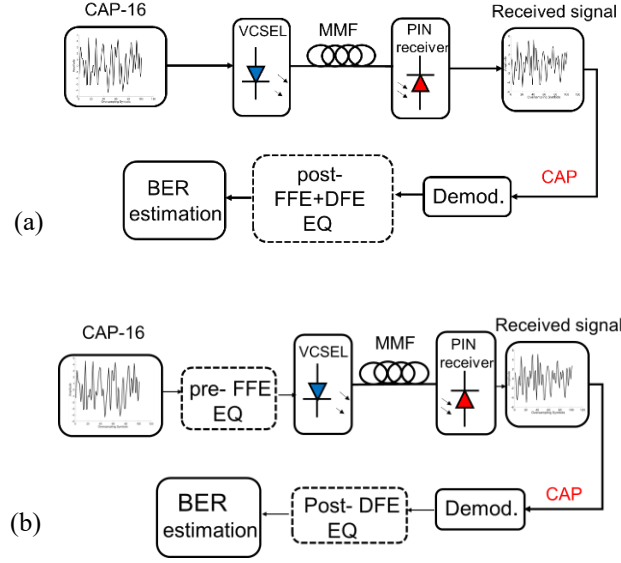


Figure 5.6: Block diagram of link model for the CAP modulation using (a) post-equalisation and (b) pre-equalisation. The pre-equaliser and post-equaliser used in the link can either be a conventional or the proposed new CAP equaliser. (EQ: equaliser, Demod.: demodulation)

The link performance is evaluated when (i) a conventional FFE and DFE equaliser is employed at the receiver (post-CONV-EQ), (ii) the CAP equaliser is used at the receiver (post-CAP-EQ), (iii) the new CAP pre-equaliser is employed at the transmitter together with the modified post-DFE proposed here is used at the receiver (pre-CAP-EQ), and (iv) a conventional FFE and DFE pre-equaliser is used at the transmitter combined with the modified post-DFE proposed here (pre-CONV-EQ). Cases (i) and (ii) have been experimentally validated in Chapter 3, while here simulation results are shown for case (iii) and are compared with the performance obtained for (i) and (ii). Furthermore, the performance of the conventional [pre-CONV-EQ, case (iv)] and new CAP equaliser at the transmitter [pre-CAP-EQ, case (iii)] is also compared and it is shown that significant performance can be achieved using a small number of additional taps on the crosstalk channel. Table 5-1 summarizes the four different type of equalisers and lists the number of taps assumed for each part in each configuration studied. The total number of taps is nearly same between four taps of equalisers to allow a fair comparison. One additional tap for the pre-equalisers is the scaling factor at the receiver side (Figure 5.5).

Table 5-1: equaliser parameters

Scheme	pre-equalizer channel taps		post-equalizer channel taps				Total equalizer taps per channel
	main FFE	crosstalk FFE	main		crosstalk		
			FFE	DFE	FFE	DFE	
(i) CONV-EQ	-	-	25	25	-	-	50
(ii) post-CAP-EQ	-	-	20	20	5	5	50
(iii) pre-CAP-EQ	20	5	1	20	0	5	51
(iv) pre-CONV-EQ	25	0	1	20	0	5	51

The performance of the pre-CAP-EQ on the same link is explored. A separate training and testing pattern are used. A PRBS length of $2^{13}-1$ (PRBS-13) is used as the input data stream and is encoded in a random order into transmitted symbols on each channel. The transmitted symbols are then used to obtain the weight of post- FFE and DFE taps based on the least mean square (LMS) algorithm. The testing pattern consists of the same PRBS-13 pattern but encoded in the normal order. The spacing of FFE taps is half symbol period ($T/2$). The trained FFE and DFE taps are used to recover the distorted received symbols. Based on the trained post-FFE taps from the CAP equaliser, the pre-FFE taps are obtained by transferring the post-FFE taps to the transmitter side according to (8) and (9) while at the receiver side same DFE taps are used to remove the post-cursor ISI.

Figure 5.7 shows the demodulation results at 112 Gb/s over 100 m OM4 MMF link, employing the post-CONV-EQ, post-CAP-EQ and pre-CAP-EQ. No noise is included in the constellation diagrams in order to better visualize the residual ISI and compare the performance of the equalisers. The post-CONV-EQ fails to recover the transmitted symbols, whilst both the pre-CAP-EQ and post-CAP-EQ yield a distinct constellation diagram.

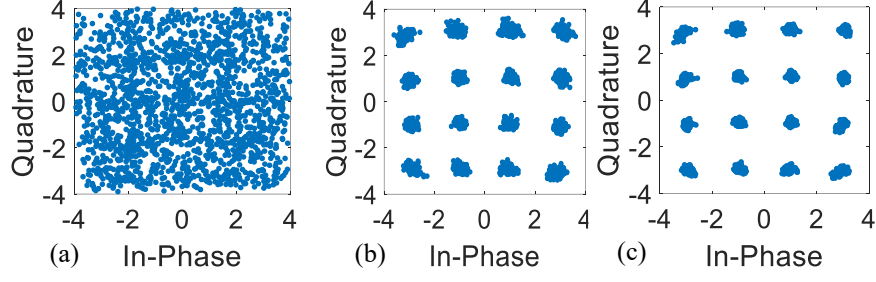


Figure 5.7: Constellation diagrams at 112 Gb/s over 100 m OM4 fibre (a) post-CONV-EQ, (b) post CAP-EQ and (c) pre-CAP-EQ.

Figure 5.8(a) illustrates the first five main channel tap coefficients for both I- and Q- channel (a^I and a^Q). It can be clearly seen that the main channel taps a^I and a^Q nearly overlapped with each other. Figure 5.8(b) shows the crosstalk channel tap coefficients for both I- and Q- channel (a^{IQ} and a^{QI}). As proved in equation 4-10 and 4-11, the crosstalk channel taps a^{IQ} and a^{QI} have opposite value for each coefficient.

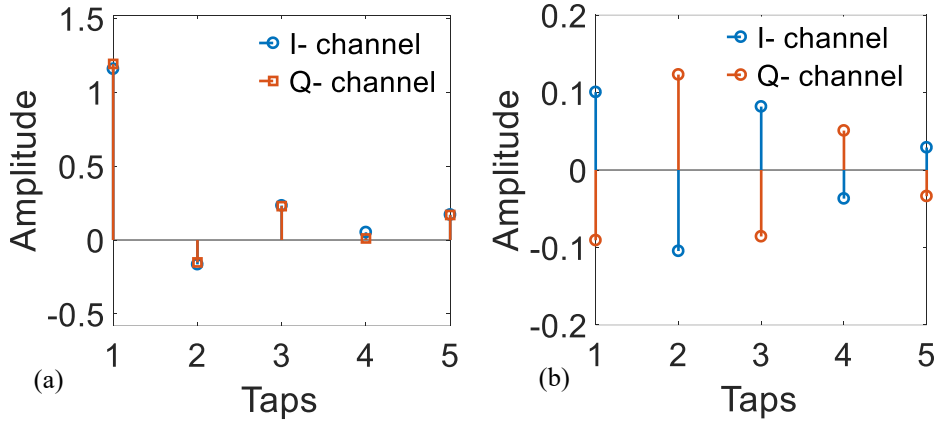


Figure 5.8: For both I- and Q- channels: (a) main channel tap coefficients (first five), (b) crosstalk channel tap coefficients.

In order to further evaluate the performance of the proposed pre-CAP-EQ structure, the performance of the link when a pre-CONV-EQ with the same number of total taps is used at the transmitter. This conventional pre-equaliser, contrary to the proposed pre-CAP-EQ, features FFE taps only on each main channel. To compare their performance, both pre-equalisers are set to have the same number of taps on the main channel (20 taps) and additional taps (up to 5) are added. The choice for the basic tap lengths

(20 taps) of the main channel can be found in Figure 3.20 in Chapter 3 which quantifies the EVM performance when increasing the taps length from 0. Figure 5.9 illustrates that the EVM performance of pre-equalisers with only 20 main channel taps is ~ 6.7 (0 additional taps). For the pre-CONV-EQ the additional taps are added on the main channel, while for the pre-CAP-EQ taps are added on the crosstalk channel. The post-equaliser sections for both cases are assumed to be the same and consists of the modified DFE CAP structure presented in Figure 5.5. For each pre-equaliser type and length, the error vector magnitude (EVM) of the recovered symbols at the receiver is calculated (Figure 5.9).

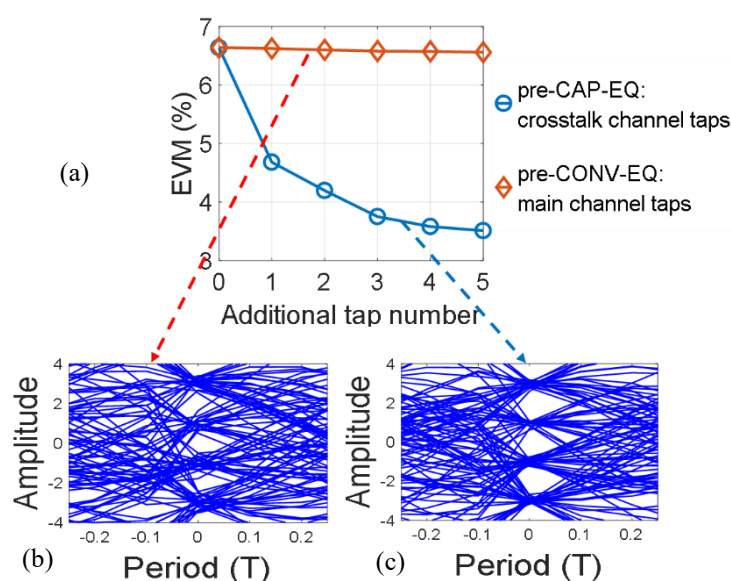


Figure 5.9(a) Calculated EVM as a function of the additional number of taps for the two types of pre-equalisers for 112 Gb/s data transmission over 100 m OM4 MMF and recovered eye diagrams at the receiver on the I-channel after equalisation using: (b) the pre-CONV-EQ and (c) pre-CAP-EQ equaliser for a total number of taps of 25 (5 additional taps)

It is clearly shown that for the pre-CONV-EQ, the use of additional FFE taps on the main channel does not introduce any further suppression of the ISI in the link with a constant EVM of $\sim 6.7\%$ obtained. On the contrary, adding taps on the crosstalk channel and forming the proposed CAP pre-equaliser results in a significant performance improvement with a reduction of the EVM down to 3.4% . Figure 5.9(b) and (c) show that the eye diagrams at the receiver for the I-channel after equalisation for the longest conventional pre-equaliser (pre-CONV-EQ with 25 main channel taps) and CAP pre-equaliser (pre-CAP-

EQ, 20 taps on the main channel and 5 taps on the crosstalk channel). The proposed pre-CAP-EQ equaliser yields a much clearer eye diagram. Figure 5.10 shows the BER performance of the link when the pre-CAP-EQ and the post-CAP-EQ is employed. The pre-CAP-equaliser achieves a receiver sensitivity of a -4.2 dBm at the hard decision forward error correction (HD-FEC) BER threshold of 3.8×10^{-3} which 2 dB better than that achieved with the post-CAP-equaliser. This improvement is due to the absence of the noise enhancement power penalty for the pre-equalisation scheme and better recovered constellation diagrams.

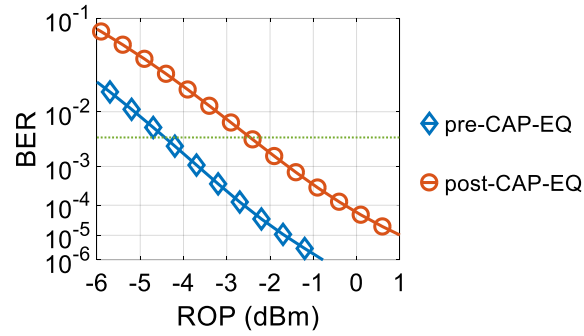


Figure 5.10: BER comparison of pre- and post-CAP-EQ at 112 Gb/s over 100 m OM4 fibre (ROP: received optical power).

5.4. Experimental Results

Due to a current limitation in a suitable signal source to generate a high quality high-speed CAP signal, data transmission experiments over 100 m OM4 MMF using an 850 nm MM VCSEL were carried out at 56 Gb/s (symbol rate of 14 Gbaud). The schematic of experimental setup was shown in Figure 5.11. At the transmitter end, a 50 GS/s arbitrary waveform generator (AWG, Tektronics 70000A) with a 15 GHz analogue bandwidth was used to generate the high-speed modulating signal. If the post-equalisation method was employed, noise enhancement introduced by the equaliser was also considered.

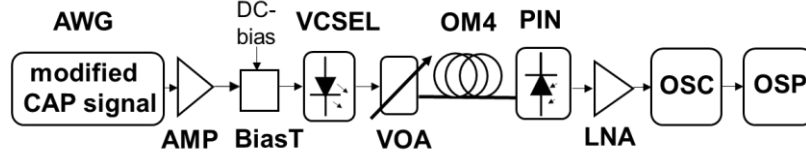


Figure 5.11: Experiment setup used in the data transmission tests (AWG: arbitrary waveform generator, AMP: electrical amplifier, VOA: variable optical attenuator, OSC: real-time oscilloscope, OSP: offline signal processing)

Figure 5.12 shows the obtained eye diagram at the receiver on the I-channel after equalisation for the 56 Gb/s CAP-16 100 m OM4 MMF link and the different types of equaliser studied (a) post-CONV-EQ, (b) post-CAP-EQ and (c) pre-CAP-EQ. The total tap length for all equalisers is 46 taps. The post-CONV-EQ features 23 FFE and 23 DFE taps on each channel while the post-CAP-EQ and pre-CAP-EQ have 18 FFE and 18 DFE taps for the main channel and 5 FFE and 5 DFE taps for the crosstalk channel. It should be noted that noises are not included in eye diagrams. The post- and pre-CAP-EQ both yield good quality of eye diagrams which are much better than that the post-CONV-EQ. which shows large residual ISI and CCI.

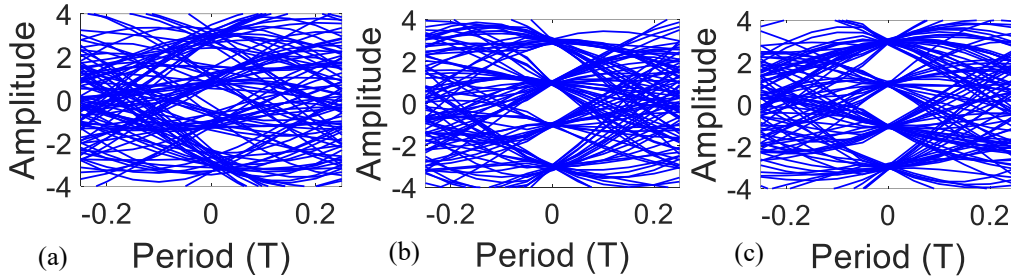


Figure 5.12: Experimental I- channel eye diagram at 56 Gb/s over 100 m OM4 fibre based on (a) post-CONV-EQ and (b) post-CAP-EQ and (c) pre-CAP-EQ.

Figure 5.13 shows the experimental BER performance of the link for the three types of equalisers as well as the respective simulated curves using the link model presented in section III for the 56 Gb/s data transmission. Good agreement is achieved between the simulation and experimental results. The conventional post-equaliser yields the worst performance with a receiver sensitivity of -3 dBm while the

pre-CAP-EQ achieves the best, with a sensitivity of -6.2 dBm. The obtained sensitivity is 0.7 dB better than that obtained for post-CAP-EQ. This smaller improvement obtained with the use of the pre-equaliser at 56 Gb/s when compared to the 2 dB improvement expected at 112 Gb/s via the simulation studies is due to the lower symbol rate which results in lower ISI and CCI in the link and therefore a lower noise enhancement power penalty for the post-equalisation scheme. The good agreement between simulation and experimental results obtained at 56 Gb/s strengthens the simulation results obtained at the higher data rate of 112 Gb/s and we hope to experimentally demonstrate this in the near future.

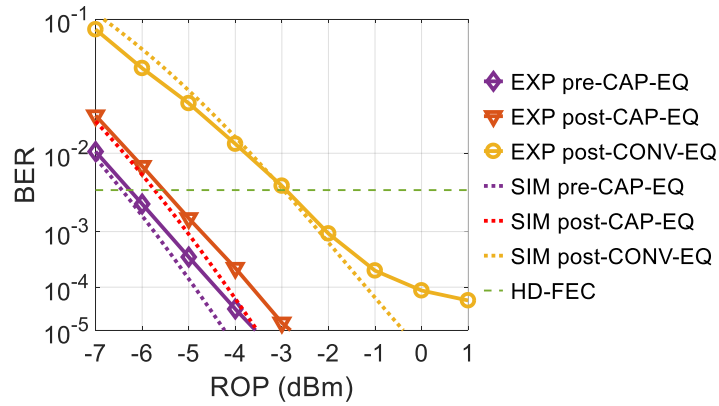


Figure 5.13: Experimental and Simulated BER comparison at 56 Gb/s over 100 m OM4 MMF for the different types of equalisation schemes: post-conv-EQ, pre-CAP-EQ and post-CAP-EQ (EXP: experimental, SIM: simulated).

5.5. Conclusion

A novel type of pre-equaliser named pre-CAP-equaliser is proposed for the first time for use in short-reach optical links employing CAP modulation scheme. The proposed equaliser uses the symbols transmitted on both channel symbols to pre-equalize the transmitted waveforms and mitigate cross channel interference due to the nonlinear phase response of the link. It is shown via simulation studies and data transmission experiments on a VCSEL-based 100 m OM4 MMF link that the proposed pre-equalisation scheme outperforms both pre-equalisation method using a conventional FFE equaliser and the corresponding post-equalisation scheme using a similar CAP equaliser. The data transmission experiments at 56 Gb/s demonstrate a 0.7 improvement in receiver sensitivity respectively over the

corresponding CAP-based post-equalisation scheme. Simulation studies indicate that a larger sensitivity improvement of 2 dB can be achieved at 112 Gb/s using the proposed scheme owing to the efficient suppression of the noise enhancement power penalty. The proposed CAP equalisers pave the way for the practical implementation of single-lane 100 Gb/s short-reach optical links using MM VCSELs and OM4 MMF.

CHAPTER

6

ARTIFICIAL NEURAL NETWORK BASED

EQUALISERS

A novel artificial neural network for CAP-based data transmission is proposed in short-reach MMF links in order to further mitigate its nonlinear impairment. The performances of different equalisers and modulations are compared both in simulation and experiment for a link at 112 Gb/s. A receiver sensitivity improvement of 2.4 dB is achieved in comparison with the CAP equaliser.

6.1. Artificial Neural Network

6.1.1. Introduction

During the past few years, ANNs have been explored to improve the performance of optical links. In [149], 50 Gb/s IMDD PAM-4 transmission was achieved over 25 km SSMF using 10 GHz optics. In [145], an 84-Gbaud PAM-4 system was demonstrated over 1.5 km SSMF proving up to 10x BER improvement over FFE. Single side band PAM-4 transmission of 112 Gb/s was also been demonstrated over 80 km SSMF, which reduces the BER by a factor of 10 in comparison with the Volterra equaliser under the threshold of 3.8×10^{-3} [150]. Demonstration of an ANN based nonlinear equaliser at 80 Gb/s CO-OFDM with QAM-16 revealed a threefold Q factor improvement after 1000-km transmission and 1 dB with respect to the linear equalisation and Volterra equaliser [151]. In addition, ANNs have also been employed to compensate for other nonlinear issues in optical links. Intra- and inter-channel nonlinearity compensation in WDM coherent optical OFDM based on ANN nonlinear equalisation was experimentally reported with the middle 20-Gb/s channel outperforming Volterra-based equalisation by ~ 2 dB in Q-factor [152]. Moreover, ANNs have been experimentally demonstrated for estimation of in-band optical signal to noise ratio (OSNR), and also for modulation format classification [153]. However, for CAP modulation based optical links, there are no reports of an ANN equaliser being used. This Chapter first proposes the use of a novel artificial neural network (ANN) in conjunction with the CAP equaliser structure to further improve the performance of FFE and DFE equalisers based on short-reach MMF links. The combination of the ANN and CAP equaliser can efficiently compensate for the non-linear impairments of both the electrical and optical components in the link. We experimentally demonstrate that 112 Gb/s CAP-based data transmission can be achieved over 100 m of OM4 MMF with a receiver sensitivity of -4.4 dBm for a BER within HD-FEC, which is an improvement of at least 2.5 dB over other such links based on different modulation schemes [154, 155].

6.1.2. Structure of CAP ANN equaliser

Figure 6.1 illustrates the structure of an ANN equaliser consisting of n taps FFE and m taps DFE. This low complexity ANN equaliser consists of one input layer, one hidden layer, and one output layer. The

function (\cdot) in the hidden layer represents the nonlinear activation function. The coefficients p_i in the hidden layer and p_0 in the output layer provide suitable bias coefficients. Assuming there are k nodes in the hidden layer, there are $(n+m)*k$ coefficients for \mathbf{W} and k coefficients for \mathbf{V} . This Chapter proposes an ANN combined with a CAP equaliser structure in order to solve the crosstalk issues. This means that $x[k]$ and $\hat{r}[k]$ for each I/Q channel include symbols from both the I- and Q- channels, which is similar to the CAP equaliser.

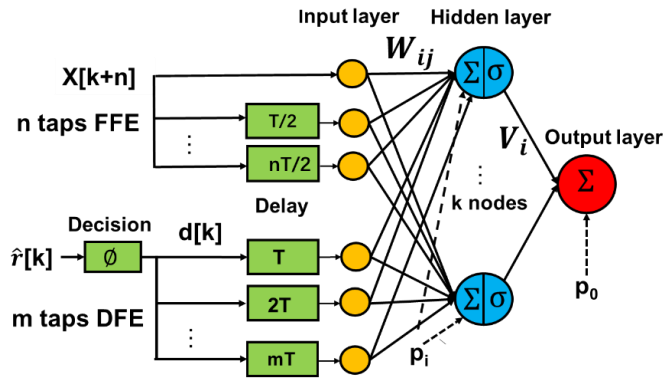


Figure 6.1: Structure of ANN

The mathematic expression for this ANN is expressed in 6-1:

$$y[k] = p_0 + \sum_{i=0}^c V_i \sigma(p_i + \sum_{j=0}^n x[k+n-j] W_{ij} + \sum_{q=1}^m d[k-q] W_{iq}) \quad 6-1$$

where $x[k]$ represents the received input symbols, $d[k]$ are the symbols decision from the DFE, \mathbf{V} and \mathbf{W} are ANN coefficients, and p_i and p_0 are the bias coefficients. The nonlinear behaviour is suppressed by including an activation function (\cdot) as shown in 6-2.

$$\sigma(x) = \frac{1}{1 + e^{-x}} \quad 6-2$$

The least mean square (LMS) algorithm is used for the training process. The cost function for an ANN at the k -th iteration can be expressed as 6-3:

$$J(\mathbf{w}) = [d(k) - h_w(x(k))]^2 \quad 6-3$$

where $x(k)$ are the input symbols, $d(k)$ are the symbols decisions, and $h_w(\cdot)$ is the ANN equaliser. The gradient descent method is used to minimize the cost function. With regards to the partial derivative term

for an ANN, a back-propagation algorithm is applied, which can be found in [156]. The coefficients $\mathbf{w}(n)$ for the input layer and coefficient $\mathbf{v}(n)$ for the hidden layer can be found according to 6-4 and 6-5.

$$\mathbf{w}(n+1) = \mathbf{w}(n) - \mu_1 \frac{\partial J(\mathbf{w})}{\partial \mathbf{w}(n)} \quad 6-4$$

$$\mathbf{v}(n+1) = \mathbf{v}(n) - \mu_2 \frac{\partial J(\mathbf{w})}{\partial \mathbf{v}(n)} \quad 6-5$$

where μ_1 and μ_2 are the updating coefficients.

6.1.3. Noise

Similar to the conventional and CAP equaliser, an ANN also introduces noise enhancement into the system. As an ANN equaliser is a nonlinear equaliser, the noise enhancement introduced by the ANN equaliser is not same as the conventional FFE and DFE equaliser. A new standard deviation of the noise after the ANN equaliser is illustrated in Figure 6.2 and it can be expressed in 6-6. The measured standard deviation value of the noise σ_1 is used to generate a matrix of noise values in Matlab and added to the received symbols, which is then demodulated and pass through the ANN equaliser. The output $x_1[n]$ includes both the recovered symbols and amplified noise. $x_2[n]$ is generated by demodulated the received symbols and pass through the ANN equaliser without adding the noise. The new standard deviation of the noise is the root-mean-square (RMS) value of the matrix calculated by subtracted $x_2[n]$ from $x_1[n]$, shown in the equation 6-5. The new standard of the σ_{new} is then used to estimate the BER performance.

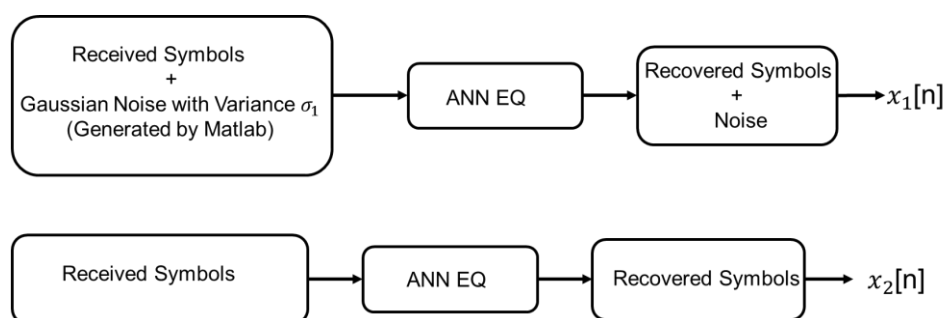


Figure 6.2: Schematic of the method for calculating the noise after the ANN equaliser (EQ: equaliser)

$$\sigma_{new} = \sqrt{\frac{\sum_{n=1}^N (x_1[n] - x_2[n])^2}{N}}$$

6-6

6.1.4. Simulation results

Figure 6.3 shows the schematic of the link model used, the main parameters for each of the link components is same as Chapter 3. The training pattern and testing pattern was same as Chapter 3 based on the PRBS-11 pattern. In the simulation, the ANN had 4 nodes in the hidden layer with 25 FFE taps and 25 DFE taps (20 taps from the main channel and 5 taps from the crosstalk channel).

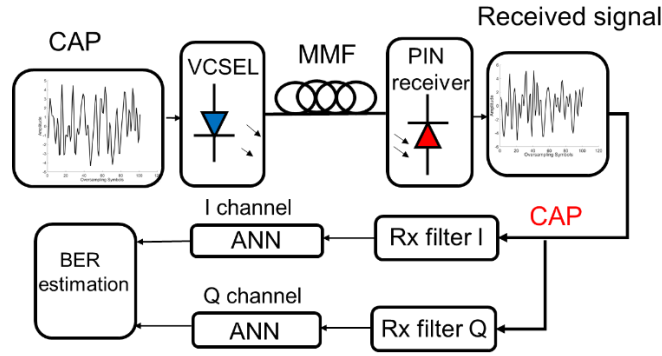


Figure 6.3: Link model used

Figure 6.4 illustrates the recovered symbols at 112 Gb/s over a 100 m OM4 fibre. It can be clearly seen that the conventional equaliser fails to recover the symbols while both the CAP and ANN equalisers successfully recover them. The ANN had the clearest constellation diagrams among three equalisers. The BER performance of the CAP and ANN equalisers with CAP-16 and also DMT is shown in Figure 6.5. The BER plot of the conventional equaliser does not appear as it fails to recover the symbols. The receiver sensitivity to achieve a HD-FEC limit for the DMT, CAP equaliser and ANN equaliser based CAP-16 was -0.7 dBm, -2.4 dBm, and -4.7 dBm, respectively.

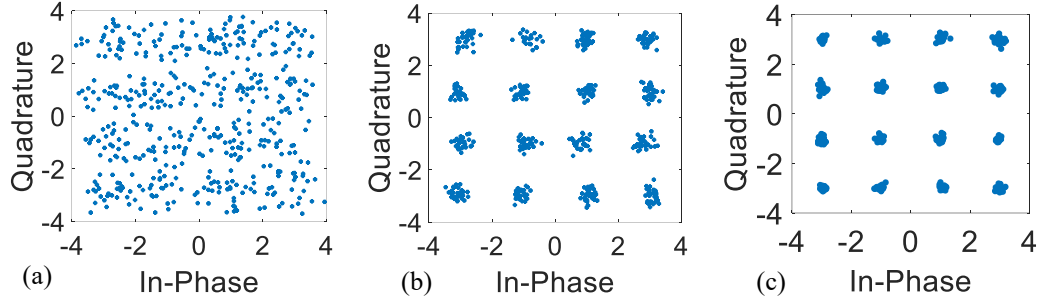


Figure 6.4: Recovered constellation diagrams at 112 Gb/s over a 100 m OM4 fibre: (a) conventional equaliser, (b) CAP equaliser and (c) ANN equaliser

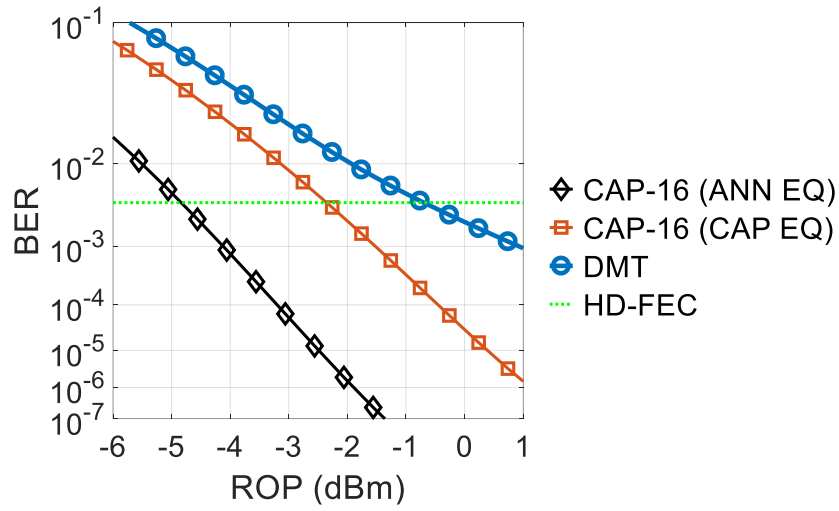


Figure 6.5: BER performance of CAP-16 based on ANN and CAP equalisers and DMT at 112 Gb/s over a 100 m OM4 fibre

6.1.5. Experimental results

The experimental setup was the same as that used in Chapter 3, and is shown in Figure 6.6. The offline signal processing included demodulation, ANN equalisation, and BER estimation. For the data transmission tests presented here, the CAP equaliser comprised 22-taps FFE and 22-taps DFE on the main channel, and 5-taps FFE and 5-taps DFE taps on the other (crosstalk) channel. The experimental recovered constellation diagram is illustrated in Figure 6.7 at 112 Gb/s over a 100 m OM4 fibre. The ANN and CAP equalisers successfully recovered signals while the conventional equaliser failed. It can be clearly seen that the ANN equaliser had the best performance among the three equalisers.

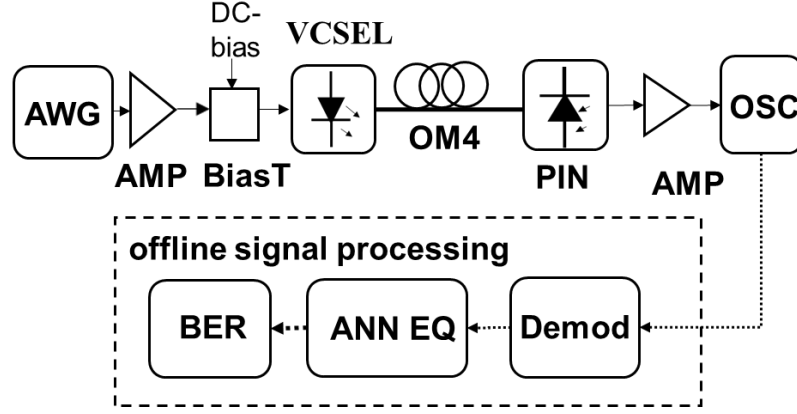


Figure 6.6: Experimental Setup (AWG: arbitrary waveform generator, OSC: oscilloscope, Demod: demodulation, EQ: equaliser)

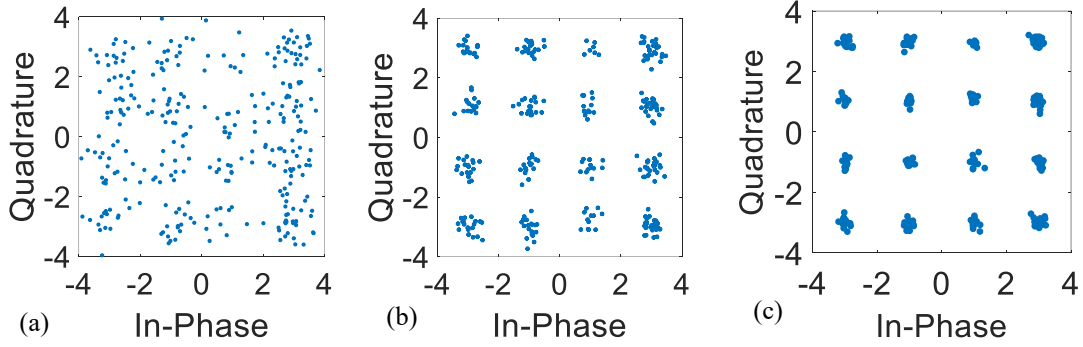


Figure 6.7: Constellation diagrams at 112 Gb/s over 100 m OM4 fibre: (a) conventional equaliser, (b) CAP equaliser and (c) ANN equaliser.

Both the experimental and simulated BER performances of CAP-16 based conventional, CAP and ANN equaliser, and DMT scheme are shown in Figure 6.8. The receiver sensitivity for the CAP-16 based ANN equaliser, CAP equaliser and DMT scheme was -4.4 dBm, -2 dBm, and 0 dBm, respectively. The conventional equaliser BER is not plotted as the received symbols were not recovered successfully. The experimental results matched well with the simulated results with a difference of < 0.5 dB. As discussed in the previous Chapters, the simulation model does not include all nonlinear effects which may be existed in the experiment, the simulation result is slightly better than the experimental result. However, the models are sufficient to demonstrate the principle and performance of this novel equaliser.

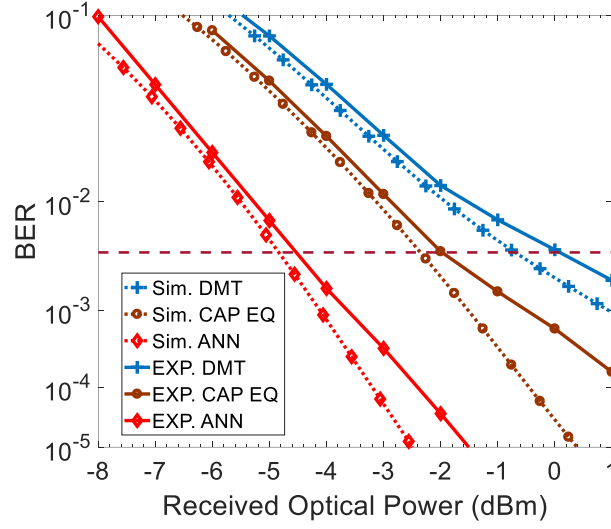


Figure 6.8: BER performance of two equalisers based on CAP-16 scheme and DMT scheme at 112 Gb/s over a 100 m OM4 fibre.

6.1.6. Conclusion

We proposed the use of a novel artificial neural network for CAP-based data transmission in short-reach MMF links in order to further mitigate its nonlinear impairment. The performance of different equalisers and modulations was compared both in simulation and experiment for a link at 112 Gb/s. A receiver sensitivity improvement of 2.4 dB was achieved in comparison with the CAP equaliser.

CHAPTER

7

OPTICAL EQUALISERS

A monolithically integrated silicon optical equaliser for 50 Gb/s data transmission based on the NRZ scheme after 10 km standard single mode fibre (SSMF) is demonstrated. A significant eye quality improvement at the receiver side can be clearly seen compared to the scenarios without using this optical equaliser.

7.1. Silicon optical equaliser

7.1.1. Introduction

Equalisation is a simple yet effective approach used to suppress distortion in optical links. Equalisation can be carried out in either the electrical or in the optical domain. However, the drawback of the DSP approach is that a more complex receiver structure is needed, which may increase costs and energy consumption. Also, in an optical communication system, the electrical method used can increase the loss of the optical phase and polarization information of the signal as it is used after the square law optical detection. In contrast, optical equalisers are implemented directly in the optical channel retaining full optical phase, amplitude and polarization information and so can more effectively compensate for signal distortion. Optical equalisers have attracted much research interest. An explicit optical FFE model to investigate the practical performance improvement of bandwidth-limited transmitters and fibre links was developed recently in [157]. Optical equalisation has enabled optical equalized systems to operate at data rates above 100 Gb/s [158]. Furthermore, it can be operated simultaneously on multiple WDM channels, which makes the optical FFE more power efficient than per wavelength electrical channel FFEs. Optical equaliser structures with variable coefficients can be based on cascaded Mach-Zehnder interferometers (MZI), ring resonators, or etalons. Various tunable optical equalisers were demonstrated using silica/polymer PLCs [159, 160] and InP PICs [161] with stable high-performance in passive and active devices, respectively, but suffer from bulky size. Silicon photonics can offer both active and passive optical components on a single chip with both compact sizes and low-power consumption. The use of mature COMS microelectronics fabrication infrastructure promises large-scale silicon PICs with low cost but high yield. Optical components such as modulators, variable optical attenuators and wavelength-division multiplexing (WDM) filters have been monolithically integrated on silicon chips. Recently, silicon equalisers integrated with In-Phase/Quadrature Modulation for coherent transmission have been reported [162]. Here we demonstrate the compact silicon optical equaliser different from the design concept shown in [162, 163], the ultracompact monolithic integration of an optical equaliser for a 50-Gbaud IM/DD system, to show the powerful capability for the integration of new functions into silicon photonics. This optical equaliser area is less than $2.8 \text{ mm} \times 0.65 \text{ mm}$, which is smaller than the previous demonstrated PLCs ($2.6 \text{ cm} \times 2 \text{ cm}$) [163], InP ($8.5 \text{ mm} \times 3.5 \text{ mm}$) [161] and has a comparable size with

silicon optical equalisation filters [162].

7.1.2. Design and experimental setup

We used a simpler design concept compared to that in [162], using variable optical attenuators (VOAs) which is built by forward biased PN junctions to implement several parallel filter structures. Figure 7.1 illustrates the design of this optical equaliser. In the actual design, two 2x2 3 dB multimode interferometer (MMI) couplers implement the function of a 1x3 interferometer due to lack of qualified 1x3 building block and the power was split by 1:1:2 for the pre-, post- and main tap cursor, respectively. Each VOA had its own set of coefficients which were adjusted independently where the input signals were split and passed through different waveguide time delays. The multimode interference was combined with different waveguide time delays. The output signals were combined using multimode interference (MMI) combiners. The tap coefficients could be set by appropriate adjustment of the electrical control signals of the VOA and phase shifter (PS) sections. Figure 7.2 shows the micro image of the fabricated on-chip optical equaliser. This design was fabricated at IMEC in a multi-project wafer (MPW) for silicon photonics. The silicon-on-insulator (SOI) wafer had a 220 nm thick top silicon layer and a 2 μm thick buried-oxide layer.

In this design, three taps of FFE with half baud tap spacing were adopted since all FFE based optical equalisers are in practice only able to support a few taps. This integrated equaliser used the design concept analyzed in our previous work [157] with three VOAs and was designed for TE mode only with fully etched apodised grating couplers used as input and output ports.

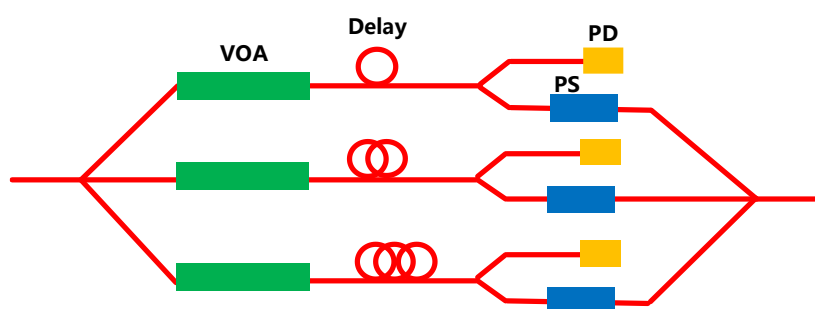


Figure 7.1: Principle of the optical equaliser

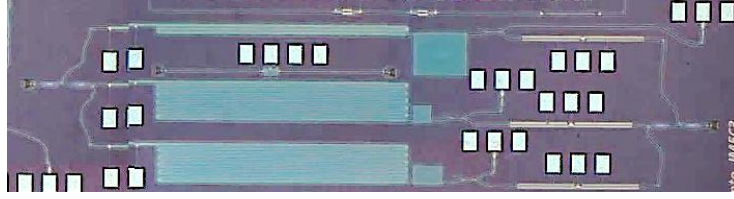


Figure 7.2: Image of this on-chip optical equaliser.

The light coupled into the optical equaliser was split by three multimode interferometer [MMI] couplers. The relative delay between the three arms of the VOA was designed to be 10 ps account to the half baud rate of 50GB/s achieved by introducing a waveguide length difference of 0.7 mm with the assumption that the group index is 4.24.

The total insertion loss of the coupling from the grating to fibre was about 11 dB for both sides with a 14 dB grating coupling loss and a 8 dB chip loss. All three taps were fabricated with forward biased PN junctions to tune the amplitude and phase, respectively. The total optical equaliser size was 1×1.5 mm. The working principle of this simple three-tap optical equaliser was explained in [53] and is summarized here. An optical signal propagating through three parallel VOAs experiences three different time delays, with the combination of the upper/down arms of two VOAs, resulting in three relative time delays, $-T/2$, 0, and $T/2$. Therefore, the impulse response consists of a main one at time 0, with two small impulses at times $-T/2$, 0, and $T/2$. The amplitude of these three impulses can be controlled by the VOA and the phase difference can be controlled by the phase shifter. These two pre- and post- cursor components can remove the power from the previous bit and the following bit, thereby cancelling the ISI. By removing the ISI using an optical equaliser, the modulation bandwidth can be boosted.

Figure 7.3 shows the experimental setup in order to characterize our on-chip optical equaliser. A continuous light with wavelength 1560 nm was emitted from the tunable laser diode. The light was modulated by the Mach-Zehnder modulator (MZM) which was driven by a pattern generator of 40 Gb or 50 Gb PRBS signals. Due to the polarization sensitivity, the polarization controller (PC) was placed before the MZM. A VOA was placed after the MZM for the optical power adjustment into the on-chip optical equaliser. A 10 km standard single mode fibre (SSMF) was used, and then the signal was fed into the on-chip optical equaliser. In this experiment, two vertical grating couplers were used to couple the light from the fibre to the silicon waveguide and the output signal from the waveguide to the fibre. Another polarization controller (PC) was placed before the VOA. The electrodes of the VOAs, PDs and

PS were contacted by a probe pin array spaced with 250 μm . Variable voltages generated from independent power supplies were applied to different pins in the array. The transmitted output temporal waveform was detected by a 50 GHz DWDM Finisar Single high-speed photo detector (XPDV2120R) and recorded by the Agilent wide-band oscilloscope (86100A).

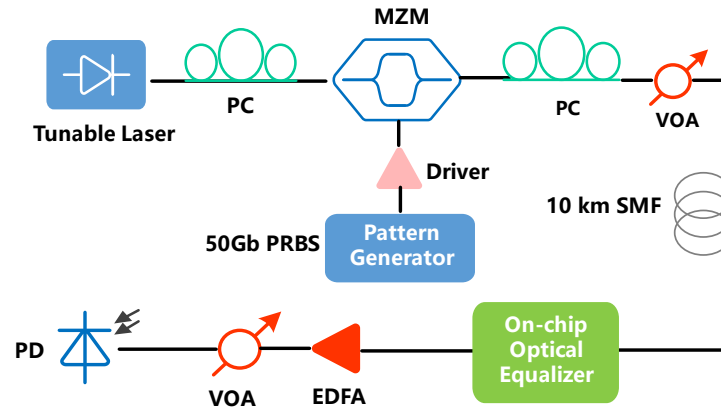


Figure 7.3: Experimental setup to characterize the optical equaliser

7.1.3 Experimental Results

As measured in IMEC MPW, the VOA was composed of forward biased PN junctions with a tuning rate of 30 dB/17 mm. Therefore, here the three VOA lengths were designed to be 11.2 mm, 11.2 mm and 3.2 mm for the pre-, post- and main cursors. The measured VOAs for all three taps against different bias voltages are shown in Figure 7.4. It can be clearly seen that the maximum attenuation was about 9 dB at 1 V, but we didn't go further to avoid blowing up the PN junction.

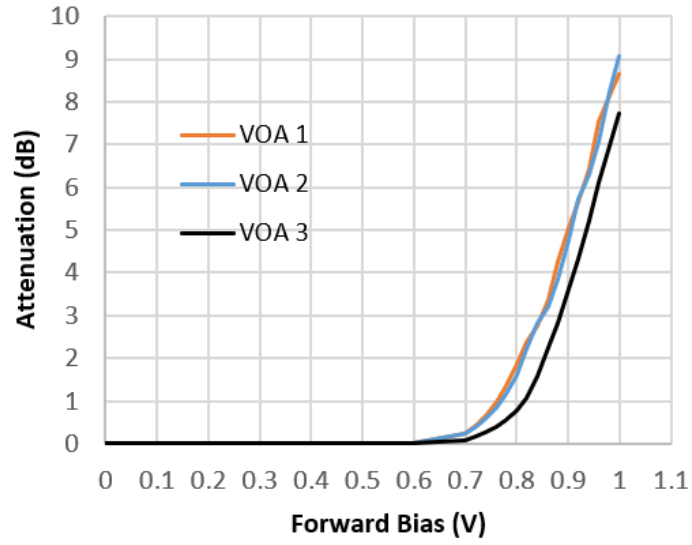


Figure 7.4: VOAs (three taps) against their applied voltages

The impulse response of the optical equaliser was characterized by feeding the ultrashort optical pulses into the chip, shown in Figure 7.5. The normalized three pulse response with pre- and post- cursor amplitude was half of the main cursor, conforming to the design with two cascaded MMI. However, the time delay between three taps was 7 ps and 14 ps, respectively, which was not in accordance with the design of 10 ps each. One reason for this could be fabrication issues, and another could be miscalculation of the refractive index of the PN junction and passive waveguide of the main cursor.

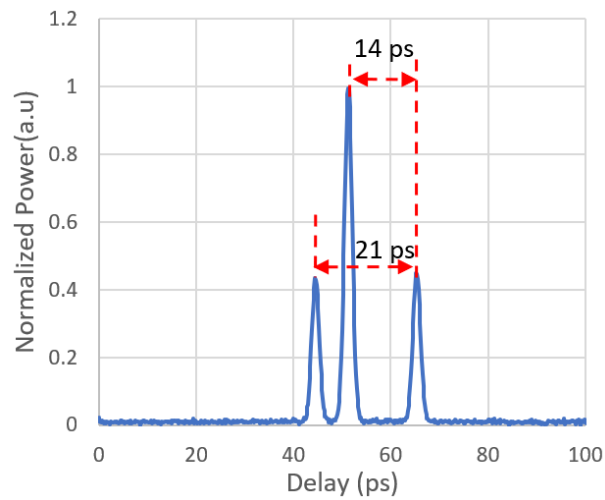


Figure 7.5: Delays of impulse responses (three taps)

The transmitter pattern was based on Pseudorandom bit stream (PRBS) NRZ data with a length of $2^{16}-1$. The data was modulated at 40 Gb/s and 50 Gb/s, respectively, on the light from an external cavity laser at 1560 nm employing a dual-drive LiNbO Mach-Zehnder modulator. By adjusting the voltage on the three VOAs and also the phase shifter, the performance of this optical equaliser is explored in Figure 7.6 by measuring the eye diagrams after the 10 km SSMF with and without equaliser. The back-to-back (B2B) eye diagram was measured as the reference. At the received optical power of -10.8 dBm, the eye clearly opened and was error free compared to the scenarios without an optical equaliser at both 40 Gb/s and 50 Gb/s data transmissions.

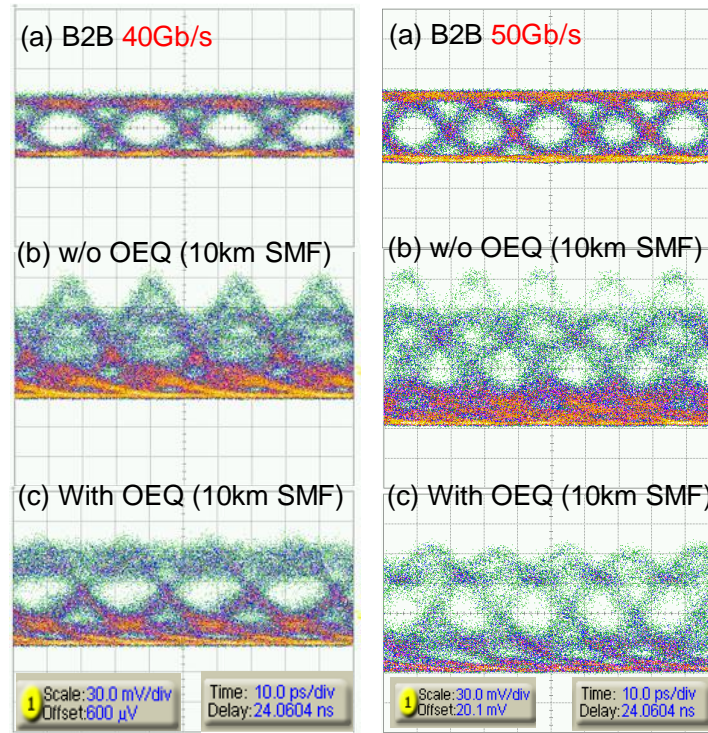


Figure 7.6: Eye diagrams at B2B and after 10 km without and with the optical equaliser.

7.1.4. Conclusion

Here we demonstrated a monolithically integrated silicon optical equaliser for 50 Gb/s data transmission based on the NRZ scheme. This silicon optical equaliser has three taps with half symbol spacing designed based on three VOAs and phase shifters which can be used to appropriately adjust the tap coefficients. Eye diagrams were measured after 10-km SSMF using a tunable laser diode at a wavelength of 1560 nm.

In order to demonstrate the performance of the equalisers, eye diagrams were shown clearly open with error free transmission using this optical equaliser after 10 km SSF, at both 40 Gb/s and 50 Gb/s data transmissions.

CHAPTER

8

FUTURE WORK

This chapter proposed the potential future developments for the system performances enhancement.

8.1. Future work

8.1.1. Parallel transmission

8.1.1.1. 4×100 Gb/s VCSEL based OM4 link

400 Gb/s optical links have been targeted as the next generation of short-reach communication links inside data centres. This target can be achieved with different configurations such as deploying 16 lane each operating at 25 Gb/s or 8 lanes at 50 Gb/s. However, such multi-lane configurations impose stringent requirements in terms of the footprint, power consumption and number of active and passive components in the link. A single lane 112 Gb/s data transmission has been demonstrated. 4×100 Gb/s multi-channel transmission can be achieved using $4 \times$ OM4 bundle and 2×2 VCSELs array structure (Figure 8.1). Short wavelength division multiplexing between 850 nm and 1000 nm [164] can also be used to demonstrate 400 Gb/s data transmission by using four wavelengths, as shown in Figure 8.2.

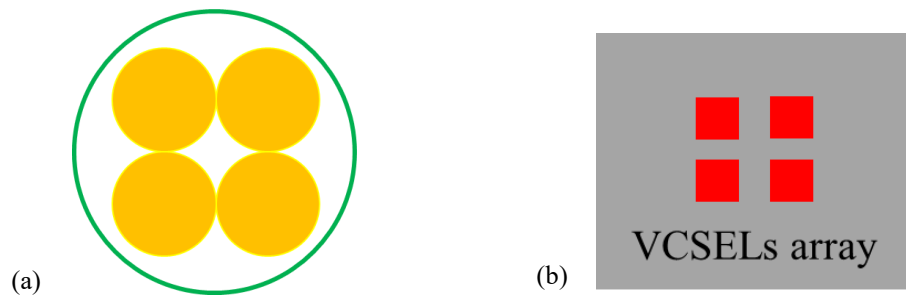


Figure 8.1: 400 Gb/s optical transmission: (a) OM4 bundle and (b) 2×2 VCSELs array

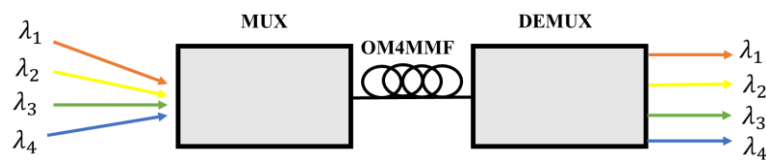


Figure 8.2: 400 Gb/s over a single OM4 fibre achieved by SWDM technique

8.1.1.2. Toward 100 Gb/s POF link

The POF links investigated here are based on a single commercial LED transmitter. Recently, the

development of Gallium Nitride devices has enabled the fabrication of energy efficient LEDs in array structures, which provides a perfect platform for parallel optics applications. As illustrated in Figure 8.3, this multi-POF bundle cable has a diameter of 4.2 mm which is comparable to a coaxial copper cable. The μ LED arrays can be designed with a pixel-to-pixel distance of 1 mm and arranged in a hexagonal shape. According to the results shown in this dissertation, total data rate can be up to 35 Gb/s if each of channels is operating at 5 Gb/s, which has already been demonstrated over 10 m POF. WDM is also a promising technology to further improve the capacity link. By deploying small dimension μ LEDs with different wavelengths such as 410 nm (violet), 450 (blue) and 520 (green) for each POF, a total data rate >100 Gb/s can be expected (Figure 8.3(b)).

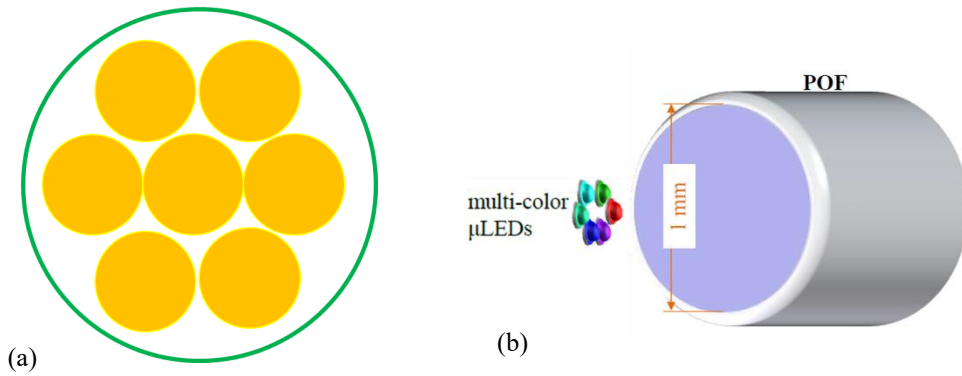


Figure 8.3:(a) Hexagonal SI-POF bundle for parallel transmission, (b) WDM-POF link.

8.1.2. Artificial neural network based pre-equalisation scheme

Chapter 5 has presented a novel pre-CAP-equaliser, providing a 2 dB improvement in receiver sensitivity compared to the post-CAP-equaliser. Chapter 6 demonstrates a novel artificial neural network (ANN) equaliser to further suppress the nonlinear behavior of the link. Therefore, a novel ANN based pre-equaliser scheme can be proposed to further improve the link performance including the MMF fibre and POF link by simultaneously suppressing the noise enhancement factor and also nonlinear effects (Figure 8.4). In [165], a Volterra filter based pre-equalisation scheme is used for the VCSEL based link using DMT scheme. 135 Gb/s over 300 m OM4 fibre is reported at the soft-decision feedforward error correction limit. It can be expected this novel ANN based pre-equalisation with CAP scheme should outperformance results in [165].

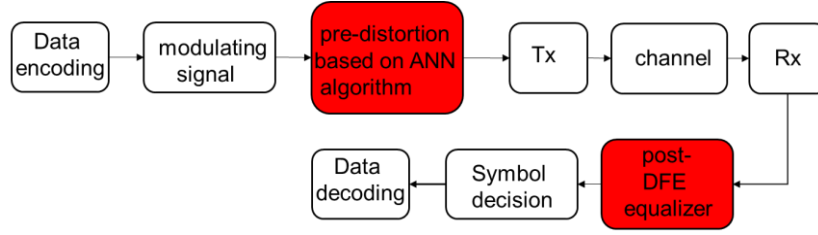


Figure 8. 4: Schematic of the link with pre-distortion based on ANN algorithm.

8.1.3. CAP modulation based other optical communication links

In the work here, OM4 based and POF based links have been investigated based on CAP modulation using both conventional equaliser and CAP equaliser. As a promising modulation scheme, CAP can also be employed in other types of optical communication systems such as standard single mode fibre (SSMF) based link or wireless visible light communication link. Similar work can be investigated using CAP equaliser to improve the performance of links. Although the SSMF has smaller dispersion than the MMF, the long-distance transmission over SSMF still generates large dispersion which degrades the system performance. Moreover, nonlinear behaviors can also be found in SSMF system [149, 150]. For the wireless communication visible light communication link, the dispersive wireless channel has been explored in [145]. It can be expected that CAP equaliser can also be used to improve the capacities of both two links by solving the crosstalk between I- and Q- channel.

CHAPTER

9

CONCLUSIONS

This chapter concludes this dissertation. The major achievements in the development of high speed multimode fibre links are summarized and limitations are also described.

9.1. Conclusion

Owing to the rising demand for the inside data centres, short-range optical data communication is concentrated on improving the link capacity. Multimode glass fibre based links maintain their popularity for high data rate short distance applications such as in-building networks with the distance typically less than 500 m. Meanwhile, plastic optical fibres have also attracted much research interest for even shorter links such as home networks and in-car networks. The development of the bandwidth hungry services such as high-definition TV, video streaming/monitoring and cloud computing pushes the data rate beyond 1 Gb/s. However, for both multimode glass and plastic optical fibres based links, the link performance is mainly limited by the low bandwidth. Therefore, advanced modulation scheme in conjunction with novel equalisation techniques is proposed to enhance the achievable data rates over both links. Chapter 1 has reviewed principles of various modulation schemes including pulse amplitude modulation (PAM), carrierless amplitude and phase modulation (CAP) and discrete multitone scheme (DMT).

Chapter 2 has reviewed the fundamentals of both MMF and LED based links. In particular, the mechanisms and characteristics of the fundamental building blocks including the MMF/POF channel, transmitters such as VCSELs and LEDs, and also receivers (PIN/APD) have been reviewed. As the 40G/100G Ethernet standard has been published, the OM4 fibre has been considered the cost-effective solution for updating the existing fibre bases owing to its larger bandwidth. SI-POF is of particular interests owing to its-low cost and matches well with μ LEDs. OM4 fibre and SI-POF is therefore has been used in the work here. In addition, the noise performance of PIN and APD has also been explored.

The VCSEL based OM4 fibre link has been investigated in Chapter 3 based on CAP-16 modulation using a novel CAP equaliser. As a promising modulation scheme, CAP modulation has been widely used in optical communication links. However, CAP modulation suffers from the crosstalk issues between I- and Q- channel which significantly degrades the system performance. In the work here, we firstly proposed this novel type of equaliser to solve crosstalk issues between I- and Q- channel while the conventional feed-forward and decision-feedback equaliser can not combat with. This novel CAP equaliser utilizes received symbols on both I- and Q- channel to recover each of them. 112 Gb/s CAP-16 data transmission has been achieved over 100 m OM4 fibre within hard decision feedforward error correction limit. Both simulation and experiment studies have been detailed investigated. The performance of conventional equaliser, PAM and DMT scheme have also been studied. The CAP

equaliser demonstrates a 1.2 dB and 1.7 dB improvement in receiver sensitivity compared to the PAM-4 and the DMT scheme while the conventional equaliser fails to recover the received signals. The CAP equaliser has shown a significant performance improvement over the conventional equaliser with very small additional complexity.

The μ LED-POF link is also investigated using the CAP equaliser in Chapter 4, achieving 4 Gb/s over 25 m POF link and 5 Gb/s over 10 m POF. In this Chapter, an APD is used as the receiver which has been demonstrated to outperform PIN in [142]. However, conventional equaliser can only support 4 Gb/s and fails at 5 Gb/s over 10 m POF due to failure to recover the received signals. Both simulation and experiment work has demonstrated the significant performance improvement using CAP equaliser than the conventional equaliser.

In Chapter 5, a novel pre-CAP-equaliser has been proposed to solve the crosstalk issue at the transmitter side for the VCSEL based OM4 fibre link. This pre-CAP-equaliser consists of a novel FFE section at the transmitter to simultaneously suppress the ISI and CCI and also a novel DFE at the receiver side. 56 Gb/s experiment work has been demonstrated over 100 m OM4 fibre with an improvement of 0.7 dB over the post-CAP-equaliser. Simulation results have been shown that a 2 dB improvement can be obtained over the post-CAP-equaliser at 112 Gb/s over 100 m OM4 fibre.

Chapter 6 demonstrates a novel artificial neural network equaliser in conjunction with the CAP equaliser structure at 112 Gb/s over 100 m OM4 fibre. ~ 2.4 dB improvement in receiver sensitivity has been achieved compared to the CAP equaliser. In addition, a monolithically integrated silicon optical equaliser for 50 Gb/s data transmission has been demonstrated. The design of this optical equaliser includes three taps which can be adjusted by three VOAs and phase shifters. After 10 km SSMF at both 40 Gb/s and 50 Gb/s data transmissions, the error-free eye diagram recovered by this optical equaliser demonstrates a significant link performance improvement compared to that without this optical equaliser.

Several novel equalisation techniques for short-range optical links have been demonstrated in the thesis. For the further improvement of the link speed, the performance can be limited by the large noise enhancement at the receiver side resulting from the low bandwidth and also nonlinearities accumulated from the link, and therefore largely degrades the BER performance. The simulation model in the thesis does not include all nonlinearities such as the receiver nonlinearity resulted from the square law effect. This leads to the difference between the simulation results and the experimental results. It can be clearly seen that the simulation result is better than the corresponding experimental results. However, it is

sufficient to show the principle of novel equalisers and demonstrate its improved performance compared to the conventional one.

Appendix

BER estimation method

The BER of the link is calculated using the measured root-mean-square (RMS) noise values assuming Gaussian distribution. Assuming the symbols are successfully recovered, the recovered symbols are not in the ideal position due to the residual inter-symbol-interference (ISI).

For binary communication, the threshold value can be calculated in **10-1**.

$$V_{TH} = \frac{S_1 + S_2}{2} \quad \mathbf{10-1}$$

where S_1 and S_2 are ideal symbol states. For the k th recovered symbol, its corresponding ideal symbol is found first according to **10-1**. Assuming its corresponding ideal symbol is S_1 , the BER can be calculated by **10-2**.

$$BER^k = Q\left(\frac{V_{TH}-S'_k}{\sigma}\right) = \frac{1}{2} \operatorname{erfc}\left(\frac{V_{TH}-S'_k}{\sqrt{2}\sigma}\right) \quad \mathbf{10-2}$$

where S'_k is the k -th recovered symbols, σ is the root mean square (rms) value of the noise. Assuming its corresponding symbol is S_2 , the BER can be found according to **10-3**.

$$BER^k = \frac{1}{2} \operatorname{erfc}\left(\frac{S'_k - V_{TH}}{\sqrt{2}\sigma}\right) \quad \mathbf{10-3}$$

For M received symbols, the BER for this binary link is then expressed in **10-4**.

$$BER = \frac{\sum_{k=1}^M BER^k}{M}, k = 1, 2, \dots, M \quad \mathbf{10-4}$$

For multilevel encoding scheme assuming N symbol states, the BER can be estimated from the calculation of symbol error rate (SER) assuming Gray coding used (**10-5**).

$$BER \approx \frac{SER}{N} \quad \mathbf{10-5}$$

A small value of BER can be further seen equivalent to $\frac{SER}{N}$. The decision threshold is expressed in **10-6**.

$$V_{TH}^n = \frac{S_n + S_{n+1}}{2}, n = 1, 2, \dots, N - 1 \quad \mathbf{10-6}$$

For the k -th received symbol whose corresponding ideal symbol are S_1 and S_N , the symbol errors are from one neighbor symbol, which can be expressed as **10-7** and **10-8**

$$SER_1 = \frac{1}{2} \operatorname{erfc} \left(\frac{V_{TH}^1 - S_k'}{\sqrt{2}\sigma} \right) \quad \mathbf{10-7}$$

$$SER_N = \frac{1}{2} \operatorname{erfc} \left(\frac{S_k' - V_{TH}^{N-1}}{\sqrt{2}\sigma} \right) \quad \mathbf{10-8}$$

Otherwise, the symbol errors are from two neighbor symbols and can be expressed as

$$SER_n = \frac{1}{2} \operatorname{erfc} \left(\frac{S_k' - V_{TH}^{n-1}}{\sqrt{2}\sigma} \right) + \frac{1}{2} \operatorname{erfc} \left(\frac{V_{TH}^n - S_k'}{\sqrt{2}\sigma} \right), \quad n = 2, \dots, N - 1. \quad \mathbf{10-9}$$

For M recovered symbols, the SER is expressed in **10-10**.

$$SER = \frac{\sum_{k=1}^M SER^k}{M} \quad \mathbf{10-10}$$

where SER^k is the SER for the k -th recovered symbol. Therefore, the BER is deduced in **10-11**.

$$BER = \frac{\sum_{k=1}^M SER^k}{MN} \quad \mathbf{10-11}$$

Considering the noise enhancement factor, the RMS value of noises used in the BER calculation is expressed in **10-12**.

$$\sigma = F_e \sigma_m \quad \mathbf{10-12}$$

where σ_m is the measured RMS noise value and F_e is the noise enhancement factor, which has been clearly stated in Chapter 3. The BER performance is also evaluated based on the Monte Carlo method. The Gaussian noise is generated and added to the received waveform. The received waveforms with

noises are demodulated and pass through the equalizer and the BER is calculated by counting the errors, as illustrated in Figure 10.1. For 112 Gb/s data transmission over 100 m OM4 fibre, the error is counted at the received optical power of -2.4 dBm (achieving the HD-FEC threshold based on BER estimation method) for different transmitted pattern lengths. The BER of 3.8×10^{-3} corresponding to 125 errors for the pattern length of $2^{15}-1$. Table 10-1 illustrates the number of counting errors and BER based on different pattern lengths. It can be clearly shown that the result of Monte Carlo method is according with the result of the BER estimation method.

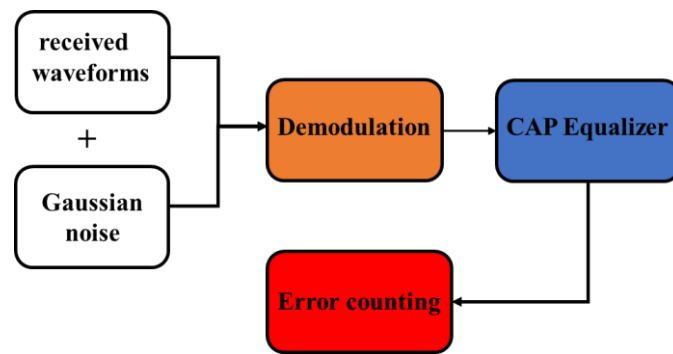


Figure 10.1: Schematic of error counting based on Monte Carlo method.

Table 10-1 Monte Carlo method for BER calculating

Pattern lengths	Number of Errors	BER
$2^{15}-1$	119	3.6×10^{-3}
$2^{16}-1$	243	3.7×10^{-3}
$2^{17}-1$	480	3.7×10^{-3}
$2^{18}-1$	1005	3.8×10^{-3}

References

- [1] A. G. Bell and S. Tainter, "Photophone transmitter," *US Pat*, vol. 235, p. 50, 1880.
- [2] A. G. Bell, "The photophone," *Science*, vol. 1, no. 11, pp. 130-134, 1880.
- [3] D. Hutt, K. Snell, and P. Belanger, "Alexander Graham Bell's Photophone," *Optics and Photonics News*, vol. 4, no. 6, pp. 20-25, 1993.
- [4] C. DeCusatis, *Handbook of fiber optic data communication: a practical guide to optical networking*. Academic Press, 2013.
- [5] D. R. Goff, "Fiber Optic Video Transmission. 1st," ed: Woburn, Massachusetts: Focal Press, 2003.
- [6] V. Alwayn, "Optical Network Design and Implementation" ciscopress. com," *United State of America*, 2004.
- [7] G. P. Agrawal, "Optical communication: its history and recent progress," in *Optics in Our Time*: Springer, Cham, 2016, pp. 177-199.
- [8] S. Blokhin *et al.*, "Oxide-confined 850 nm VCSELs operating at bit rates up to 40 Gbit/s," vol. 45, no. 10, pp. 501-503, 2009.
- [9] C. V. N. Index, "Forecast and methodology, 2014-2019 white paper," *Retrieved 23rd September*, 2015.
- [10] C. De Blok and P. Matthijsse, "Core alignment procedure for single-mode-fibre jointing," *Electronics Letters*, vol. 20, no. 3, pp. 109-110, 1984.
- [11] A. Chu and S. Hong, "Buried sol-gel/SiON waveguide structure for passive alignment to single-mode fiber on Si substrate," *IEEE Photonics Technology Letters*, vol. 19, no. 1, pp. 45-47, 2007.
- [12] J. Yamada, S. Machida, and T. Kimura, "2 Gbit/s optical transmission experiments at 1.3 μm with 44 km single-mode fibre," *Electronics Letters*, vol. 17, no. 13, pp. 479-480, 1981.
- [13] R. J. Mears, L. Reekie, I. Jauncey, and D. N. Payne, "Low-noise erbium-doped fibre amplifier operating at 1.54 μm ," *Electronics Letters*, vol. 23, no. 19, pp. 1026-1028, 1987.
- [14] S. Sugimoto *et al.*, "High-speed digital-signal transmission experiments by optical wavelength-division multiplexing," *Electronics Letters*, vol. 13, no. 22, pp. 680-682, 1977.
- [15] Y. Miyagawa, T. Yamamoto, H. Masuda, M. Abe, H. Takahashi, and H. Takara, "Over-10 000-channel 2.5 GHz-spaced ultra-dense WDM light source," *Electronics Letters*, vol. 42, no. 11, pp. 655-657, 2006.
- [16] F. E. Ross, "An overview of FDDI: The fiber distributed data interface," *IEEE Journal on Selected Areas in Communications*, vol. 7, no. 7, pp. 1043-1051, 1989.
- [17] V. Hopkin and B. Kirk, "Microelectronics communications technology producing quality products mobile and portable power emerging technologies," in *Proceedings of the Wescon Conference*, 1995, pp. 7-9.
- [18] R. N. Hall, G. E. Fenner, J. Kingsley, T. Soltys, and R. Carlson, "Coherent light emission from GaAs junctions," *Physical Review Letters*, vol. 9, no. 9, p. 366, 1962.
- [19] G. P. Agrawal and N. K. Dutta, *Semiconductor lasers*. Springer Science & Business Media, 2013.
- [20] H. Statz, C. Tang, and J. Lavine, "Spectral output of semiconductor lasers," *Journal of Applied Physics*, vol. 35, no. 9, pp. 2581-2585, 1964.

- [21] W. Gambling, D. Payne, and H. Matsumura, "Mode excitation in a multimode optical-fibre waveguide," *Electronics Letters*, vol. 9, no. 18, pp. 412-414, 1973.
- [22] A. B. W. Daum, and L. Goehlich, "Environmental qualification of polymer optical fibres for industrial applications," presented at the Plastic Optical Fibres and Applications Conference, Paris, 1992.
- [23] O. Ziemann, J. Krauser, P. E. Zamzow, and W. Daum, "POF handbook," *Springer*, 2008.
- [24] J.-M. Wun *et al.*, "GaN-based miniaturized cyan light-emitting diodes on a patterned sapphire substrate with improved fiber coupling for very high-speed plastic optical fiber communication," *IEEE Photonics Journal*, vol. 4, no. 5, pp. 1520-1529, 2012.
- [25] J. J. McKendry *et al.*, "High-speed visible light communications using individual pixels in a micro light-emitting diode array," *IEEE Photonics Technology Letters*, vol. 22, no. 18, pp. 1346-1348, 2010.
- [26] X. Li, J. Wei, N. Bamiedakis, R. Penty, and I. White, "Avalanche photodiode enhanced PAM-32 5 Gb/s LED-POF link," in *2014 The European Conference on Optical Communication (ECOC)*, 2014, pp. 1-3: IEEE.
- [27] F. W. Scholl, M. H. Coder, S. J. Anderson, and B. V. Dutt, "Applications of plastic optical fiber to local area networks," in *Fiber Optic Datacom and Computer Networks*, 1988, vol. 991, pp. 190-195: International Society for Optics and Photonics.
- [28] W. Daum, J. Krauser, P. E. Zamzow, and O. Ziemann, "Components for POF systems," in *POF—Polymer Optical Fibers for Data Communication*: Springer, 2002, pp. 95-154.
- [29] J. Bliss, *Plastic Optical Fibers and Applications*. Information Gatekeepers Inc, 1994.
- [30] M. Kitazawa, K. Shimada, N. Saito, S. Takahashi, and K. Yagi, "Mechanical and optical performance of a new PMMA-based plastic fiber," in *Specialty Fiber Optic Systems for Mobile Platforms and Plastic Optical Fibers*, 1993, vol. 1799, pp. 30-37: International Society for Optics and Photonics.
- [31] R. Bates, S. Walker, and M. Yaseen, "The limits of plastic optical fiber for short distance high-speed computer data links," *Fiber & Integrated Optics*, vol. 12, no. 2, pp. 199-208, 1993.
- [32] W. Daum, A. Hoffman, U. Strecker, A. Brockmeyer, and A. Weinert, "Influence of chemicals on the durability of polymer optical fibres," in *Proceedings of the 3rd International Conference on Plastic Optical Fibres, Yokohama*, 1994, pp. 111-114.
- [33] C. F. Lam, *Passive optical networks: principles and practice*. Elsevier, 2011.
- [34] C. Lin, *Broadband Optical Access Networks and Fiber-to-the-Home*. Wiley Online Library, 2006.
- [35] Available: <https://www.marketresearch.com/MarketsandMarkets-v3719/Automotive-Communication-Technology-Bus-Module-11725925/>
- [36] J.-W. Jang, C.-Y. Kim, and Y.-S. Yu, "A Study on the MOST150/Ethernet Gateway of In-Vehicle Network," *IJCSNS*, vol. 10, no. 9, pp. 62-65, 2010.
- [37] D. M. Kuchta *et al.*, "A 71-Gb/s NRZ modulated 850-nm VCSEL-based optical link," *IEEE Photonics Technology Letters*, vol. 27, no. 6, pp. 577-580, 2015.
- [38] J. Werner, "Tutorial on carrierless AM/PM-part I-Fundamentals and digital CAP transmitter," *Contribution to ANSI X3T9*, vol. 5, 1992.
- [39] J. Werner, "Tutorial on carrierless AM/PM-Part II: Performance of bandwidth efficient line codes," *ANSI X3T9. 5 TP/PMD*, 1993.
- [40] G.-H. Im, D. Harman, G. Huang, A. Mandzik, M.-H. Nguyen, and J.-J. Werner, "51.84 mb/s 16-

- cap atm lan standard," *IEEE Journal on Selected Areas in Communications*, vol. 13, no. 4, pp. 620-632, 1995.
- [41] A. Shalash and K. K. Parhi, "Comparison of discrete multitone and carrierless AM/PM techniques for line equalization," in *1996 IEEE International Symposium on Circuits and Systems. Circuits and Systems Connecting the World. ISCAS 96*, 1996, vol. 2, pp. 560-563: IEEE.
 - [42] A. F. Shalash and K. K. Parhi, "Multidimensional carrierless AM/PM systems for digital subscriber loops," *IEEE Transactions on Communications*, vol. 47, no. 11, pp. 1655-1667, 1999.
 - [43] I. Thng, X. Li, and C. C. Ko, "A new 3D CAP system," in *Proceedings of IEEE. IEEE Region 10 Conference. TENCN 99. Multimedia Technology for Asia-Pacific Information Infrastructure* (Cat. No. 99CH37030), 1999, vol. 1, pp. 309-312: IEEE.
 - [44] M. I. Olmedo *et al.*, "Multiband carrierless amplitude phase modulation for high capacity optical data links," *Journal of Lightwave Technology*, vol. 32, no. 4, pp. 798-804, 2013.
 - [45] J. D. Ingham, R. Penty, I. White, and D. Cunningham, "40 Gb/s carrierless amplitude and phase modulation for low-cost optical datacommunication links," in *Optical Fiber Communication Conference*, 2011, p. OThZ3: Optical Society of America.
 - [46] L. Frenzel, *Principles of electronic communication systems*. McGraw-Hill, Inc., 2007.
 - [47] J. Wei, J. Ingham, D. Cunningham, R. Penty, and I. White, "Performance and power dissipation comparisons between 28 Gb/s NRZ, PAM, CAP and optical OFDM systems for data communication applications," *Journal of Lightwave Technology*, vol. 30, no. 20, pp. 3273-3280, 2012.
 - [48] J. Wei, J. Ingham, D. Cunningham, R. Penty, and I. White, "Comparisons between 28 Gb/s NRZ, PAM, CAP and optical OFDM systems for datacommunication applications," in *2012 Optical Interconnects Conference*, 2012, pp. 3-4: IEEE.
 - [49] J. Wei, D. Cunningham, R. Penty, and I. White, "Feasibility of 100G ethernet enabled by carrierless amplitude/phase modulation and optical OFDM," in *European Conference and Exhibition on Optical Communication*, 2012, p. P6. 05: Optical Society of America.
 - [50] A. Nespola, S. Abrate, R. Gaudino, C. Zerna, B. Offenbeck, and N. Weber, "High-speed communications over polymer optical fibers for in-building cabling and home networking," *IEEE Photonics Journal*, vol. 2, no. 3, pp. 347-358, 2010.
 - [51] L. Geng, R. Penty, I. White, and D. Cunningham, "FEC-free 50 m 1.5 Gb/s plastic optical fibre link using CAP modulation for home networks," in *2012 38th European Conference and Exhibition on Optical Communications*, 2012, pp. 1-3: IEEE.
 - [52] J. Wei, L. Geng, D. Cunningham, R. Penty, and I. White, "Comparisons between gigabit NRZ, CAP and optical OFDM systems over FEC enhanced POF links using LEDs," in *2012 14th International Conference on Transparent Optical Networks (ICTON)*, 2012, pp. 1-4: IEEE.
 - [53] J. Wei, L. Geng, D. Cunningham, R. Penty, and I. White, "Gigabit NRZ, CAP and optical OFDM systems over POF links using LEDs," *Optics express*, vol. 20, no. 20, pp. 22284-22290, 2012.
 - [54] C. Zerna, J. Sundermeyer, A. Fiederer, N. Verwaal, B. Offenbeck, and N. Weber, "Integrated PAM2 decision feedback equalizer for Gigabit Ethernet over standard SI-POF using red LED," in *36th European Conference and Exhibition on Optical Communication*, 2010, pp. 1-3: IEEE.
 - [55] R. Kruglov, S. Loquai, C.-A. Bunge, M. Schueppert, J. Vinogradov, and O. Ziemann, "Comparison of PAM and CAP modulation schemes for data transmission over SI-POF," *IEEE Photonics Technology Letters*, vol. 25, no. 23, pp. 2293-2296, 2013.
 - [56] F. Wu *et al.*, "Performance comparison of OFDM signal and CAP signal over high capacity

- RGB-LED-based WDM visible light communication," *IEEE Photonics Journal*, vol. 5, no. 4, pp. 7901507-7901507, 2013.
- [57] G. Stepniak, L. Maksymiuk, and J. Siuzdak, "Experimental comparison of PAM, CAP, and DMT modulations in phosphorescent white LED transmission link," *IEEE Photonics Journal*, vol. 7, no. 3, pp. 1-8, 2015.
 - [58] J. S. Chow, J. C. Tu, and J. M. Cioffi, "A discrete multitone transceiver system for HDSL applications," *IEEE journal on selected areas in communications*, vol. 9, no. 6, pp. 895-908, 1991.
 - [59] P. Neo, J. Freeman, and T. Wilkinson, "Modal Control of a 50 μ m core diameter Multimode Fiber Using a Spatial Light Modulator," in *Optical Fiber Communication Conference*, 2007, p. JThA21: Optical Society of America.
 - [60] R. A. Panicker and J. M. J. J. o. L. T. Kahn, "Algorithms for compensation of multimode fiber dispersion using adaptive optics," vol. 27, no. 24, pp. 5790-5799, 2009.
 - [61] J. Carpenter and T. D. Wilkinson, "Precise modal excitation in multimode fibre for control of modal dispersion and mode-group division multiplexing," in *2011 37th European Conference and Exhibition on Optical Communication*, 2011, pp. 1-3: IEEE.
 - [62] M. B. Shemirani and J. M. J. J. o. L. T. Kahn, "Compensation of multimode fiber dispersion by optimization of launched amplitude, phase, and polarization," vol. 28, no. 14, pp. 2084-2095, 2010.
 - [63] J. Carpenter, B. C. Thomsen, and T. D. J. I. P. T. L. Wilkinson, "Mode division multiplexing of modes with the same azimuthal index," vol. 24, no. 21, pp. 1969-1972, 2012.
 - [64] Y. Fazea and V. J. O. F. T. Mezhuyev, "Selective mode excitation techniques for mode-division multiplexing: A critical review," vol. 45, pp. 280-288, 2018.
 - [65] L. Raddatz, I. White, D. Cunningham, and M. J. J. o. L. T. Nowell, "An experimental and theoretical study of the offset launch technique for the enhancement of the bandwidth of multimode fiber links," vol. 16, no. 3, p. 324, 1998.
 - [66] D. H. Sim, Y. Takushima, and Y. C. J. J. o. L. T. Chung, "High-speed multimode fiber transmission by using mode-field matched center-launching technique," vol. 27, no. 8, pp. 1018-1026, 2009.
 - [67] J. Carpenter and T. D. J. J. o. l. t. Wilkinson, "Holographic offset launch for dynamic optimization and characterization of multimode fiber bandwidth," vol. 30, no. 10, pp. 1437-1443, 2011.
 - [68] C. Kwok, R. V. Penty, I. H. White, and D. G. Cunningham, "Novel passive launch scheme for ultimate bandwidth improvement of graded-index multimode fibers," in *Optical Fiber Communication Conference*, 2010, p. OWA3: Optical Society of America.
 - [69] L. Geng *et al.*, "Efficient line launch for bandwidth improvement of 10 Gbit/s multimode fibre links using elliptical Gaussian beam," in *36th European Conference and Exhibition on Optical Communication*, 2010, pp. 1-3: IEEE.
 - [70] D. Hondros and P. Debye, "Elektromagnetische wellen an dielektrischen drähten," *Annalen der Physik*, vol. 337, no. 8, pp. 465-476, 1910.
 - [71] O. Schriever, "Elektromagnetische wellen an dielektrischen drähten," *Annalen der Physik*, vol. 368, no. 23, pp. 645-673, 1920.
 - [72] K. Kao and G. A. Hockham, "Dielectric-fibre surface waveguides for optical frequencies," in *Proceedings of the Institution of Electrical Engineers*, 1966, vol. 113, no. 7, pp. 1151-1158: IET.

- [73] T. Miya, Y. Terunuma, T. Hosaka, and T. Miyashita, "Ultimate low-loss single-mode fibre at 1.55 μm ," *Electronics Letters*, vol. 15, no. 4, pp. 106-108, 1979.
- [74] D. Gloge, "Optical power flow in multimode fibers," *Bell System Technical Journal*, vol. 51, no. 8, pp. 1767-1783, 1972.
- [75] Y. Dong and K. W. Martin, "Gigabit communications over plastic optical fiber," *IEEE Solid-State Circuits Magazine*, vol. 3, no. 1, pp. 60-69, 2011.
- [76] M. Ishiharada, H. Kaneda, T. Chikaraishi, S. Tomita, I. Tanuma, and K. Naito, "Properties of flexible light guide made of silicone elastomer," in *First Plastic Optical Fibres and Applications Conference, Paris*, 1992, pp. 38-42.
- [77] H. Abdul-Rahman and C. Wang, "Limitations in current day lighting related solar concentration devices: a critical review," *International Journal of Physical Sciences*, vol. 5, no. 18, pp. 2730-2756, 2010.
- [78] G. Keiser, "Optical fiber communications," *Wiley Encyclopedia of Telecommunications*, 2003.
- [79] G. P. Agrawal, *Fiber-optic communication systems*. John Wiley & Sons, 2012.
- [80] J. A. Buck, *Fundamentals of optical fibers*. John Wiley & Sons, 2004.
- [81] S. Bottacchi, *Multi-gigabit transmission over multimode optical fibre: theory and design methods for 10GbE systems*. John Wiley & Sons, 2006.
- [82] Y. Sun and J. Kamino, "Optical Fiber for Datacenter Connectivity," *Datacenter Connectivity Technologies: Principles and Practice*, p. 213, 2018.
- [83] M. Duelk, "Next-generation 100 G ethernet," in *2005 31st European Conference on Optical Communication, ECOC 2005*, 2005, vol. 5, pp. 15-18: IET.
- [84] C. Lethien, C. Loyez, J.-P. Vilcot, N. Rolland, and P. A. Rolland, "Exploit the bandwidth capacities of the perfluorinated graded index polymer optical fiber for multi-services distribution," *Polymers*, vol. 3, no. 3, pp. 1006-1028, 2011.
- [85] G. Giaretta, W. White, M. Wegmuller, and T. Onishi, "High-speed (11 Gbit/s) data transmission using perfluorinated graded-index polymer optical fibers for short interconnects (< 100 m)," *IEEE Photonics Technology Letters*, vol. 12, no. 3, pp. 347-349, 2000.
- [86] T. Ishigure, Y. Koike, and J. W. Fleming, "Optimum index profile of the perfluorinated polymer-based GI polymer optical fiber and its dispersion properties," *Journal of Lightwave Technology*, vol. 18, no. 2, pp. 178-184, 2000.
- [87] J. Zubia and J. Arrue, "Plastic optical fibers: An introduction to their technological processes and applications," *Optical Fiber Technology*, vol. 7, no. 2, pp. 101-140, 2001.
- [88] Y. Koike, *Fundamentals of plastic optical fibers*. John Wiley & Sons, 2015.
- [89] N. G. Harbach, "Fiber Bragg gratings in polymer optical fibers," EPFL2008.
- [90] L.-E. Adam, J. Zaers, H. Ostertag, H. Trojan, M. Bellemann, and G. Brix, "Performance evaluation of the whole-body PET scanner ECAT EXACT HR/sup+/following the IEC standard," *IEEE Transactions on Nuclear Science*, vol. 44, no. 3, pp. 1172-1179, 1997.
- [91] Y. Koike and M. Asai, "The future of plastic optical fiber," *NPG Asia Materials*, vol. 1, no. 1, p. 22, 2009.
- [92] I. Kaminow, T. Li, and A. E. Willner, *Optical fiber telecommunications volume VIB: systems and networks*. Academic Press, 2013.
- [93] S. Abrate, R. Gaudino, A. Antonino, S. Straullu, and P. Savio, "POF-PLUS project: toward Gbit/s transmission over SI-POF for home networking," in *Proc. 17th International Conference on Polymer Optical Fibre and Application*, 2009.

- [94] Y. Koike, T. Ishigure, and E. Nihei, "High-bandwidth graded-index polymer optical fiber," *Journal of lightwave technology*, vol. 13, no. 7, pp. 1475-1489, 1995.
- [95] Y. Koike, E. Nihei, N. Tanio, and Y. Ohtsuka, "Graded-index plastic optical fiber composed of methyl methacrylate and vinyl phenylacetate copolymers," *Applied optics*, vol. 29, no. 18, pp. 2686-2691, 1990.
- [96] T. Ishigure, E. Nihei, and Y. Koike, "Graded-index polymer optical fiber for high-speed data communication," *Applied optics*, vol. 33, no. 19, pp. 4261-4266, 1994.
- [97] Y. Koike, "Progress in GI-POF status of high speed plastic optical fiber and its future prospect," in *Proceedings of the Ninth International Conference on Plastic Optical Fibres and Applications-POF'00, Boston, Massachusetts, 2000*, 2000, pp. 1-5.
- [98] H. Yang *et al.*, "47.4 Gb/s transmission over 100 m graded-index plastic optical fiber based on rate-adaptive discrete multitone modulation," *Journal of Lightwave Technology*, vol. 28, no. 4, pp. 352-359, 2010.
- [99] S. Loquai *et al.*, "42-Gb/s Transmission Over Large-Core 1-mm PMMA Graded-Index Polymer Optical Fiber," *IEEE Photonics Technology Letters*, vol. 25, no. 6, pp. 602-605, 2013.
- [100] C. Koeppen, R. Shi, W. Chen, and A. Garito, "Properties of plastic optical fibers," *JOSA B*, vol. 15, no. 2, pp. 727-739, 1998.
- [101] O. Ziemann, J. Krauser, P. E. Zamzow, and W. Daum, *POF-polymer optical fibers for data communication*. Springer Science & Business Media, 2002.
- [102] S. Lee, U. C. Paek, and Y. Chung, "Bandwidth enhancement of plastic optical fiber with multi-step core by thermal diffusion," *Microwave and Optical Technology Letters*, vol. 39, no. 2, pp. 129-131, 2003.
- [103] M. Beckers, T. Schlüter, T. Vad, T. Gries, and C. A. Bunge, "An overview on fabrication methods for polymer optical fibers," *Polymer International*, vol. 64, no. 1, pp. 25-36, 2015.
- [104] I. Mollers *et al.*, "Plastic optical fiber technology for reliable home networking: Overview and results of the EU project POF-ALL," *IEEE Communications Magazine*, vol. 47, no. 8, pp. 58-68, 2009.
- [105] R. Bockstaele *et al.*, "Microcavity LED-based parallel data link using small-diameter (125 μ m) plastic optical fibres," *Journal of Optics A: Pure and Applied Optics*, vol. 1, no. 2, p. 233, 1999.
- [106] B. P. Pal, *Fundamentals of fibre optics in telecommunication and sensor systems*. Bohem press, 1992.
- [107] S. P. Najda *et al.*, "AlGaInN laser diode technology for GHz high-speed visible light communication through plastic optical fiber and water," *Optical Engineering*, vol. 55, no. 2, p. 026112, 2016.
- [108] S. Watson *et al.*, "Multi-gigabit data transmission using a directly modulated GaN laser diode for visible light communication through plastic optical fiber and water," in *2015 IEEE Summer Topicals Meeting Series (SUM)*, 2015, pp. 224-225: IEEE.
- [109] R. Caspary *et al.*, "High speed WDM transmission on standard polymer optical fibers," in *2015 17th International Conference on Transparent Optical Networks (ICTON)*, 2015, pp. 1-4: IEEE.
- [110] W. Daum, J. Krauser, P. Zamzow, and O. Ziemann, "POF Handbook: Optical short range transmission systems," ed: Springer-Verlag, 2008.
- [111] J. J. McKendry *et al.*, "Visible-light communications using a CMOS-controlled micro-light-emitting-diode array," *Journal of lightwave technology*, vol. 30, no. 1, pp. 61-67, 2011.
- [112] R. Michalzik, *VCSELs: fundamentals, technology and applications of vertical-cavity surface-*

- emitting lasers*. Springer, 2012.
- [113] F. H. Peters *et al.*, "Vertical-cavity surface-emitting laser technology," in *Processing and Packaging of Semiconductor Lasers and Optoelectronic Devices*, 1993, vol. 1851, pp. 122-127: International Society for Optics and Photonics.
 - [114] *100W High Power Density QCW 808nm VCSEL Array Submodule*. Available: http://www.high-tech.co.jp/common/sys/product/product00369_01.pdf
 - [115] P. Westbergh *et al.*, "High-speed 850 nm VCSELs with 28 GHz modulation bandwidth operating error-free up to 44 Gbit/s," *Electronics Letters*, vol. 48, no. 18, pp. 1145-1147, 2012.
 - [116] C. Xie, "Datacenter optical interconnects: Requirements and challenges," in *2017 IEEE Optical Interconnects Conference (OI)*, 2017, pp. 37-38: IEEE.
 - [117] D. Ofelt, M. Nowell, and J. D'Ambrosia, "400 Gigabit ethernet call-for-interest consensus IEEE 802.3 ethernet working group," 2013.
 - [118] C. Cole, "Beyond 100G client optics," *IEEE communications magazine*, vol. 50, no. 2, pp. s58-s66, 2012.
 - [119] D. M. Kuchta *et al.*, "A 50 Gb/s NRZ modulated 850 nm VCSEL transmitter operating error free to 90 C," *Journal of lightwave technology*, vol. 33, no. 4, pp. 802-810, 2014.
 - [120] P. Pepeljugoski, D. Kuchta, and A. Risteski, "Modal noise BER calculations in 10-Gb/s multimode fiber LAN links," *IEEE photonics technology letters*, vol. 17, no. 12, pp. 2586-2588, 2005.
 - [121] Z. Tan *et al.*, "A 70 Gbps NRZ optical link based on 850 nm band-limited VCSEL for data-center intra-connects," *Science China Information Sciences*, vol. 61, no. 8, p. 080406, 2018.
 - [122] D. Kuchta *et al.*, "64Gb/s Transmission over 57m MMF using an NRZ Modulated 850nm VCSEL," in *Optical Fiber Communication Conference*, 2014, p. Th3C. 2: Optical Society of America.
 - [123] X. Pang *et al.*, "7× 100 Gbps PAM-4 Transmission over 1-km and 10-km Single Mode 7-core Fiber using 1.5- μ m SM-VCSEL," in *2018 Optical Fiber Communications Conference and Exposition (OFC)*, 2018, pp. 1-3: IEEE.
 - [124] M. I. Olmedo *et al.*, "Multiband carrierless amplitude phase modulation for high capacity optical data links," *Journal of Lightwave Technology*, vol. 32, no. 4, pp. 798-804, 2014.
 - [125] T. Zuo, L. Zhang, J. Zhou, Q. Zhang, E. Zhou, and G. N. Liu, "Single Lane 150-Gb/s, 100-Gb/s and 70-Gb/s 4-PAM Transmission over 100-m, 300-m and 500-m MMF Using 25-G Class 850nm VCSEL," in *ECOC 2016; 42nd European Conference on Optical Communication*, 2016, pp. 1-3: VDE.
 - [126] R. Puerta *et al.*, "Effective 100 Gb/s IM/DD 850-nm multi-and single-mode VCSEL transmission through OM4 MMF," *Journal of Lightwave Technology*, vol. 35, no. 3, pp. 423-429, 2017.
 - [127] C. Kottke *et al.*, "High-speed DMT and VCSEL-based MMF transmission using pre-distortion," *Journal of Lightwave Technology*, vol. 36, no. 2, pp. 168-174, 2018.
 - [128] D. Falconer, S. L. Ariyavisitakul, A. Benyamin-Seeyar, and B. Eidson, "Frequency domain equalization for single-carrier broadband wireless systems," *IEEE Communications Magazine*, vol. 40, no. 4, pp. 58-66, 2002.
 - [129] W. Bo *et al.*, "Single-lane 112Gbps transmission over 300m OM4 multimode fiber based on a single-transverse-mode 850nm VCSEL," in *ECOC 2016; 42nd European Conference on Optical Communication*, 2016, pp. 1-3: VDE.

- [130] J. Wang *et al.*, "50Gb/s PAM-4 oxide VCSEL development progress at Broadcom," in *Vertical-Cavity Surface-Emitting Lasers XXI*, 2017, vol. 10122, p. 1012202: International Society for Optics and Photonics.
- [131] G. D. Brown, "Bandwidth and rise time calculations for digital multimode fiber-optic data links," *Journal of Lightwave Technology*, vol. 10, no. 5, pp. 672-678, 1992.
- [132] B. Kasper, "Equalization of multimode optical fiber systems," *Bell System Technical Journal*, vol. 61, no. 7, pp. 1367-1388, 1982.
- [133] T. S. Rappaport, *Wireless communications: principles and practice*. prentice hall PTR New Jersey, 1996.
- [134] L. Geng, J. Wei, R. V. Pentty, I. White, and D. G. Cunningham, "3 Gbit/s LED-based step index plastic optical fiber link using multilevel pulse amplitude modulation," in *2013 Optical Fiber Communication Conference and Exposition and the National Fiber Optic Engineers Conference (OFC/NFOEC)*, 2013, pp. 1-3: IEEE.
- [135] J. Wang and J. M. Kahn, "Performance of electrical equalizers in optically amplified OOK and DPSK systems," *IEEE Photonics Technology Letters*, vol. 16, no. 5, pp. 1397-1399, 2004.
- [136] W. Rosenkranz and C. Xia, "Electrical equalization for advanced optical communication systems," *AEU-International Journal of Electronics and Communications*, vol. 61, no. 3, pp. 153-157, 2007.
- [137] F. R. Kschischang and B. P. Smith, "Forward error correction (FEC) in optical communication," in *CLEO/QELS: 2010 Laser Science to Photonic Applications*, 2010, pp. 1-2: IEEE.
- [138] R. M. J. I. T. o. c. Pyndiah, "Near-optimum decoding of product codes: Block turbo codes," vol. 46, no. 8, pp. 1003-1010, 1998.
- [139] W. J. Gross, V. C. Gaudet, and A. Milner, "Stochastic implementation of LDPC decoders," in *Conference Record of the Thirty-Ninth Asilomar Conference on Signals, Systems and Computers, 2005.*, 2005, pp. 713-717: IEEE.
- [140] E. Agrell, and M. Secondini, "Information-Theoretic Tools for Optical Communications Engineers," *IEEE Photonics Conference (IPC)*, pp. 1-5, 2018, doi: 10.1109/IPCon.2018.8527126.
- [141] M. Schüppert and C.-A. Bunge, "5Gb/s Eye-Safe LED-Based SI-POF Transmission With Equalization of Transmitter Nonlinearities," *IEEE Photonics Technology Letters*, vol. 28, no. 23, pp. 2732-2735, 2016.
- [142] X. Li *et al.*, "μLED-based single-wavelength bi-directional POF link with 10 Gb/s aggregate data rate," *Journal of Lightwave Technology*, vol. 33, no. 17, pp. 3571-3576, 2015.
- [143] K. Azadet *et al.*, "Equalization and FEC techniques for optical transceivers," *IEEE Journal of Solid-State Circuits*, vol. 37, no. 3, pp. 317-327, 2002.
- [144] M. Maeng *et al.*, "0.18-/spl mu/m CMOS equalization techniques for 10-Gb/s fiber optical communication links," *IEEE Transactions on Microwave Theory and Techniques*, vol. 53, no. 11, pp. 3509-3519, 2005.
- [145] X. Li *et al.*, "Wireless visible light communications employing feed-forward pre-equalization and PAM-4 modulation," *Journal of Lightwave Technology*, vol. 34, no. 8, pp. 2049-2055, 2016.
- [146] J. Zhang, J. Yu, N. Chi, and H.-C. Chien, "Time-domain digital pre-equalization for band-limited signals based on receiver-side adaptive equalizers," *Optics express*, vol. 22, no. 17, pp. 20515-20529, 2014.
- [147] J. Pan, P. Isautier, and S. E. Ralph, "Digital pre-shaping for narrowband filtering impairment

- compensation in superchannel applications," in *Integrated Photonics Research, Silicon and Nanophotonics*, 2013, p. JT3A. 1: Optical Society of America.
- [148] T. Freckmann, C. V. González, and J. M. R.-C. Crespo, "Joint electronic dispersion compensation for DQPSK," in *OFC/NFOEC 2008-2008 Conference on Optical Fiber Communication/National Fiber Optic Engineers Conference*, 2008, pp. 1-3: IEEE.
 - [149] C. Ye, D. Zhang, X. Huang, H. Feng, and K. Zhang, "Demonstration of 50Gbps IM/DD PAM4 PON over 10GHz class optics using neural network based nonlinear equalization," in *2017 European Conference on Optical Communication (ECOC)*, 2017, pp. 1-3: IEEE.
 - [150] Z. Wan *et al.*, "Nonlinear equalization based on pruned artificial neural networks for 112-Gb/s SSB-PAM4 transmission over 80-km SSMF," *Optics express*, vol. 26, no. 8, pp. 10631-10642, 2018.
 - [151] M. A. Jarajreh *et al.*, "Artificial neural network nonlinear equalizer for coherent optical OFDM," *IEEE Photonics Technology Letters*, vol. 27, no. 4, pp. 387-390, 2014.
 - [152] E. Giacomidis *et al.*, "Intra and inter-channel nonlinearity compensation in WDM coherent optical OFDM using artificial neural network based nonlinear equalization," in *2017 Optical Fiber Communications Conference and Exhibition (OFC)*, 2017, pp. 1-3: IEEE.
 - [153] J. Thrane, J. Wass, M. Piels, J. C. Diniz, R. Jones, and D. Zibar, "Machine learning techniques for optical performance monitoring from directly detected PDM-QAM signals," *Journal of Lightwave Technology*, vol. 35, no. 4, pp. 868-875, 2016.
 - [154] F. Karinou, N. Stojanovic, C. Prodaniuc, Z. Qiang, and T. Dippon, "112 Gb/s PAM-4 optical signal transmission over 100-m OM4 multimode fiber for high-capacity data-center interconnects," in *ECOC 2016; 42nd European Conference on Optical Communication*, 2016, pp. 1-3: VDE.
 - [155] R. Puerta, J. J. V. Olmos, I. T. Monroy, N. N. Ledentsov, and J. P. Turkiewicz, "Flexible multiCAP modulation and its application to 850 nm VCSEL-MMF links," *Journal of Lightwave Technology*, vol. 35, no. 15, pp. 3168-3173, 2017.
 - [156] D. E. Rumelhart, G. E. Hinton, and R. J. Williams, "Learning representations by back-propagating errors," *Cognitive modeling*, vol. 5, no. 3, p. 1, 1988.
 - [157] X. Guo, D. G. Cunningham, R. V. Pentty, and I. H. White, "Optical equalizers for bandwidth-limited transmitters and pam-based fiber optic links," *Journal of Lightwave Technology*, vol. 36, no. 12, pp. 2484-2491, 2018.
 - [158] G. Raybon, P. J. Winzer, and C. R. Doerr, "10 x 107-Gbit/s electronically multiplexed and optically equalized NRZ transmission over 400 km," in *Optical Fiber Communication Conference*, 2006, p. PDP32: Optical Society of America.
 - [159] V. Mikhailov, C. Doerr, L. Buhl, R. Killey, P. Bayvel, and L. WC1E, "Mitigation of signal distortion in 42.7 Gb/s duobinary transmission using a single chip optical equalizer," in *2007 33rd European Conference and Exhibition of Optical Communication, ECOC 2007*, 2007: IET.
 - [160] C. Doerr *et al.*, "A single-chip optical equalizer enabling 107-Gb/s optical non-return-to-zero signal generation," in *2005 31st European Conference on Optical Communication, ECOC 2005*, 2005, vol. 6, pp. 13-14: IET.
 - [161] A. Bhardwaj, N. Sauer, L. Buhl, W. Yang, L. Zhang, and D. T. Neilson, "An InP-based optical equalizer monolithically integrated with a semiconductor optical amplifier," *IEEE Photonics Technology Letters*, vol. 19, no. 19, pp. 1514-1516, 2007.
 - [162] P. Dong, C. Xie, L. L. Buhl, Y.-K. Chen, J. H. Sinsky, and G. Raybon, "Silicon in-

- phase/quadrature modulator with on-chip optical equalizer," *Journal of Lightwave Technology*, vol. 33, no. 6, pp. 1191-1196, 2015.
- [163] C. Doerr *et al.*, "Simple multichannel optical equalizer mitigating intersymbol interference for 40-Gb/s nonreturn-to-zero signals," *Journal of lightwave technology*, vol. 22, no. 1, pp. 249-256, 2004.
 - [164] T. N. Huynh *et al.*, "4× 50Gb/s NRZ shortwave-wavelength division multiplexing VCSEL link over 50m multimode fiber," in *Optical Fiber Communication Conference*, 2017, p. Tu2B. 5: Optical Society of America.
 - [165] C. Kottke, C. Caspar, V. Jungnickel, R. Freund, M. Agustin, and N. N. Ledentsov, "High speed 160 Gb/s DMT VCSEL transmission using pre-equalization," in *2017 Optical Fiber Communications Conference and Exhibition (OFC)*, 2017, pp. 1-3: IEEE.